

ACTA GEO TECHNICA SLOVENICA

2011/2

s. m. springman et al.

LESSONS LEARNT FROM FIELD INVESTIGATIONS IN POTENTIALLY UNSTABLE SLOPES IN SWITZERLAND

m. skrinar & b. lutar

ANALYSIS OF CRACKED SLENDER-BEAMS ON WINKLER'S FOUNDATION USING A SIMPLIFIED COMPUTATIONAL MODEL

e. uncuoğlu & m. laman

LATERAL RESISTANCE OF A SHORT RIGID PILE IN A TWO-LAYER COHESIONLESS SOIL

m. marjanović et al.

LANDSLIDE ASSESSMENT OF THE STARČA BASIN (CROATIA) USING MACHINE LEARNING ALGORITHMS

p. oreste

THE STABILITY OF THE EXCAVATION FACE OF SHALLOW CIVIL AND MINING TUNNELS

m. maček et al.

INFLUENCE OF MOULD SUCTION ON THE VOLUME-CHANGE BEHAVIOUR OF COMPACTED SOILS DURING INUNDATION



ustanovitelji **founders**

Univerza v Mariboru, Fakulteta za gradbeništvo
University of Maribor, Faculty of Civil Engineering
Univerza v Ljubljani, Fakulteta za gradbeništvo in geodezijo
University of Ljubljana, Faculty of Civil and Geodetic Engineering
Univerza v Ljubljani, Naravoslovnotehniška fakulteta
University of Ljubljana, Faculty of Natural Sciences and Engineering
Slovensko geotehniško društvo
Slovenian Geotechnical Society
Društvo za podzemne in geotehniške konstrukcije
Society for Underground and Geotechnical Constructions

izdajatelj **publisher**

Univerza v Mariboru, Fakulteta za gradbeništvo
University of Maribor, Faculty of Civil Engineering

odgovorni urednik **editor-in-chief**

Ludvik Trauner
University of Maribor

uredniki **co-editors**

Bojana Dolinar
University of Maribor
Borut Macuh
University of Maribor
Stanislav Škrabl
University of Maribor
Helena Vrecl Kojc
University of Maribor
Damijana Zlatolas
University of Maribor
Bojan Žlender
University of Maribor

posvetovalni uredniki **advisory editors**

Darinka Battelino
University of Trieste
Heinz Brandl
Vienna University of Technology
Chandrakant. S. Desai
University of Arizona
Pedro Seco e Pinto
National Laboratory of Civil Engineering

lektor **proof-reader**

Paul McGuiness

naklada **circulation**

300 izvodov - issues

tisk **print**

Tercia tisk d.o.o. Ptuj

Revija redno izhaja dvakrat letno. Članki v reviji so recenzirani s strani priznanih mednarodnih strokovnjakov. Baze podatkov v katerih je revija indeksirana: SCIE - Science Citation Index Expanded, JCR - Journal Citation Reports / Science Edition, ICONDA - The international Construction database, GeoRef. Pri financiranju revije sodeluje Javna agencija za knjigo Republike Slovenije.

uredniški odbor **editorial board**

József Farkas
Budapest University of Technology and Economics
Theodoros Hatzigogos
Aristotle University of Thessaloniki
Rolf Katzenbach
Technical University Darmstadt
Nasser Khalili
The University of New South Wales, Sydney
Zlatko Langof
University of Sarajevo
Jakob Likar
University of Ljubljana
Janko Logar
University of Ljubljana
Bojan Majes
University of Ljubljana
Milan Maksimović
University of Belgrade
Borut Petkovšek
Slovenian National Building and Civil Engineering Institute
Mihael Ribičič
University of Ljubljana
César Sagaseta
University of Cantabria
Patrick Selvadurai
McGill University
Stephan Semprich
University of Technology Graz
Devendra Narain Singh
Indian Institute of Technology, Bombay
Abdul-Hamid Soubra
University of Nantes
Kiirchi Suzuki
Saitama University
Antun Szavits-Nossan
University of Zagreb
Ivan Vaniček
Czech Technical University in Prague
Jianhua Yin
The Hong Kong Polytechnic University

naslov uredništva **address**

ACTA GEOTECHNICA SLOVENICA
Univerza v Mariboru, Fakulteta za gradbeništvo
Smetanova ulica 17, 2000 Maribor, Slovenija
Telefon / Telephone: +386 (0)2 22 94 300
Faks / Fax: +386 (0)2 25 24 179
E-pošta / E-mail: ags@uni-mb.si

spletni naslov **web address**

<http://www.fg.uni-mb.si/journal-ags/>

The journal is published twice a year. Papers are peer reviewed by renowned international experts. Indexation data bases of the journal: SCIE - Science Citation Index Expanded, JCR - Journal Citation Reports / Science Edition, ICONDA - The international Construction database, GeoRef. Financially supported also by Slovenian Book Agency.

VSEBINA

2	Ludvik Trauner UVODNIK
4	Matjaž Skrinar in Boris Lutar ANALIZA VITKIH RAZPOKANIH NOSILCEV NA WINKLERJEVI ZEMLJINI Z UPORABO POENOSTAVLJENEGA RAČUNSKEGA MODELA
18	erdal uncuoğlu in Mustafa Laman BOČNA NOSILNOST KRATKIH TOGIH PILOTOV V DVOSLOJNIH NEVEZLJIVIH TLEH
44	Miloš Marjanović in drugi OCENA UDORA KOTLINE STAAČA (HVAŠKA) Z UPORABO STROJNEGA UČENJA ALGORITMOV
56	Pierpaolo Oreste STABILNOST POVRŠINE IZKOPA PLITVIH GRADBENIH IN RUDARSKIH PREDOROV
66	Matej Maček in drugi VPLIV VROJENE SUKCIJE NA VOLUMENSKO OBNAŠANJE ZGOŠČENIH ZEMLJIN MED VLAŽENJEM
80	NAVODILA AVTORJEM

CONTENTS

Ludvik Trauner EDITORIAL	3
Matjaž Skrinar and Boris Lutar ANALYSIS OF CRACKED SLENDER-BEAMS ON WINKLER'S FOUNDATION USING A SIMPLIFIED COMPUTATIONAL MODEL	5
erdal uncuoğlu and Mustafa Laman LATERAL RESISTANCE OF A SHORT RIGID PILE IN A TWO-LAYER COHESIONLESS SOIL	19
Miloš Marjanović et al. LANDSLIDE ASSESSMENT OF THE STAAČA BASIN (CROATIA) USING MACHINE LEARNING ALGORITHMS	45
Pierpaolo Oreste THE STABILITY OF THE EXCAVATION FACE OF SHALLOW CIVIL AND MINING TUNNELS	57
Matej Maček et al. INFLUENCE OF MOULD SUCTION ON THE VOLUME-CHANGE BEHAVIOUR OF COMPACTED SOILS DURING INUNDATION	67
INSTRUCTIONS FOR AUTHORS	81

UVODNIK

V letošnjem letu smo za urejanje mednarodne revije AGS uvedli novi informacijski sistem, ki nam olajša in izboljša uredniško delo. Interaktivno komuniciranje med uredniki, recenzenti in avtorji prispevkov je s tem postalo hitrejše in kvalitetnejše. Z ozirom na to, da v uredništvo prihaja vedno več prispevkov iz vseh kontinentov sveta, je ta komunikacijska oblika bila nujna. Vsi zainteresirani si lahko delovanje sistema ogledajo na naši spletni strani <http://www.fg.uni-mb.si/journal-ags/> ali direktno na <http://zalozba.uni-mb.si/index.php/ags/>.

V pričujoči številki objavljamo 5 zanimivih prispevkov:

Prvi članek, avtorjev Matjaža Skrinarja in Borisa Lutarja, obravnava uporabo pogosto uporabljenega poenostavljenega računskega modela za analitični izračun prečnih premikov vitkih nosilcev, vgrajenih v Winklerjevi zemljini, ki so prečno razpokani. Prikazano je reševanje pripadajočih diferencialnih enačb in pridobitev natančnih analitičnih rešitev za izračun prečnih premikov poenostavljenega modela.

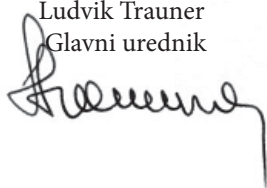
V drugem članku sta avtorja Erdal Uncuoğlu in Mustafa Laman predstavila raziskavo bočno obteženih kratkih pilotov v dvoslojnih peskih. Za ta namen je bil izveden niz modelnih preizkusov na modelih pilotov. Z izvedbo niza tridimenzionalnih nelinearnih analiz s končnimi elementi so bili raziskani učinki elastičnega modula, dilatacije in interakcije peska in pilota.

V tretjem članku so avtorji Miloš Marjanović, Miloš Kovačević, Branislav Bajat, Snježana Mihalić in Biljana Abolmasov primerjali algoritme strojnega učenja v okviru prognoze drsenja terena. Na osnovi GIS slojev področja kotline Starča, ki so vključevali geološke, hidrogeološke, morfometrijske in druge prostorske podatke, je napravljena klasifikacija mrežnih celic na primerih »drsečega« in »stabilnega terena«.

V četrtem prispevku je avtor Pierpaolo Oreste prikazal nov računski postopek, ki analizira statične pogoje površine v plitvih predorih, tudi če so ojačani s steklenimi vlakni. Postopek temelji na omejeni ravnotežni metodi, uporabljeni na zemljišču pod površino.

Peti članek avtorjev Mateja Mačka, Bojana Majesa in Ane Petkovšek, predstavlja rezultate raziskav, opravljenih na zgoščenih zemljinah, v okviru katerih konvencionalne raziskave dopolnili z meritvami sukcije. V pogojih vlažne in zmerne klime se glinene zemljine, ki so se kompaktirale na suhi strani Proktorjeve krivulje, dodatno navlažijo. Proces vlaženja spremlja zniževanje sukcije in dodatne deformacije, ki so lahko nabrekanje ali strukturni kolaps.

Ludvik Trauner
Glavni urednik



EDITORIAL

This year we introduced a new information system in order to simplify and improve the editorial work of the international journal AGS. Thus, communications among the editors, the reviewers and the authors of the articles is now faster. This form of communication was necessary because more and more contributions are being submitted to our editorial board from all continents. If you are interested in our new system, please visit our website <http://www.fg.uni-mb.si/journal-ags/> or <http://zalozba.uni-mb.si/index.php/ags/>.

In this issue we publish five interesting new contributions:

The first article, by Matjaž Skrinar and Boris Lutar, discusses the coupling of Winkler's soil model with a simplified computational model that is widely used for the calculation of transverse displacements in transversely cracked slender beams. The bending problem of a cracked beam embedded in Winkler's soil is addressed by means of an analytical approach.

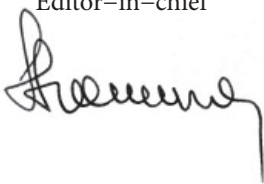
In the second article, the authors Erdal Uncuoğlu and Mustafa Laman investigated the behaviour of a laterally loaded, short, rigid pile founded in a two-layer sand-soil profile. For this purpose, a series of model tests was carried out on model piles. The effects of the elasticity modulus, dilatancy and interface behaviour of the sand were explored numerically by performing a series of three-dimensional, non-linear, finite-element analyses.

The authors of the third article, Miloš Marjanović, Miloš Kovačević, Branislav Bajat, Snježana Mihalić and Biljana Abolmasov, compared machine-learning algorithms in a landslide-susceptibility assessment. Given the input set of GIS layers for the Starča Basin, which included geological, hydrogeological, morphometric, and environmental data, a classification task was performed to classify the grid cells into landslide and non-landslide cases.

In the fourth contribution, Pierpaolo Oreste illustrates a new calculation procedure for the analysis of the face static condition in shallow tunnels, also when reinforcement interventions with fibreglass dowels are used. The procedure is based on the limit-equilibrium method applied to the ground core ahead of the face.

The fifth paper, by Matej Maček, Bojan Majes and Ana Petkovšek, presents the results of tests performed on a relatively large number of compacted test specimens, where the conventional index parameters, used to identify compacted soils, were supplemented by a suction-water-content curve, and measurements of "mould" suction. In wet climatic conditions the compaction on the dry side of the Proctor curve, which enables a high layer stiffness during construction, may result in permanent deformation and softening during the lifetime of the structure.

Ludvik Trauner
Editor-in-chief



ANALIZA VITKIH RAZPOKANIH NOSILCEV NA WINKLERJEVI ZEMLJINI Z UPORABO POENOSTAVLJENEGA RAČUNSKEGA MODELA

MATJAŽ SKRINAR IN BORIS LUTAR

o avtorjih

Matjaž Skrinar
University of Maribor,
Faculty of Civil Engineering
Smetanova 17, 2000 Maribor, Slovenija
E-pošta: skrinar@uni-mb.si

Boris Lutar
University of Maribor,
Faculty of Civil Engineering
Smetanova 17, 2000 Maribor, Slovenija
E-pošta: lutar@uni-mb.si

izvleček

Članek obravnava uporabo pogosto uporabljenega poenostavljenega računskega modela za analitični izračun prečnih premikov vitkih nosilcev, vgrajenih v Winklerjevi zemljini, ki so prečno razpokani. Prikazano je reševanje pripadajočih diferencialnih enačb in pridobitev natančnih analitičnih rešitev za izračun prečnih premikov poenostavljenega modela. Rešitve za pomike omogočajo izračun porazdelitve notranjih upogibnih momentov in strižnih sil z uporabo znanih zvez iz Euler-Bernoullijeve teorije upogiba ali z uporabo dveh mehanskih ravnotežnih pogojev.

Numerična primera pokrivata obtežni situaciji, na kratko predstavljata možnosti uporabe modela in potrjujeta uporabnost predstavljenega pristopa. Rezultati, ki so pridobljeni s predstavljenim pristopom, so primerjani še z vrednostmi iz obsežnih diskretnih računskih modelov po metodi končnih elementov, tvorjenimi z 2D končnimi elementi. Očitno je, da se velike razlike obsega vložene računskega dela modelov ne odražajo v pomembnih razlikah rezultatov med računskima modeloma.

ključne besede

nosilci s prečnimi razpokami, poenostavljeni računski model, elastična podlaga, Winklerjeva zemljina, prečni pomiki, upogibni momenti in prečne sile

ANALYSIS OF CRACKED SLENDER-BEAMS ON WINKLER'S FOUNDATION USING A SIMPLIFIED COMPUTATIONAL MODEL

MATJAŽ SKRINAR AND BORIS LUTAR

about the authors

Matjaž Skrinar
University of Maribor,
Faculty of Civil Engineering
Smetanova 17, 2000 Maribor, Slovenia
E-mail: skrinar@uni-mb.si

Boris Lutar
University of Maribor,
Faculty of Civil Engineering
Smetanova 17, 2000 Maribor, Slovenia
E-mail: lutar@uni-mb.si

abstract

This paper discusses the coupling of Winkler's soil model with a simplified computational model that is widely used for the calculation of transverse displacements in transversely cracked slender beams. The bending problem of a cracked beam embedded in Winkler's soil is addressed by means of an analytical approach. The solving of the corresponding differential equation solutions is studied in order to obtain exact analytical expressions for the transverse displacements of the simplified computational model. After the solutions for the displacements of the beam are obtained, the inner bending moment and the shear force distributions within the beam can be calculated, either by using known, established relationships from the Euler-Bernoulli beam theory or by implementing two mechanical equilibrium conditions.

Numerical examples covering several load situations are briefly presented in order to support the discussed approach. The results obtained with the presented approach are then further compared with the values from huge 2D finite-element models, where a detailed description of the crack was achieved using the discrete approach. It is evident that any drastic difference in the computational effort is not reflected in the significant differences in the results between the models.

keywords

beams with transverse cracks, simplified computational model, elastic foundation, Winkler's soil, transverse displacements, bending moment and shear forces

1 INTRODUCTION

Although cracks can certainly be considered as one of the most unfavourable effects that might occur in a structure, and many efforts are invested in their prevention during the utilization of a structure, some engineering situations actually require their inclusion within the analysis. A typical example of such a situation is in the design of structures for earthquake resistance, according to the current regulations. The EN 1998 standard, for example, requires that in concrete buildings, in composite steel-concrete buildings, and in masonry buildings, the stiffness of the load-bearing elements should, in general, be evaluated by taking into account the effect of cracking. This standard further allows for the two elastic (flexural as well as shear, but not axial) stiffness properties of concrete and masonry elements to be taken as being equal to one half of the corresponding stiffness of the non-cracked elements, unless a more accurate analysis of the cracked elements is performed. Since the explicit modelling of cracks requires the implementation 2D or 3D finite elements, where a detailed discretisation of the crack and its surrounding can be properly achieved with an appropriate mesh of finite elements, an accurate analysis is time-consuming and demands a substantial computational effort.

However, the structural analysis of cracked beams is of great engineering interest (although primarily from the inverse-identification point of view), and has been extensively studied over recent decades, resulting in numerous investigations. Several studies have confirmed that cracks can be successfully and implicitly treated as slope discontinuities within a 1D model of a beam. This simplified model, given by Okamura et al. [1], where

the crack is represented by means of an internal hinge endowed with a massless rotational spring (using the linear moment-rotation constitutive law), thus connecting those non-cracked parts of the structure that are modelled as elastic elements, represents the basis for a number of papers. Okamura et al. further introduced the earliest definition for the rotational linear spring stiffness K_r of a rectangular cross-section. In addition, some other researchers [2-8] have presented their definitions.

The model was successfully implemented for a direct analysis of the dynamics when determining the natural frequencies and mode shapes (Shifrin and Ruotolo [9], Khiem and Lien [10], Li [11], Fernández-Sáez and Navarro [12]).

Okamura's simplified computational model has already been implemented regarding the experimental inverse identification of a crack (Rizos et al. [13], Boltežar et al. [14], Vestroni and Capecchi [15], Bamnios et al. [16]).

However, since the governing differential equations of a bending displacement can only be solved analytically for moderate structures, the research interest has further oriented towards finite-element solutions (Gounaris and Dimarogonas [17], Skrinar and Umek [18], Skrinar [19], Krawczuk and Žak [20], Kisa and Brandon [21]).

Two main approaches exist for the modelling of cracks within those derivations based on the same computational model. Although they converge towards the same results, they differ regarding genuine mechanical descriptions, and also mathematical instrumentations. The first approach, also implemented within the presented manuscript, appears to be more mechanical (or engineering). It is based on the solutions of coupled governing differential equations for the elastic non-cracked regions where the cracks are modelled as slope discontinuities ([7], [9], [10], [12], [14], [16], [18], [19], [20], [22]). For various types of problems, the general solutions (as functions of four integration constants only) are usually given in advance, and the influence of the cracks is hence taken into account regarding four continuity conditions at each location. Consequently, the coefficients that govern displacement functions are explicit functions of pure mechanical information – the stiffnesses of rotational springs. In the second approach, the singularities of flexural stiffness, as represented by the Dirac delta unit step functions, are directly introduced within the governing differential equation (Caddemi and Caliò [23], Biondi and Caddemi [24,25]). This governing equation is, thus, exclusively formulated over the entire domain of the beam without the explicit enforcement of any of those continuity conditions already accounted for in the adopted flexural stiffness

model. However, in order to prevent meaningless negative values for either the flexural rigidity or the rotational stiffness, as caused by the negative impulses applied to the flexural rigidity of the element, those coefficients (without any apparent physical interpretation) that govern the solution of a unique governing differential equation, must additionally fulfil certain mathematical conditions.

In order to expand previous realizations, the scope of the presented paper is oriented towards an examination of the simplified model's behaviour regarding the problems of slender-cracked beams resting on an elastic soil. The idea of modelling soil as an elastic medium was first introduced by Winkler, and since then Winkler's soil model has been the focus of extensive research. This model is the most convenient representation of soil support within the domain of linear elasticity for framed structure-soil interaction analyses. Several approaches to the analysis of non-cracked beams on elastic foundations can be found in the literature. Jones [26] implemented a finite difference theory, Chen [27] used differential quadrature to discretize the governing differential equations defined on all elements for solving the problem of beams resting on an elastic foundation, Onu [28] derived a formulation leading to an explicit free-of meshing stiffness matrix for a beam finite-element foundation model. Guo and Weitsman [29] employed Green's foundation formulation to evaluate the response of beams on non-uniform elastic foundations, with the nonlinear material and geometric behaviours of reinforced concrete. The non-linear material and geometric behaviour of reinforced concrete deep-beams resting on a linear or non-linear Winkler's foundation was studied by Al-Azzawi et al. [30], by implementing a smeared-crack model within a finite-elements model established with ANSYS computer software. For a solution using a layer finite-element method, an incremental approach within a modified Newton-Raphson iteration method was employed by Cerioni and Mingardi [31]. The design analysis of beams, circular plates, and cylindrical tanks, on elastic foundations with a beam/strip analysis, was also studied by Melerski [32].

This paper studies those analytical equations for the load-displacement response of a cracked-elastic beam on a Winkler's soil model, as established through the solutions from governing differential equations, regarding an implemented, simplified crack-model. These solutions can be established in a straightforward manner, in order to yield a system of linear algebraic equations that can be solved by elementary numerical techniques. To complete the study, the results obtained with the simplified computational model are compared with the results obtained from more precise, as well as detailed and,

consequently, more computational effort requiring large 2D finite elements models where the discrete approach is utilized for the description of the crack. The presented examples confirm that the elaborated solutions may be effectively implemented for static structural analyses, where cracked beam-like elements are required.

2 SIMPLIFIED MODEL FOR CRACKED BEAMS ON WINKLER'S FOUNDATION

One of the simplest models for a mathematical description of a cracked structure's response behaviour is a model where the crack is introduced as a rotational linear spring connecting the non-cracked parts of the structure, as presented by Okamura et al. [1] (Fig. 1). Due to the localized effect of the crack, both the non-cracked adjacent parts of the element (to the left and to the right of the crack) are modelled as elastic sections.

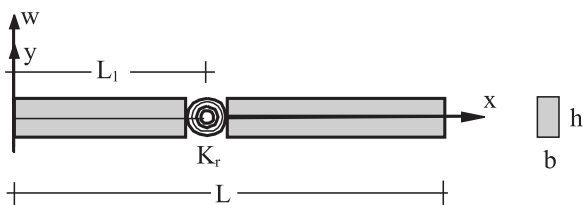


Figure 1. Okamura's computational model for transverse displacements.

The crack is defined by its location (i.e., the distance L_1 from the left-hand end), and depth d . The transverse displacements are thus (in addition to all the other parameters of the structure) a function of the crack stiffness K_r . The stiffness of the massless rotational spring depends on the height of the non-cracked cross-section h , the relative depth of the crack $\delta = d/h$, and the product of the Young's modulus E with the moment of inertia of the non-cracked cross-section I , i.e., the flexural rigidity EI . Okamura et al. introduced the earliest definition of rotational stiffness, and this is the only definition that also takes Poisson's ratio ν into account:

$$K_r = \frac{EI}{h \cdot 6 \cdot (1 - \nu^2) \cdot F(\delta)} \quad (1)$$

with

$$F(\delta) = 1.98 \cdot \delta^2 - 3.277 \cdot \delta^3 + 14.43 \cdot \delta^4 - 31.26 \cdot \delta^5 + 63.56 \cdot \delta^6 - 103.36 \cdot \delta^7 + 147.52 \cdot \delta^8 - 127.69 \cdot \delta^9 + 61.50 \cdot \delta^{10}$$

When studying the elastic displacement of a non-cracked beam element of infinitesimal length, it is possible to derive a governing differential equation that relates to the coordinate x , transverse displacement $w(x)$, the geometrical and mechanical properties of the cross-section (flexural rigidity EI), and the applied transverse load $q(x)$. The general solution of the equation for a beam on Winkler's soil model, which is a fourth-order ordinary differential equation with constant coefficients, can be given in two alternative mathematical forms. The form, as used in this manuscript, can be found in many structural textbooks, for example, in Oden, [33]:

$$w(x) = e^{\beta \cdot x} \cdot (A \cdot \cos(\beta \cdot x) + B \cdot \sin(\beta \cdot x)) + e^{-\beta \cdot x} \cdot (C \cdot \cos(\beta \cdot x) + D \cdot \sin(\beta \cdot x)) + \text{particular integral} \quad (2)$$

with

$$\beta = \sqrt[4]{\frac{k}{4 \cdot E \cdot I}}$$

where A , B , C and D are constants of the integration obtained from boundary conditions, whilst the particular integral depends on the mathematical form of the load $q(x)$. The constant k is referred to as the constant of proportionality, given as a product of the modulus (or coefficient) of the subgrade reaction k_s with the width of the beam b . The relationship between the soil subgrade reaction modulus and its elastic properties, i.e., the modulus of elasticity for the elastic medium E_f and the Poisson's ratio ν_f is given by a formula developed by Selvadurai [34]:

$$k_s = \frac{0.65 \cdot E_f}{b \cdot (1 - \nu_f^2)}$$

However, since the crack separates the beam into two elastic parts, the transverse displacements cannot be described by a single function anymore and, therefore, two displacement functions are required. Consequently, two coupled differential equations for the parts on the left- ($v_1(x)$) and right-hand ($v_2(x)$) sides of the crack, with eight unknown constants altogether, have to be solved simultaneously. The solutions, i.e., the functions $w_1(x)$ and $w_2(x)$ for the parts to the left and the right, respectively, implement eight unknown constants altogether:

$$w_1(x) = e^{\beta \cdot x} \cdot (A_1 \cdot \cos(\beta \cdot x) + B_1 \cdot \sin(\beta \cdot x)) + e^{-\beta \cdot x} \cdot (C_1 \cdot \cos(\beta \cdot x) + D_1 \cdot \sin(\beta \cdot x)) + \text{particular integral} \quad (3)$$

$$w_2(x) = e^{\beta \cdot x} \cdot (A_2 \cdot \cos(\beta \cdot x) + B_2 \cdot \sin(\beta \cdot x)) + e^{-\beta \cdot x} \cdot (C_2 \cdot \cos(\beta \cdot x) + D_2 \cdot \sin(\beta \cdot x)) + \text{particular integral} \quad (4)$$

Four of them are determined from the actual boundary conditions, and the remaining four are obtained from the continuity conditions at the crack location ($x=L_1$), where the influence of the crack is introduced as a slope discontinuity. These conditions are the equality of displacement:

$$w_1(L_1) = w_2(L_1), \quad (5)$$

the condition for the discrete increase of the rotations:

$$\varphi_1(L_1) + \frac{EI \cdot w_1''(L_1)}{K_r} = \varphi_2(L_1), \quad (6)$$

the equality of the bending moments:

$$w_1''(L_1) = w_2''(L_1), \quad (7)$$

and the equality of the shear forces:

$$w_1'''(L_1) = w_2'''(L_1). \quad (8)$$

The described approach can be straightforwardly expanded to cover a situation with N_c cracks that split the beam into N_{c+1} elastic segments. A transverse displacement computation requires solving the N_{c+1} coupled governing differential equations by implementing four mechanical boundary conditions and $4 \cdot N_c$ continuity conditions.

After the solutions for the displacements of the beam are obtained, the bending moment and shear force distributions within the beam can be calculated using the well-known relationships from the Euler-Bernoulli beam theory. However, with known solutions for the displacements, the problem becomes statically determinate. Consequently, the internal load distributions may also be fully determined by implementing two mechanical equilibrium conditions without using stiffness criteria.

The discussed approach even allows for analytical solutions of the transverse displacements to be constructed for some load situations. However, for two main reasons these solutions are not actually essential in engineering practice. Firstly, analytical solutions cannot cover all the general load cases that may appear, and furthermore, their derivations are also very time consuming. Secondly, in engineering practice, numerical results are sufficient for the analysis.

3 VALIDATIONS

Two load situations of a cracked structure were analyzed in order to verify the discussed approach. The length L

of the beam was 10 m, the cross-section was a rectangle with dimensions of 0.80 m by 0.80 m, and the Young modulus was 33 GPa (corresponding to concrete grade C30/37). Two cracks were introduced at distances of 3 m and 2 m from the left- and right-hand ends, respectively. The depths of both cracks were 0.4 m and, from among all the existing definitions for a rotational spring, the definition given by Okamura was selected (producing the value $K_r = 4.423902 \cdot 10^8$ Nm) due to the fact that this is the only one that takes the Poisson's ratio into account. For this relative depth and a Poisson's ratio of 0.3, Okamura's definition produces results that have been proved to be in good agreement with those experimentally obtained values, as presented by Vestroni [35].

The Winkler's foundation was assumed to have a subgrade reaction modulus of $k_s = 50$ MPa/m.

Transverse displacements, shear forces, and bending moments along the structure's length were studied for all load cases.

The considered structure was furthermore modelled using finite elements by implementing the SolidWorks Simulation Professional v. 2011 finite-element program, where the discrete-crack approach was utilized to model the cracks. The transverse displacements and reactions were obtained from a computational model consisting of 163,369 2D six-noded quadrilateral second-order triangular-shell finite elements with more than 327,747 nodal points. In each node, three degrees of freedom were taken into account – vertical and horizontal displacements, as well as rotation. The vertical and horizontal displacements for each load combination were obtained in discrete points by solving approximately 2,000,000 linear equations.

3.1 LOAD CASE 1: THREE CONCENTRATED DOWNWARD FORCES

During the first load situation three vertical downward transverse forces were applied, located at the left-end ($F_1=500$ kN), mid-span ($F_2=800$ kN), and the right-end ($F_3=250$ kN), Fig. 2. Since the structure had two cracks and a concentrated in-field transverse load, the corresponding computational model of the considered load combination consisted of four elastic segments. Consequently, four coupled functions for four elastic regions had to be analyzed in order to obtain vertical displacement distributions along the structure. The interpolation functions for each region followed the mathematical form of Eq.(1), without a particular integral, since no distributed load was applied to the structure.

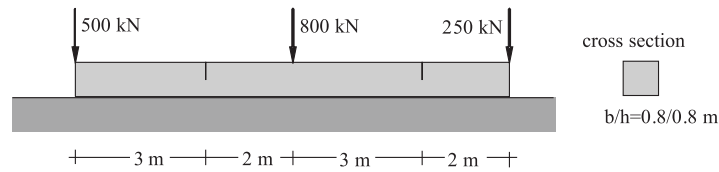


Figure 2. First example setup.

3.2 LOAD CASE 1: RESULTS AND DISCUSSION

The following functions for transverse displacements of the axis were obtained from the system of 16 linear

algebraic equations (resulting from four coupled governing differential equations, GDE), by the implementation of mechanical boundary conditions, as well as continuity conditions:

$$w_1(x) = e^{-0.306957 \cdot x} \cdot \left((-7.650490 \cdot 10^{-3} - 6.202263 \cdot 10^{-4} \cdot e^{0.613913 \cdot x}) \cdot \cos(0.306957 \cdot x) - (3.218247 \cdot 10^{-4} + 3.218247 \cdot 10^{-4} \cdot e^{0.613913 \cdot x}) \cdot \sin(0.306957 \cdot x) \right) \quad 0 \leq x \leq 3 \text{ m}$$

$$w_2(x) = e^{-0.306957 \cdot x} \cdot \left((-5.454747 \cdot 10^{-3} - 5.727759 \cdot 10^{-4} \cdot e^{0.613913 \cdot x}) \cdot \cos(0.306957 \cdot x) - (2.253137 \cdot 10^{-5} + 6.699410 \cdot 10^{-4} \cdot e^{0.613913 \cdot x}) \cdot \sin(0.306957 \cdot x) \right) \quad 3 \leq x \leq 5 \text{ m}$$

$$w_3(x) = e^{-0.306957 \cdot x} \cdot \left((8.266908 \cdot 10^{-3} + 1.121122 \cdot 10^{-4} \cdot e^{0.613913 \cdot x}) \cdot \cos(0.306957 \cdot x) - (1.476991 \cdot 10^{-2} + 3.268873 \cdot 10^{-5} \cdot e^{0.613913 \cdot x}) \cdot \sin(0.306957 \cdot x) \right) \quad 5 \leq x \leq 8 \text{ m}$$

$$w_4(x) = e^{-0.306957 \cdot x} \cdot \left((7.586349 \cdot 10^{-3} + 1.623280 \cdot 10^{-4} \cdot e^{0.613913 \cdot x}) \cdot \cos(0.306957 \cdot x) - (7.949772 \cdot 10^{-3} + 2.767785 \cdot 10^{-5} \cdot e^{0.613913 \cdot x}) \cdot \sin(0.306957 \cdot x) \right) \quad 8 \leq x \leq 10 \text{ m}$$

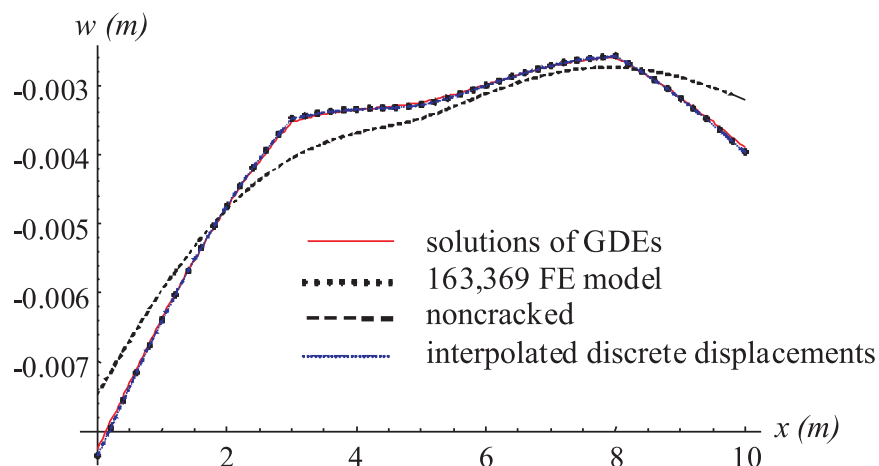


Figure 3. Comparison of transverse displacements.

The transverse displacements along the axis of the structure obtained by GDEs were compared to the discrete values obtained from the FE mesh, and are presented in Fig. 3, where only small discrepancies are noticeable. The transverse displacements for the non-cracked structure are also shown, exclusively to emphasize the effect of the introduced cracks.

The stress distribution at the soil surface can be obtained directly by multiplying the transverse displacements by the constant of proportionality. Fig. 4, therefore, shows the complete beam in the deformed state with the distance between the nodes being approximately 1 cm. It is obvious from Fig. 4 that the deformed curve of the contact surface is smooth and without any significant variations.

The same behaviour is evident, even in the vicinities of both cracks, Fig. 5 and, consequently, it can be concluded that strong local variations of the soil stresses are not actually presented.

It is further evident from Fig. 5 that open cracks do not exhibit any unexpected behaviour.

The differences between the displacements from both models were additionally examined since the transverse displacements represent a foundation for a further analysis of the inner forces and the bending moments. Fig. 6 shows the discrepancies in the results from both computational models at some discrete points along the structure. As expected, slightly larger discrepancies appeared at all the positions of the local effects (applied transverse loads and cracks). The average discrepancy was slightly below 0.77 %, with a maximum positive discrepancy of 2.01 % appearing at the right-end, and a maximum negative discrepancy of 2.09 % appearing at the left crack. It should be mentioned that the non-cracked situation was also considered, bringing the average discrepancy slightly below 0.37 %, with a maximum discrepancy of 1.19 % appearing at the mid-span. This proves that the discrepancies for the cracked situation do not originate solely from the applied simplified model.

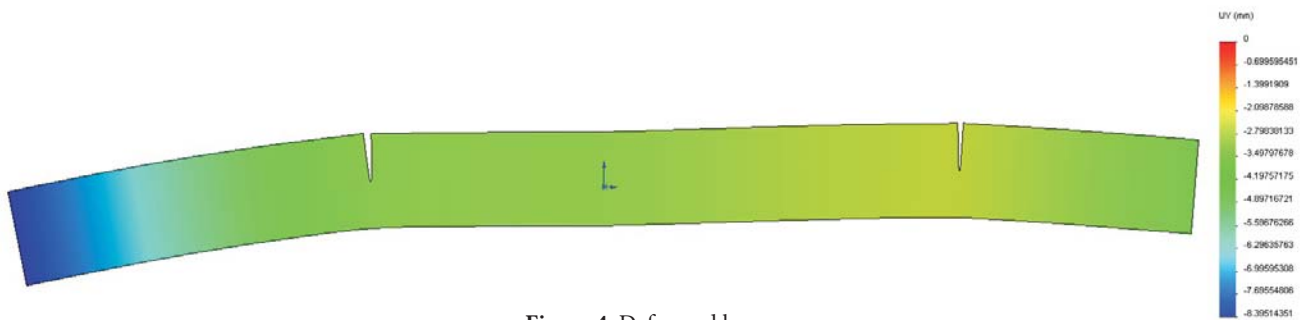


Figure 4. Deformed beam.

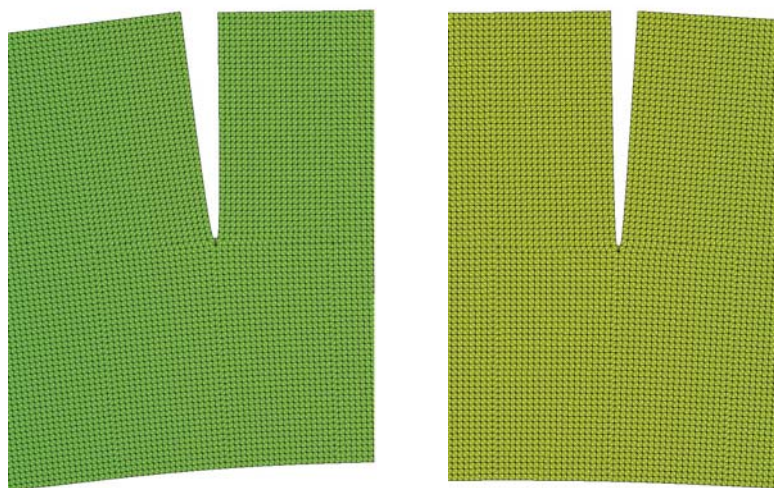


Figure 5. Details of the beam deformed state in the vicinity of the cracks.

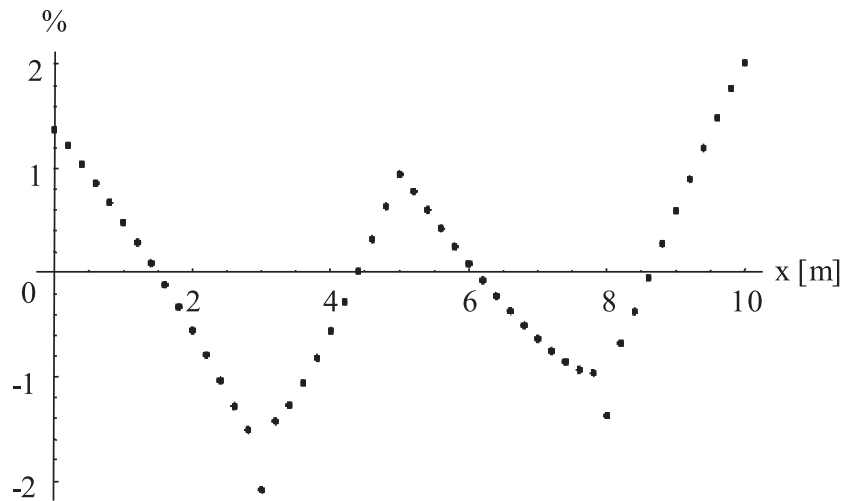


Figure 6. Discrepancies in transverse displacements.

Afterwards, the solution of GDEs allowed the bending moments to be evaluated analytically along the structure by implementing the second derivatives of the transverse displacement functions. The results obtained with this approach coincide completely at every point with the values obtained from the simple equilibrium conditions of the rotations.

Furthermore, the bending moment values from the 2D FE model were additionally required in order to provide a reliable assesment of the obtained results. Two unrelated approaches were conducted, since the bending moment values could not be retrieved directly from the 2D FE computational model. In the first approach, polynomial interpolation was utilized individually for all four regions in order to construct transverse displace-

ment functions within the range of each discrete set of evaluated displacements (presented in Fig. 3). When using a polynomial interpolation, the interpolant is a polynomial and, thus, infinitely differentiable, which then made it possible to determine the bending-moment functions. However, although the matching of the transverse displacement functions was excellent and completely without any oscillatory artefacts, these negative effects become more than just evident at the end points of all four bending-moment functions, Fig. 7 (dashed line). Consequently, the interpolated transverse displacement functions were exclusively implemented within the equilibrium conditions of the rotations, thus providing results (dotted line) in excellent agreement with GDEs solutions from the simplified computational model (solid line).

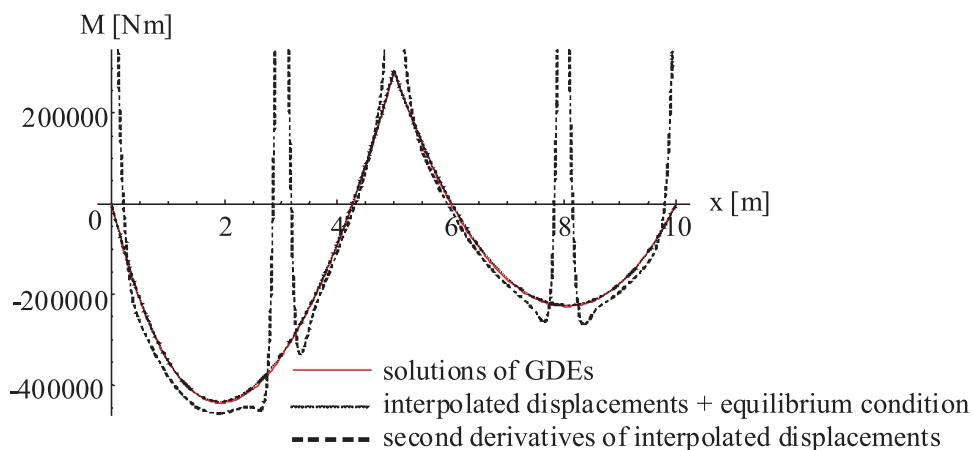


Figure 7. Comparison of bending moments.

In the second approach, the moments of normal stresses from the 2D FE model were numerically integrated in several selected transverse sections in order to construct bending moments. This approach produced values that were completely independent of the obtained displacements. Special attention was paid to those locations where the local stress singularities were caused by the applied concentrated loads or cracks, primarily due to the fact that the stresses were actually obtained in Gauss integration points within the finite elements, and their nodal values were further obtained by extrapolation, automatically executed by the original algorithm of the FE software. Nevertheless, an excellent agreement of the results from both computational models was clearly proved when comparing the integrated values (discrete dots in Fig. 8) to the values obtained from the GDEs (solid line). The discrepancy in the results at the position of the maximum negative (hogging) moment (located between the left end and left crack) was 0.98 %, while at the position of maximum positive (sagging) moment (located at the mid-span), the discrepancy was 1.51 %.

The discrepancies at the cracks' locations were 1.71 % and 1.17 % for the left- and right-hand cracks, respectively.

An identical situation was also detected when the shear forces were studied and all four computational techniques were implemented. Again, both computations based on GDEs solutions of the simplified model (the third derivative of transverse displacements, as well as the applied vertical equilibrium) produced identical results (red solid line in Fig. 9). Furthermore, the first solution based on the discrete displacements from the FE model, i.e., the implementation of the interpolated displacements within the condition of the vertical equilibrium, again provided an exceptional agreement with the first two approaches (dashed line). Like with the bending moments, the integration of the shear stresses from the FE model at certain selected cross-sections (discrete dots) again produced excellent matching of the results, even at the centre of the structure, where a concentrated transverse load was applied and, consequently, an abrupt change in the shear forces was expected.

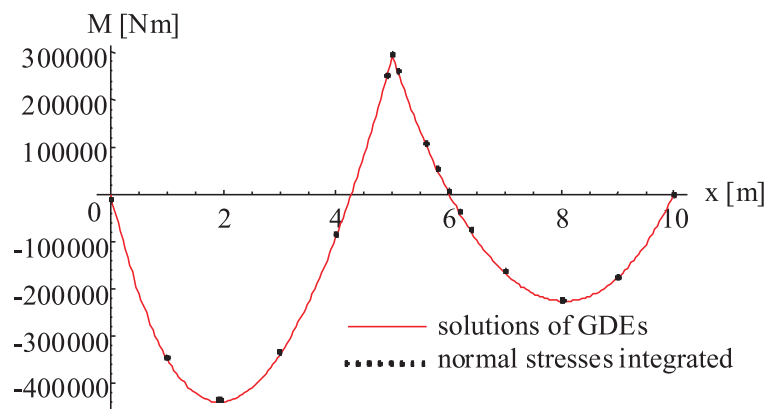


Figure 8. Comparison of bending moments.

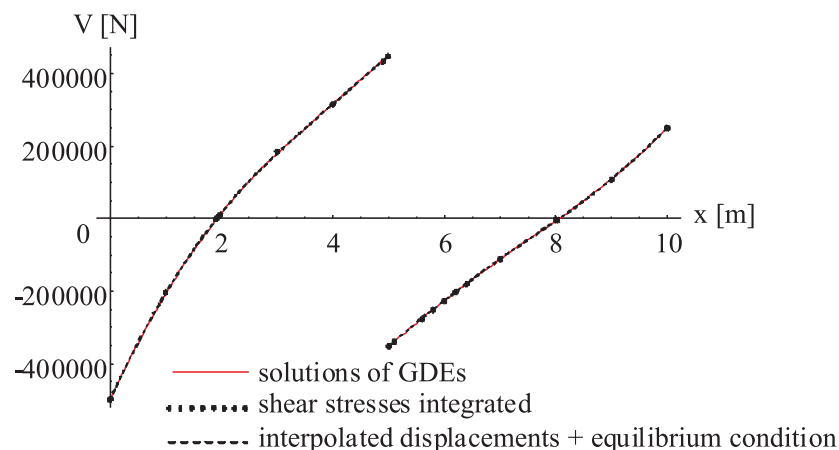


Figure 9. Comparison of shear forces.

The discrepancy of the results at the position of the maximum negative shear force (located at the left-end) was 0.12 %, while at the position of the maximum positive shear force (located at the left-hand side of the midspan) the discrepancy was 0.28 %.

3.3 LOAD CASE 2: THREE CONCENTRATED DOWNWARD FORCES AND TWO UNIFORM TRANSVERSE LOADS

In the second load case, three vertical downward transverse forces from the first load situation remained on the structure; however, both side forces were shifted by 20 cm towards the centre of the beam. Furthermore, two uniform transverse continuous loads were applied. The downward uniform load of 50 kN/m was applied in the region between the left-end and the mid-span of the structure, while the remainder of the element was loaded by a downward uniform load of 75 kN/m, Fig. 10.

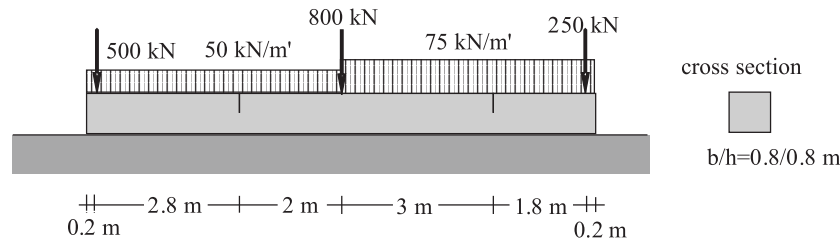


Figure 10. Second example setup.

3.4 LOAD CASE 2: RESULTS AND DISCUSSION

Since the structure had two cracks and three concentrated in-field transverse loads, the corresponding computational model of the considered load combination consisted of six elastic segments. Consequently, six coupled functions for six elastic regions had to be analyzed in order to obtain the vertical displacement distributions along the structure. Since the distributed load was applied to each part of the structure, the interpolation function for each region followed the mathematical form of Eq.(2), with the particular integral equal to $-q/k$.

The following functions for the transverse displacements were obtained from a system of coupled governing differential equations (GDEs) by the implementation of mechanical boundary conditions, as well as the continuity conditions:

$$w_1(x) = e^{-0.306957 \cdot x} \cdot (-5.032285 \cdot 10^{-3} \cdot \cos(0.306957 \cdot x) + 1.250409 \cdot 10^{-3} \cdot \sin(0.306957 \cdot x)) - 1.25 \cdot 10^{-3} \\ + e^{0.306957 \cdot x} \cdot (-2.531466 \cdot 10^{-3} \cdot \cos(0.306957 \cdot x) + 1.250409 \cdot 10^{-3} \cdot \sin(0.306957 \cdot x)) \quad 0 \leq x \leq 0.2 \text{ m}$$

$$w_2(x) = e^{-0.306957 \cdot x} \cdot (-6.943232 \cdot 10^{-3} \cdot \cos(0.306957 \cdot x) - 9.108504 \cdot 10^{-4} \cdot \sin(0.306957 \cdot x)) - 1.25 \cdot 10^{-3} \\ + e^{0.306957 \cdot x} \cdot (-6.199267 \cdot 10^{-4} \cdot \cos(0.306957 \cdot x) - 4.397391 \cdot 10^{-4} \cdot \sin(0.306957 \cdot x)) \quad 0.2 \leq x \leq 3 \text{ m}$$

$$w_3(x) = e^{-0.306957 \cdot x} \cdot (-5.003725 \cdot 10^{-3} \cdot \cos(0.306957 \cdot x) - 6.464836 \cdot 10^{-4} \cdot \sin(0.306957 \cdot x)) - 1.25 \cdot 10^{-3} \\ + e^{0.306957 \cdot x} \cdot (-5.780136 \cdot 10^{-4} \cdot \cos(0.306957 \cdot x) - 7.472313 \cdot 10^{-4} \cdot \sin(0.306957 \cdot x)) \quad 3 \leq x \leq 5 \text{ m}$$

$$w_4(x) = e^{-0.306957 \cdot x} \cdot (8.770142 \cdot 10^{-3} \cdot \cos(0.306957 \cdot x) - 1.394470 \cdot 10^{-2} \cdot \sin(0.306957 \cdot x)) - 1.875 \cdot 10^{-3} \\ + e^{0.306957 \cdot x} \cdot (1.092993 \cdot 10^{-4} \cdot \cos(0.306957 \cdot x) - 4.267824 \cdot 10^{-5} \cdot \sin(0.306957 \cdot x)) \quad 5 \leq x \leq 8 \text{ m}$$

$$w_5(x) = e^{-0.306957 \cdot x} \cdot (8.213005 \cdot 10^{-3} \cdot \cos(0.306957 \cdot x) - 8.361426 \cdot 10^{-3} \cdot \sin(0.306957 \cdot x)) - 1.875 \cdot 10^{-3} \\ + e^{0.306957 \cdot x} \cdot (1.504083 \cdot 10^{-4} \cdot \cos(0.306957 \cdot x) - 3.857611 \cdot 10^{-5} \cdot \sin(0.306957 \cdot x)) \quad 8 \leq x \leq 9.8 \text{ m}$$

$$w_6(x) = e^{-0.306957 \cdot x} \cdot (3.004931 \cdot 10^{-2} \cdot \cos(0.306957 \cdot x) + 8.306926 \cdot 10^{-3} \cdot \sin(0.306957 \cdot x)) - 1.875 \cdot 10^{-3} \\ + e^{0.306957 \cdot x} \cdot (1.097615 \cdot 10^{-4} \cdot \cos(0.306957 \cdot x) + 1.467303 \cdot 10^{-5} \cdot \sin(0.306957 \cdot x)) \quad 9.8 \leq x \leq 10 \text{ m}$$

The transverse displacements along the axis of the structure obtained by the GDEs were compared to the discrete values obtained from the FE mesh, as presented in Fig. 11, where only small discrepancies are noticeable. The transverse displacements for the non-cracked structure are also shown, exclusively to emphasize the effect of the introduced cracks.

The differences between the displacements from both models were further examined. Figure 12 shows the discrepancies in the results from both computational models at some discrete points along the structure. Again, extreme local discrepancies appeared at all positions regarding local effects (applied transverse loads and cracks). Compared to the first load case, the average discrepancy was even better, i.e., slightly below

0.5 %. Furthermore, both of the obtained extreme values were also lower. A maximum positive discrepancy of 1.18 % and a maximum negative discrepancy of 1.33 % again appeared at the same points: at the right-end and the left-crack, respectively. It should also be noted that, for the considered load case, the discrepancy at the right-crack also decreased, while at the left-end of the structure the discrepancy remained almost identical, when compared to the first load case.

The bending moments were evaluated analytically along the structure by implementing the second derivatives of the transverse displacement functions from the solutions of the GDEs. The results obtained with this approach at every point coincided completely with those values obtained from the simple equilibrium conditions of the rotations.

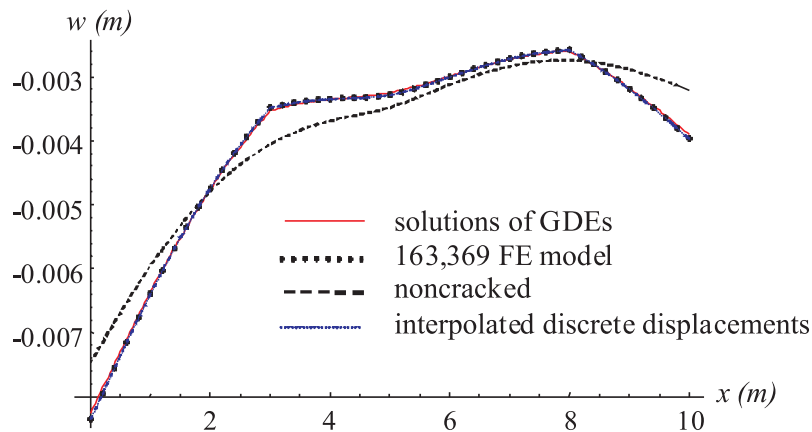


Figure 11. Comparison of transverse displacements.

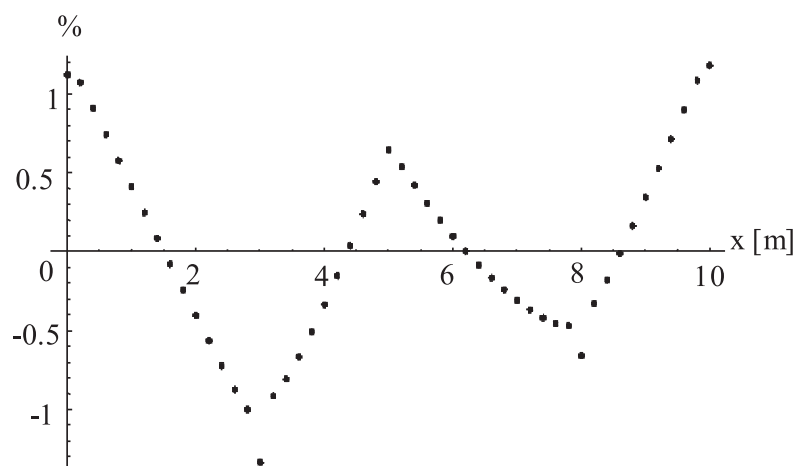


Figure 12. Discrepancies of transverse displacements.

As in the first load case, the displacement results from the 2D FE model were additionally implemented in two approaches for the comparative evaluation of the bending moments. In the first approach a polynomial interpolation was again utilized individually for all six regions in order to construct the transverse displacement functions within the range of each discrete set of evaluated displacements. However, it transpired that the transverse displacements for both short-ending regions can also be completely and adequately described by those functions belonging to the next neighbouring region. The interpolated functions were afterwards implemented within the equilibrium conditions of the rotations, providing results (dotted line) in excellent agreement with GDEs solutions from the simplified computational model (solid line), Fig. 13. In the second approach, the moments of the normal stresses from the discrete points of the FE model were numerically integrated within several selected transverse sections in

order to construct the bending moments (discrete dots in Fig. 11), again proving the quality of the results from the simplified model.

The discrepancy in the results at the position of the maximum negative (hogging) moment (located between the left-end and left-crack) was 1.07 %, whilst at the position of the maximum positive (sagging) moment (located at the mid-span) the discrepancy was 1.21 %. The discrepancies at the crack locations were 1.69 % and 1.13 % for the left and right-cracks, respectively.

The shear forces were additionally studied, implementing all four computational techniques. As expected, both computations based on the GDEs solutions of the simplified model (the third derivative of the transverse displacements, as well as the applied vertical equilibrium) produced identical results (red solid line in Fig. 14). Furthermore, the first solution based

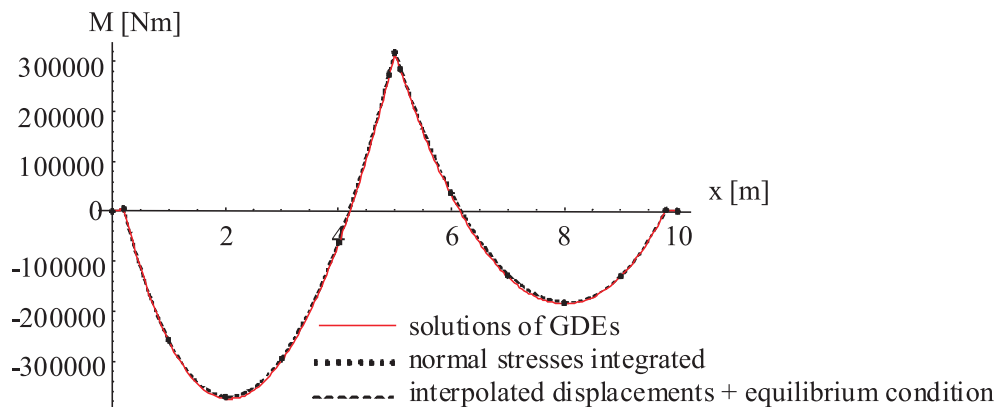


Figure 13. Comparison of bending moments.

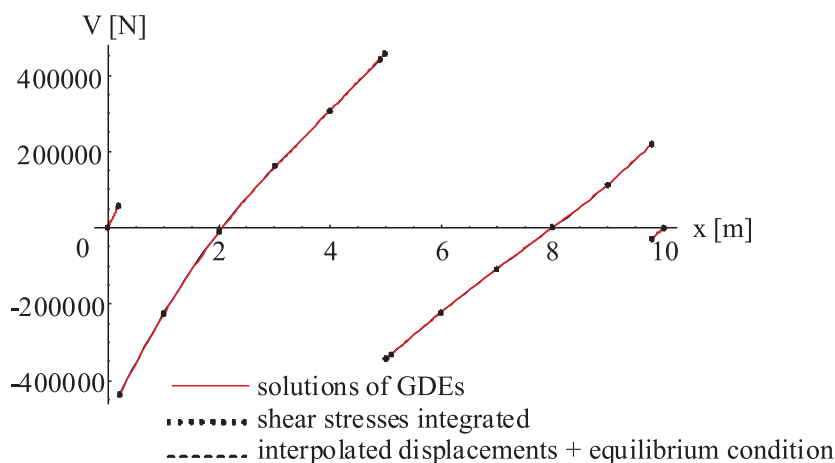


Figure 14. Comparison of shear forces.

on the discrete displacements from the FE model, i.e., the implementation of the interpolated displacements within the condition of the vertical equilibrium, again provided an exceptional agreement with the first two approaches (dashed line). Finally, the integration of the shear stresses at certain selected isolated cross-sections (discrete dots) again produced an excellent matching of the results, even within the positions of the concentrated transverse loads, where abrupt changes in the shear forces clearly appeared.

The discrepancy in the results at the position of the maximum negative shear force (located at the right-side of the left transverse force) was 1.59 %, while at the position of the maximum positive shear force (located at the left-side of the mid-span) the discrepancy was 0.30 %.

4 CONCLUSIONS

Okamura's simplified computational model of cracked beams was implemented to evaluate the transverse displacements and inner forces for transversely cracked slender beams resting on Winkler's foundation. The transverse displacements were firstly evaluated from solutions of coupled differential equations, while the implementation of well-known relationships from the Euler-Bernoulli beam theory further allowed for the bending moments and shear forces to be computed.

The results obtained with the discussed approach were afterwards compared to the results obtained from the pure numerical approach implementing parabolic triangular-shell finite elements within the framework of the finite-elements method. Despite the clear computational differences between both approaches, the considered examples showed that the application of the simplified model produces excellent matching results. The proposed computational model has also proved itself to be useable for beams on Winkler's foundation, as the discrepancies in the results obtained with this approach compared with the results obtained with much more complex and time-consuming 2D finite-elements models are just up to 2.2 %, despite the enormous differences in the computational effort. Furthermore, the transverse displacement solutions obtained from differential equations are given in analytical form, which allows for a straightforward further analysis of the bending moments and shear forces.

The proposed approach thus yields an adequate, as well as accurate, approach for the modelling of cracked beam structures in engineering situations where the cracks have to be considered during the analysis.

REFERENCES

- [1] Okamura H., Liu H.W., Chorong-Shin C. (1969). A cracked column under compression, *Eng. Frac. Mech.* 1, 547-564.
- [2] Ostachowicz W.M., Krawczuk M. (1990). Vibrational analysis of cracked beam, *Comp. and Struc.* 36-22, 245-250.
- [3] Dimarogonas A.D., Papadopoulos C.A. (1983). Vibration of cracked shafts in bending, *J. Sound Vib.* 91(4), 583-593.
- [4] Rajab M.D., Al-Sabeeh A. (1991). Vibrational characteristics of cracked shafts, *J. Sound and Vib.* 147(3), 465-473.
- [5] Krawczuk M., Ostachowicz W.M. (1993). Influence of a crack on the dynamic stability of a column, *J. Sound Vib.* 167(3), 541-555.
- [6] Sundermayer J.N., Weaver R.L. (1993). On crack identification and characterization in a beam by nonlinear vibration analysis, *Theoretical and applied mechanics*, TAM Report No. 743, UIIU-ENG-93-6041.
- [7] Hasan W.M. (1995). Crack detection from the variation of the eigenfrequencies of a beam on elastic foundation, *Eng. Frac. Mec.* 52(3), 409-421.
- [8] Skrinar M., Pliberšek T. (2004). New linear spring stiffness definition for displacement analysis of cracked beam elements, *Proc. Applied. Math. Mechanics* 4, 654-655.
- [9] Shifrin E.I., Ruotolo R. (1999). Natural frequencies of a beam with an arbitrary number of cracks, *J. Sound Vib.* 222, 409-423.
- [10] Khiem N.T., Lien T.V. (2001). A simplified method for natural frequency analysis of a multiple cracked beam, *J. Sound Vib.* 245, 737-751.
- [11] Li Q.S. (2002). Free vibration analysis of non-uniform beams with an arbitrary number of cracks and concentrated masses, *J. of Sound Vib.*, 252, 509-525.
- [12] Fernández-Sáez J., Navarro C. (2002). Fundamental frequency of cracked beams in bending vibrations: an analytical approach, *J. Sound and Vib.* 256(1), 17-31.
- [13] Rizos P.F., Aspraghtas N., Dimarogonas A.D. (1990). Identification of crack location and magnitude in a cantilever beam from the vibration modes, *J. Sound Vib.* 138, 381-388.
- [14] Boltežar M., Štrancar B., Kuhelj A. (1998). Identification of transverse crack location in flexural vibrations of free-free beams, *J. Sound Vib.* 211(5), 729-734.
- [15] Vestroni F., Capecchi D. (2000). Damage detection in beam structures based on frequency measurements, *J. Eng. Mech.* 126, 761-768.

- [16] Bamnios Y., Douka E., Trochidis A. (2002). Crack identification in beam structures using mechanical impedance, *J. Sound Vib.* 256(2), 287-297.
- [17] Gounaris G., Dimarogonas A.D. (1988), A finite element of a cracked prismatic beam for structural analysis, *Comp. Struc.* 28(3), 301-313.
- [18] Skrinar M., Umek A. (1996). Plane beam finite element with crack, *J. Gradbeni vestnik (in Slovenian)* 1&2, 2-7.
- [19] Skrinar M. (2007). On the application of a simple computational model for slender transversely cracked beams in buckling problems, *Comput. mater. sci.* 39(1), 242-249.
- [20] Krawczuk M., Źak A., Ostachowicz W. (2000). Elastic beam finite element with a transverse elastoplastic crack, *Finite Elem. Anal. Design* 34, 61-73.
- [21] Kisa M., Brandon J. (2000). The effects of closure of cracks on the dynamics of a cracked cantilever beam, *J. Sound Vib.* 238(1), 1-18.
- [22] Skrinar M. (2009). Elastic beam finite element with an arbitrary number of transverse cracks, *Finite Elem. Anal. Des.* 45(3), 181-189.
- [23] Caddemi S., Caliò I. (2008). Exact solution of the multi-cracked Euler-Bernoulli column, *International J. of Solids and Structures* 45 (16), 1332-1351.
- [24] Biondi B., Caddemi S. (2007). Euler-Bernoulli beams with multiple singularities in the flexural stiffness, *European J. Mechanics A/Solids* 26 (5), 789-809.
- [25] Biondi B., Caddemi S. (2005). Closed form solutions of Euler-Bernoulli beams with singularities, *J. of Solids and Structures* 42, 3027-3044.
- [26] Jones G. (1997). *Analysis of beams on elastic foundations: using finite difference theory*, Thomas Telford.
- [27] Chen C. N. (1998). Solution of beam on elastic foundation by DQUM. *Journal of Engineering Mechanics*, December, 1381-1384.
- [28] Onu G. (2000). Shear effect in beam finite element on two-parameter elastic foundation. *Journal of Engineering Mechanics*, September, 1104-1107.
- [29] Guo Y. J. and Weitsman Y. J. (2002). Solution method for beams on nonuniform elastic foundations. *Journal of Engineering Mechanics*, American Society of Civil Engineers, 128, No. 5, May, 592-594.
- [30] Al-Azzawi A. A., Mahdy A. H., Farhan O. Sh. (2010), Finite element analysis of deep beams on nonlinear elastic foundations, *Journal of the Serbian Society for Computational Mechanics*, Vol. 4, No. 2, 13-42.
- [31] Cerioni R., Mingardi L. (1996). Nonlinear analysis of reinforced concrete foundation plates, *Computers & Structures*, 61, 1, 87-106.
- [32] Melerski E. S. (2000). *Design Analysis of Beams, Circular Plates and Cylindrical Tanks on Elastic Foundations: With IBM Compatible Software – Hardcover*, Balkema, A. A. Publishers.
- [33] Oden J. T. (1967). *Mechanics of elastic structures*, New York: McGraw-Hill.
- [34] Selvadurai A.P.S. (1979). *Elastic analysis of soil-foundation interaction*, Elsevier Scientific Pub. Co., Amsterdam.
- [35] Vestroni F. (2009). *Lecture notes from the course Dynamical Inverse Problems: Theory and Application*, Udine.

BOČNA NOSILNOST KRATKIH TOGIH PILOTOV V DVOSLOJNIH NEVEZLJIVIH TLEH

ERDAL UNCUOĞLU İN MUSTAFA LAMAN

o avtorjih

vodilni avtor

Erdal Uncuoğlu
Erciyes University,
Civil Engineering Department
38039 Talas / Kayseri, Turčija
E-pošta: erdalu@erciyes.edu.tr

Mustafa Laman
Osmaniye Korkut Ata University,
Civil Engineering Department
80000, Osmaniye, Turčija
E-pošta: mustafalaman@osmaniye.edu.tr

izvleček

V članku je predstavljena raziskava bočno obteženih kratkih pilotov v dvoslojnih peskih. Za ta namen je bil izveden niz modelnih preizkusov na modelih pilotov. Z izvedbo niza tridimenzionalnih nelinearnih analiz s končnimi elementi so bili raziskani učinki elastičnega modula, dilatacije in interakcije peska in pilota. Bočne nosilnosti pilotov v pogojih slojevitih peščenih tal so bile izračunane z metodami Brinch Hansen (1961) ter Meyerhof idr. (1981). Med seboj so bili primerjani rezultati dobljeni z eksperimentalnimi študijami, numeričnimi analizami in konvencionalno metodo.

Rezultati so pokazali, da imajo preiskovani parametri precejšen učinek na obnašanje bočno obteženih kratkih togih pilotov. Prikazano je tudi, da vrednost mejne bočne nosilnosti pomembno varira glede na uporabljeno metodo.

ključne besede

bočna obtežba, kratek pilot, dvoslojen pesek, modelni preizkus, končni element, bočna efektivna napetost

LATERAL RESISTANCE OF A SHORT RIGID PILE IN A TWO-LAYER COHESIONLESS SOIL

ERDAL UNCUOĞLU İN MUSTAFA LAMAN

about the authors

corresponding author

Erdal Uncuoğlu
Erciyes University,
Civil Engineering Department
38039 Talas / Kayseri, Turkey
E-mail: erdal@erciyes.edu.tr

Mustafa Laman
Osmaniye Korkut Ata University,
Civil Engineering Department
80000, Osmaniye, Turkey
E-mail: mustafalaman@osmaniye.edu.tr

abstract

The behavior of a laterally loaded short rigid pile founded in a two-layer sand soil profile has been investigated. For this purpose, a series of model tests were carried out on model piles. The effects of the elasticity modulus, dilatancy and interface behavior of the sand have been explored numerically by performing a series of three-dimensional non-linear finite-element analyses. The lateral load capacities in the layered sand conditions have been calculated using the methods proposed by Brinch Hansen (1961) and Meyerhof et al. (1981). The results obtained from experimental studies, numerical analyses and a conventional method were compared with each other. The results proved that the parameters investigated had a considerable effect on the behavior of short rigid piles subjected to lateral loads. It was also shown that the value of the ultimate lateral load capacity could vary significantly, depending on the methods used.

keywords

lateral load, short pile, two-layered sand, model test, finite element, lateral effective stress

1 INTRODUCTION

Short piles or pier foundations that have a large diameter are widely used to support structures such as transmission towers, advertisement and information posts, overhead catenary systems carrying electrical power in railway networks and water towers. These structures have to withstand significant lateral loads and overturning moments, but relatively small vertical forces, which as a consequence are often neglected.

The behavior of piles subjected to lateral loads is governed by the interaction between the pile and the soil, and it is a non-linear three-dimensional soil-structure interaction problem. The soil's stress-strain behavior, including shear strength, stiffness and volume change characteristics and soil-pile interface, plays an important role in the response of piles subjected to lateral loads [1]. For that reason, in pile foundations the load-transfer mechanism is so complex and not fully understood yet [2].

In recent years, experimental model studies including the 1g model and centrifugal model tests were made on model short rigid piles in homogeneous soil conditions [3, 4, 5, 6, 7, 8, 9, 10, 11]. However, the majority of the existing design methods related to laterally loaded short rigid piles [12, 13, 14, 15, 16], except the methods proposed by Brinch Hansen [12] and Meyerhof et al. [14], are valid only for homogeneous soil conditions. There are numerous studies in the literature concerned with the application of the finite-element method for piles subjected to lateral loads [1, 2, 17, 18, 19, 20, 21, 22, 23, 24]. Most of the studies mentioned have been performed on long flexible piles in homogeneous soil conditions.

On the other hand, most of the soil deposits are a layered system and in reality piles are often embedded in layered soils. There are a few studies in the literature based on numerical analyses related to flexible piles subjected to lateral loads in layered soils [25, 26, 27]. Also, there is

limited information in the literature that attempted to explore the behavior of short rigid piles subjected to lateral loading in layered soil deposits and to investigate the factors affecting the lateral load capacity of short rigid piles in layered soils.

In this study, the behavior of a short rigid pile subjected to a lateral loading in a two-layer sand soil profile of different densities and thickness is investigated. For this purpose, a series of model test studies was carried out on model piles founded in homogeneous loose, homogeneous dense and two-layered sand conditions. The model tests were analyzed by a three-dimensional non-linear finite-element method. Initially, in the numerical studies, a parametric study was performed in order to explore the effect of some parameters, such as the elasticity modulus, dilatancy and interface behavior of the sand on the lateral load capacity of short rigid piles. After the determination of the parametric values, model test studies were analyzed under the experimental ultimate lateral load capacities for each of the soil conditions considered to evaluate the failure regions developed around the pile and the distribution of the lateral effective stresses along the pile embedded depth under the experimental

conditions. Finally, the lateral load capacities and the distributions of the lateral effective stresses were calculated using the methods proposed by Brinch Hansen [12] and Meyerhof et al. [14]. Then, the results obtained from these conventional methods were compared with the experimental and numerical results of this study.

2 EXPERIMENTAL TESTING PROGRAM

The loading tests were carried out in a steel box container. The internal dimensions of the test box were 960×480 mm in plan and 500 mm in height. The two side walls of the box were 10-mm-thick glass and the other sides and base plate were a 20-mm-thick wooden plate. The dimensions of the test box were chosen to be large enough to minimize the influence of the box boundaries. The inside walls of the test box were smooth and therefore the side friction effect was minimal. The distance between the pile tip and the base plate of the box was five times that of the pile diameter. A schematic view of the model test set-up is shown in Fig. 1.

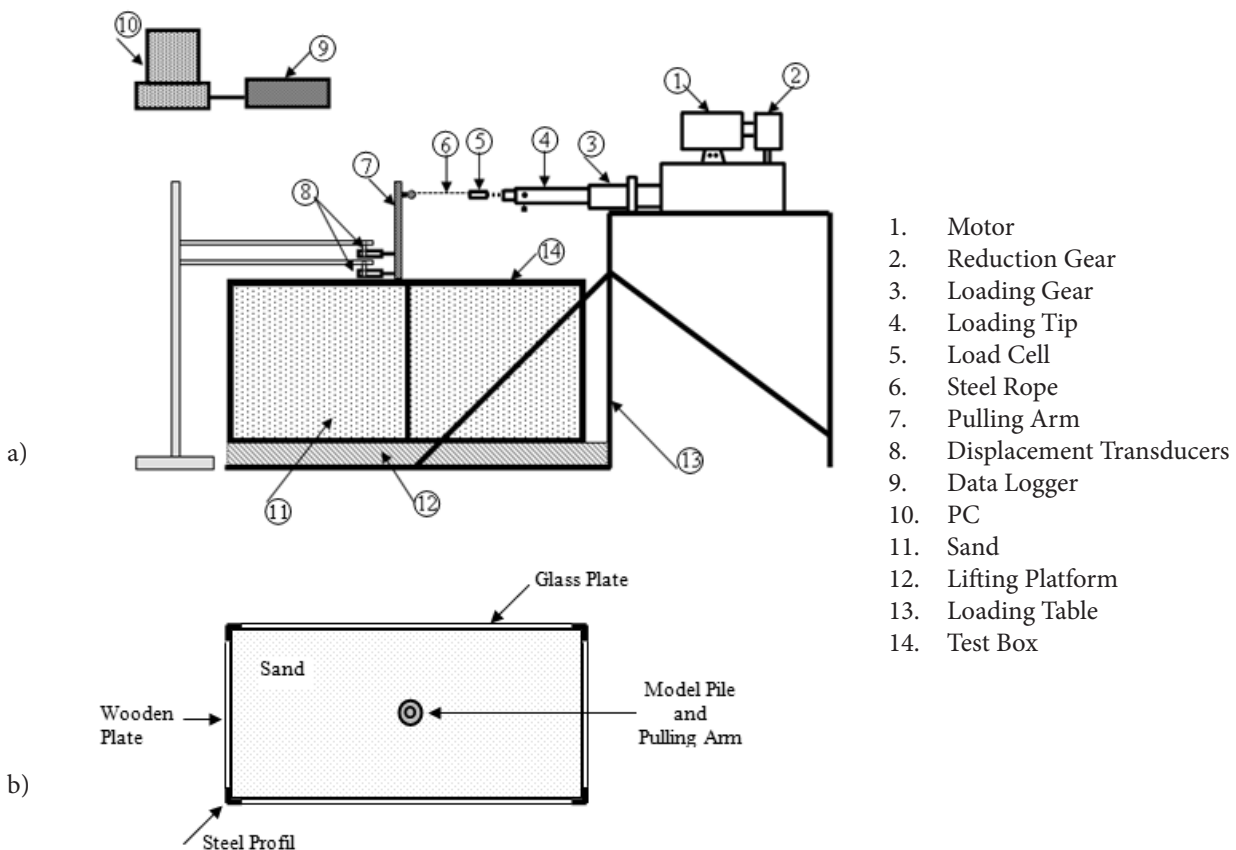


Figure 1. General layout of the apparatus for the model test: (a) side view (b) plan view.

The model tests were conducted on 1/20-scale model piles. A circular model pile with a diameter (D) of 50 mm and a length (L) of 200 mm was used in the tests. The model pile was fabricated from steel ($E_{pile}=210000$ MPa). The embedment ratio (L/D) of the pile was 4 in all the tests. A pulling arm, also fabricated from steel, with a diameter of 25 mm and a height of 330 mm was attached to the model pile, as seen in Fig. 2.

A short rigid pile can be described as one where the embedded length does not exceed ten times its lateral dimension [28]. On the other hand, Broms [13] showed that the embedment depth of a laterally loaded pile has to be less than $2T$ to behave as a rigid pile. In cohesionless soils, the value of the stiffness factor T is calculated as:

$$T = \sqrt[5]{\frac{E_{pile} I_{pile}}{n_h}} \quad (1)$$

where:

$E_{pile} I_{pile}$; bending stiffness of the pile,
 n_h ; coefficient of subgrade reaction.

The values of the coefficient of the subgrade reaction for the loose and dense conditions are 2200 and 17600 kN/m^3 , respectively [29]. The estimated $2T$ values are 0.987 and 0.651 for the loose and dense sand conditions, respectively. The $2T$ values indicate that the model pile satisfies the criterion valid for a short rigid pile.

The lateral load was applied at a height of 300 mm as a pulling force. The lateral load was imposed at a constant rate of displacement of 1 mm/min. via a steel cable linked to a motorized pulling mechanism. The lateral displacement of the pulling arm was measured using two linear variable differential transducers (LVDTs) attached at the elevations of 26 mm and 86 mm above the sand's surface. The lateral load was monitored by a 1-kN capacity load cell. The output from the load cell and transducers was fed to an ADU data logger. The data was converted using DIALOG software to produce the values of the lateral displacement and lateral load. The lateral load was applied until 10 mm of deflection occurred at the point that was 86 mm above the sand's surface.

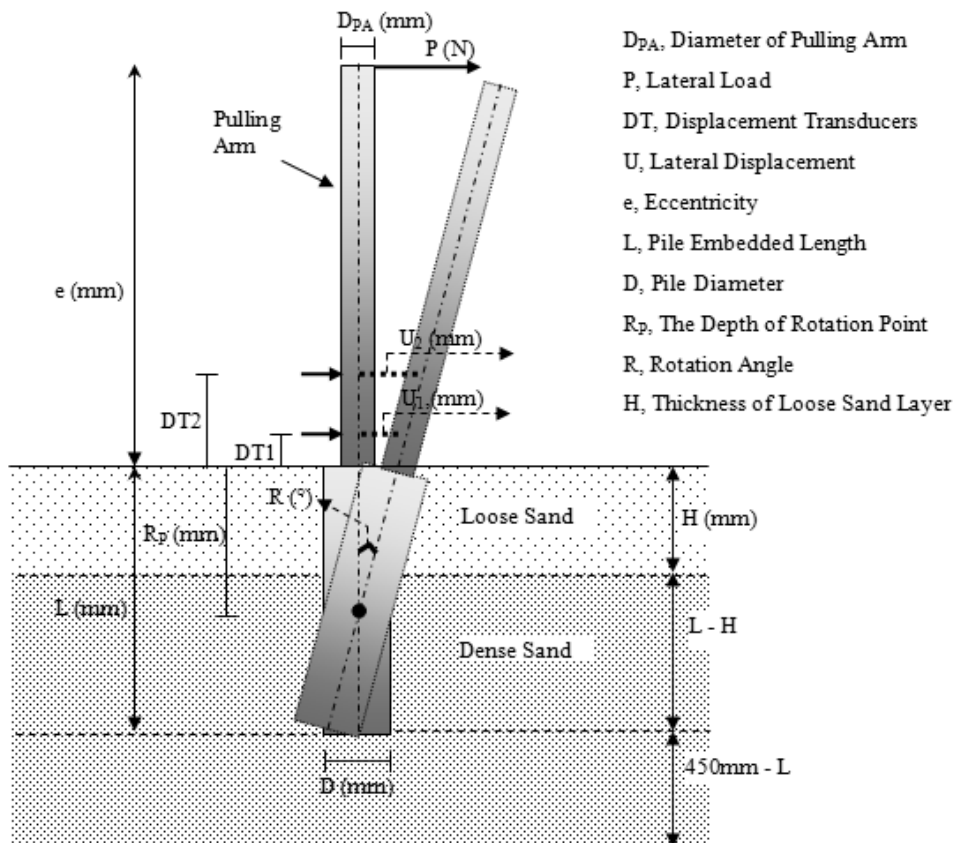


Figure 2. The geometry of the model system.

3 SOIL DESCRIPTION AND PREPARATION OF THE SAND BED

The model tests were performed in dry sand obtained from the Cakit river bed. The sand used in the tests was classified as poorly graded sand (*SP*). The effective grain size (D_{10}), uniformity coefficient (U_c) and the coefficient of curvature (U'_c) of the sand were 0.18 mm, 2.78 and 1.00, respectively. The model sand was prepared in the homogeneous loose, homogenous dense and layered sand conditions. The dry unit weights (γ_{dry}) of the sand were 15.03 kN/m³ and 17.06 kN/m³ for the loose and dense sand conditions, respectively. The internal friction angles (ϕ') obtained from triaxial compression tests were 38° and 44° for the loose and dense sand packings, respectively.

The sand was placed into the test box in layers of 30 mm thickness in both the loose and dense sand conditions. The required sand weights were calculated for each layer at the beginning of the experiment. For the loose state, the sand was poured into the test box from a height that is as close as possible and then the sand was spread out in the test box, utilizing the scale lines on the glass plates of the test box. For the dense state, in addition to the processes performed in the loose condition, each layer was compacted using a hand-held vibratory compactor. After the compaction, the thickness of the layer was controlled using the scale lines on the glass plates. When the preparation of the sand bed was completed up to the level of the pile tip, the model pile was placed at the centre of the test box, guided by an apparatus to assure centric vertical alignment. In this way the movement of the pile was also prevented. After securing the pile in place, sand was placed up to the top level of the pile.

4 TEST RESULTS

The ultimate lateral load capacity from lateral pile load tests is determined depending on the structure supported by the piles [30]. In the literature, different assumptions concerning with the ultimate lateral load capacity have

been used by different researchers. The assumptions made by researchers were generally based on the excessive lateral displacement of the pile head or the rotation of the pile [10]. On the other hand, some researchers defined the lateral load capacity of the pile from the load-displacement or moment-rotation curves as the point where the curve becomes linear or substantially linear [7, 8, 15]. Sawwaf [31] performed a series of laboratory model tests on rigid model piles to investigate the effect of reinforcing on the earth slope on the lateral behavior of a single vertical pile located near the slope. Sawwaf [31] defined the pile lateral capacities as the loads corresponding to the points wherein the lateral displacements of the pile equal to 10 and 20% of the pile diameter evaluating the effect of different parameters. In the present study, the lateral load corresponding to the lateral displacement equal to 10% of the pile diameter at the pile head was defined as the ultimate lateral load capacity.

In the experimental studies, five lateral loading tests were carried out to investigate the lateral behavior of a short rigid pile founded in layered sand deposits. The layered sand profile consisted of a loose sand layer overlying a dense sand layer, as encountered in most cases. The layer thicknesses were described using the H/L ratio. As shown in Fig. 2., H is the thickness of the loose sand layer and L is the embedded depth of the pile. The tests were performed for the ratio of $H/L=0.25, 0.50, 0.75$ and also for the homogenous loose (HL) and homogeneous dense (HD) sand conditions.

The experimental lateral load-lateral displacement relations at the pile head are presented in Fig. 3. The ultimate lateral load capacities ($P_{ultimate}$), the depths of the rotation point (R_D) and the rotation degrees (R) at the pile head for $u_{x=0}=5\text{mm}$ obtained from experiments for the homogeneous and layered sand conditions are summarized in Table 1. As seen in Table 1, the lateral load capacities obtained in the layered conditions decrease as the thickness of the upper loose sand layer increases. In addition, in the layered sand conditions, the depth of the rotation point (zero horizontal displacement point) moves towards the pile tip with an increasing thickness of the upper loose sand layer.

Table 1. Model test results.

	$HD = H/L=0$	$H/L = 0.25$	$H/L = 0.50$	$H/L = 0.75$	$HL=H/L=1$
$u_{x=0}$ (mm)	5	5	5	5	5
$P_{ultimate}$ (N)	56.641	46.249	24.576	16.149	10.299
R_D (%)	75.019	75.346	80.421	84.971	76.475
R (°)	1.893	1.888	1.766	1.670	1.854

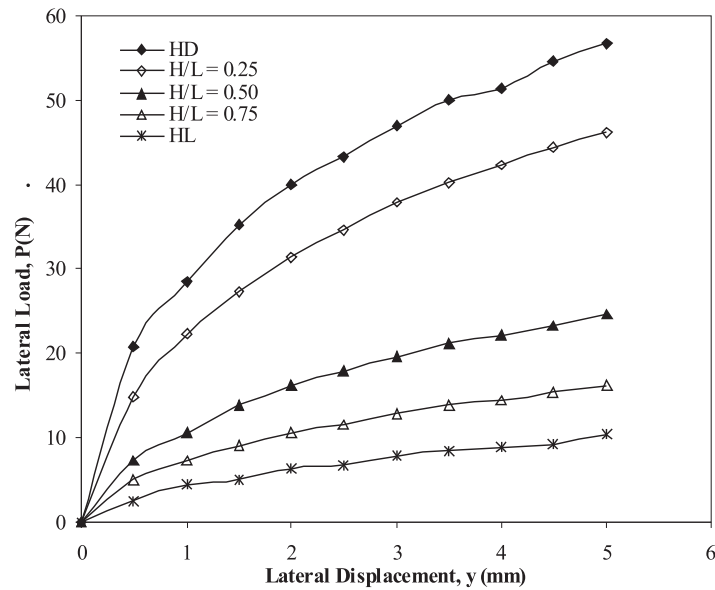


Figure 3. Experimental lateral load-lateral displacement relationships at the pile head.

As shown in Fig. 3., the experimental relations are non-linear and become softer with the increasing thickness of the loose sand layer. There is no observed peak strength in the experimental results shown in this figure. The lateral load capacity of the pile in the case of $H/L=0.25$ is 19% lower than the lateral load capacity obtained in the case of homogeneous dense sand. This ratio is 57% and 71% for the cases of $H/L=0.50$ and $H/L=0.75$, respectively. It is clear that the soil packing markedly effects the lateral load capacity of short rigid piles. The lateral load capacity of the pile in homogeneous dense sand is approximately five times that in homogeneous loose sand.

The ultimate lateral load capacity of short rigid pile is essentially provided by the mobilization of passive resistance in the soil; in other words, it is significantly dependent on ϕ' . The values of the lateral passive pressures acting on opposite faces above and below the rotation point will decrease as the thickness of the upper loose sand layer increases. The decrease in the lateral resistance is mainly due to the lower stiffness of the upper loose sand layer. In addition, the smaller unit weight of the loose sand results in smaller effective stresses in the dense sand layer compared with the condition of the homogeneous dense sand. On the other hand, in the layered sand condition, the presence of the dense sand layer caused the layered system to be stiffer than the homogeneous loose sand and increased the lateral load capacity significantly with respect to the case of the homogeneous loose sand. The reduction in the

lateral load capacity with respect to the value obtained in the case of the homogeneous dense sand is not directly proportional to the layer thicknesses.

If the $P_{ultimate}$ values are normalized using the weight of the pile (W_{pile}), a non-dimensional relationship between $P_{ultimate}/W_{pile}$ and H/L for values of H/L in the range 0~1 can be obtained. The relationship illustrated in Fig. 4. may be given by the following equation. The R^2 value of the equation was found to be 0.98.

$$P_{ultimate} = 1.45 e^{-1.79(H/L)} W_{pile} \quad (2)$$

Equation 2 was obtained as an approximation of the model test results performed in the experimental studies. This equation can be used only in the conditions valid in the model tests performed. This equation is not applicable for different soil conditions.

5 FINITE-ELEMENT ANALYSES

Finite-element (FE) studies of model tests of short rigid piles subjected to lateral loading with the same geometries and same soil conditions as in the model tests were carried out using the three-dimensional (3D) non-linear computer program PLAXIS 3D Foundation. The program is formulated using the displacement method and uses constitutive models based on plasticity theory.

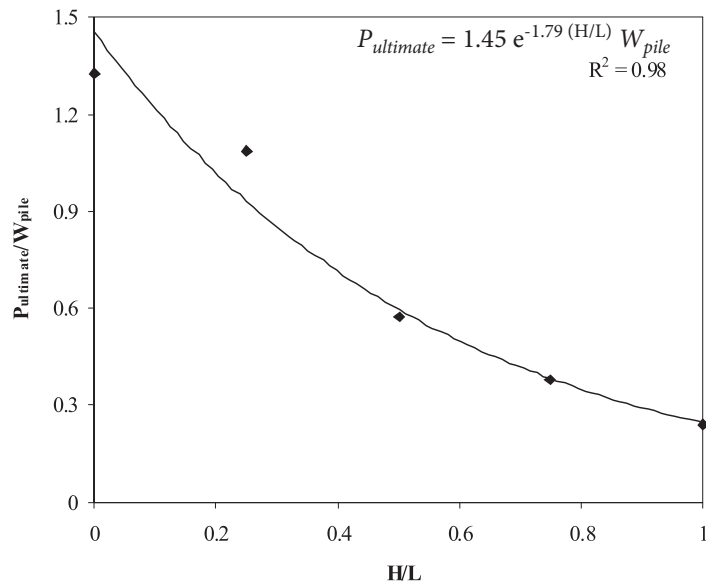


Figure 4. The non-dimensional relationship between the ultimate lateral load capacity and H/L .

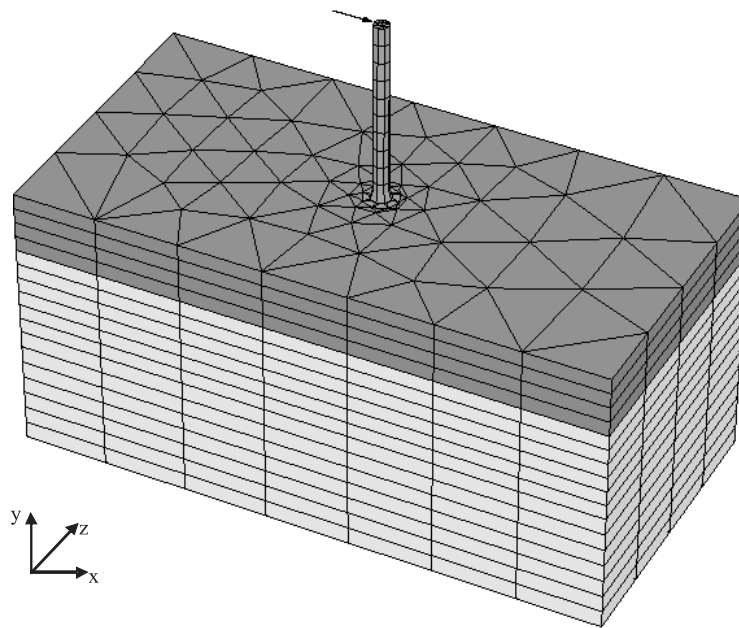


Figure 5. Three-dimensional finite-element mesh for layered sand condition.

The mesh density including the number of nodes, the number of elements and the average element size were defined after performing a series of trial analyses with several meshes of increasing refinement. The analyses were carried out until no significant changes were observed with further refinement. The medium-fine mesh density, which means the horizontal and vertical element distributions, respectively, was selected at the

end of the analyses. The selected mesh density is also refined using the additional horizontal planes called work planes in the vertical direction along the pile length in order to provide greater accuracy in the results. PLAXIS 3D Foundation refines the mesh automatically in the area surrounding the pile. Therefore, the size of the elements located around the pile was smaller. A typical mesh for 3D FE analyses in the case of the layered sand condition

is shown in Fig. 5. PLAXIS 3D Foundation incorporates a fully automatic mesh-generation procedure to create the 3D FE mesh. The 3D mesh was generated in two stages. Firstly, a two-dimensional (2D) mesh consisting of six-noded triangular elements was automatically created. Then, the 2D mesh was refined around the pile. In the second stage, this 2D mesh was extended into a 3D mesh compounded of 15-noded wedge elements. The 15-noded wedge element is composed of 6-noded triangles in the horizontal direction and 8-noded quadrilaterals in the vertical direction. In this type of 3D elements, three nodes are located along each edge, which provide a quadratic approximation of the displacement field within the volume of the element [32].

The pile is modeled as a solid pile using volume elements in the centre of the mesh. To model the interaction between the sand and pile an interface was created along the entire circumference of the pile. The sand-pile interface is modeled by means of interface elements. Sixteen-noded interface elements with zero thickness were used to simulate the soil-pile interaction. The interface elements can be smooth or fully rough. The properties of the interface are defined by the interface-strength-reduction factor (R_{inter}). The value of the R_{inter} factor was defined for each of the soil conditions by calibrating the analyses results with respect to the tests results. In the analyses, the installation effects of the pile are not taken into account. An elastic-plastic model is used to define the behavior of the interface elements. The relationship between the normal pressure and the shear force is governed by the Coulomb criterion. The interface elements allow the development of slipping behavior between the sand and the pile.

It was assumed that the lateral load is acting at a height of 6 m above the sand surface as a lateral point load in prototype dimensions since this is the approximate height of most laterally loaded structures. In the analyses, the lateral load was imposed directly to the top level of the pulling arm as a point load. The pulling arm is also modeled as a solid pile using the volume elements.

All the nodes on the model's vertical boundaries, i.e., the nodes on the end of the x - y and y - z planes, were restrained in the x and z directions, respectively. All the nodes on the model bottom boundary were fixed in all three directions (x , y and z).

The pile and pulling arm were assumed to be linearly elastic. The Mohr-Coulomb (MC) material model was used to simulate the non-linear sand behavior because of its simplicity, reasonable number of model parameters and reasonable accuracy in modeling the behavior of the laterally loaded pile problem. The MC model has a fixed

yield surface and the yield surface is not affected by plastic straining. For MC-type yield functions, the theory of associated plasticity overestimates the dilatancy. Therefore, in addition to the yield function, a plastic potential function is introduced. The plastic potential function contains the parameter of dilatancy angle that is required to model positive plastic volumetric strain increments. The elastic-plastic MC model involves five basic input parameters: elasticity modulus (E), Poisson's ratio (ν), internal friction angle (ϕ'), cohesion (c') and dilatancy angle (ψ).

The friction angles of the sand were 38° and 44° , based on the drained triaxial compression test results for the loose and dense sand packings, respectively. Direct shear tests on the sand samples were also conducted to determine the angles of internal friction. Accordingly, ϕ' values of 39.27° and 45.67° were obtained at dry unit weights of 15.03 kN/m^3 and 17.06 kN/m^3 , corresponding to the loose and dense sand packings, respectively. The value of the secant elastic modulus (E_{50}) of the sand, in both loose and dense sand conditions, was obtained from the drained triaxial compression tests. The values of E_{50} were 20600 kPa and 30000 kPa for the loose and dense sand conditions, respectively. The dilatancy angle of the sand was evaluated according to the equations proposed by Bolton [33] and PLAXIS for quartz sand. The values of Poisson's ratio generally lay between 0.20 and 0.40 in the sand; therefore, an average value of 0.30 was used in the computations [34]. To avoid complications in the analyses performed in dry cohesionless soils ($c'=0$), PLAXIS offers to enter a small value that is bigger than 0.20 kPa for c' . For that reason, a value of 0.30 kPa was used for the c' in the analyses.

The initial stresses in the numerical modeling were generated using Jaky's formula, which gives the at rest earth pressure coefficient $K_0 = 1 - \sin\phi'$ [35]. In order to obtain load-displacement relationships at the pile head the total lateral load is applied in stages.

6 PARAMETRIC STUDIES

In this section, parametric studies were conducted, both in loose and dense sand conditions, to investigate the influences of the elasticity modulus of sand, the sand dilatancy and the interface strength on the response of a short rigid pile subjected to a lateral load using the non-linear finite-element approach. The effects of these parameters can not easily be evaluated experimentally in the model loading tests.

The model calibration was made by comparing the results of the FE analyses with those from model tests

to determine the optimum values of the parameters. Thus, numerical models, for both loose and dense sand conditions, which produce the most reliable results with respect to the test results, were obtained. The value of the applied lateral load in the parametric analyses carried out in homogeneous loose sand was 40 N, while it was 80 N in homogeneous dense sand.

The effect of the elasticity modulus of the sand on the lateral response of the model pile is considered herein by keeping the values of the sand dilatancy and interface strength constant and changing the values of the elasticity modulus. The same procedure was applied while investigating the effects of other two parameters, i.e., the sand dilatancy and the interface strength.

6.1 ELASTICITY MODULUS

The strength and stiffness of the sand are generally assumed as increasing with depth. The sands exhibit non-linear and irreversible deformation behavior under loading. The deformability or stiffness of the sand varies depending on the void ratio extent, which means the difference between the maximum and minimum void ratios. On the other hand, the elasticity modulus of sand increases with effective confining stress and the elasticity modulus is not proportional to the effective confining stress [36]. It is reasonable to assume that the elasticity modulus increasing linearly with depth for sands and acceptable solutions can be obtained in this way [26, 37].

In contrast, the modulus of elasticity of sand is constant in the horizontal direction [29]. In many cases encountered in practice, the elasticity modulus of sand would not increase linearly with depth.

In PLAXIS 3D Foundation, the value of the elasticity modulus is normally constant through the depth when using the MC material model to simulate the stress-strain behavior of sand. The reference elasticity modulus ($E_{reference}$) is the value of the elasticity modulus of sand determined at the level of the reference depth ($y_{reference}$). In the homogeneous loose and dense sand conditions, the $y_{reference}$ is equal to zero and $E_{reference}$ is determined at the level of the sand surface. However, the increment of elasticity modulus with depth can be considered using the $E_{increment}$ option. This option defines the amount of increment per unit of depth.

The influence of the elasticity modulus of sand on the lateral response of a short rigid pile subjected to lateral loading was investigated, assuming that the elasticity modulus was a function that is linearly dependent on the depth of the sand layer. The values of the constant parameters a (slope) and b (intercept) of the linear relationship $y = a + bx$ were derived as an example for the homogeneous loose sand condition. The value of the secant elasticity modulus (E_{50}) of loose sand defined considering the stress-strain curve obtained from drained triaxial compression test conducted under the confining pressure equal to 100 kPa was 20600 kPa. The dry unit weight of the loose sand was 15.03 kN/m³. An effective stress value

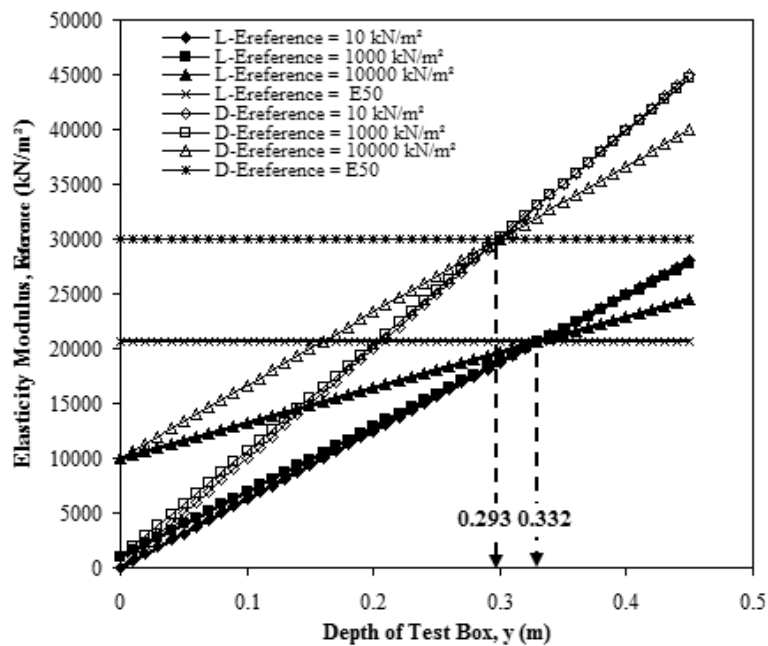


Figure 6. Elasticity modulus functions in the loose (L) and dense (D) sand conditions.

of 100 kPa can be obtained at a depth of 6.65 m below the sand surface in the homogeneous loose sand layer in the prototype conditions. However, this prototype depth corresponds to a depth of 33 cm in the model dimensions. If we assume that the value of elasticity modulus increases linearly with depth, the value of $E_{reference}$ determined at the level of the sand surface will increase as well as $E_{increment}$ per unit depth and it will be equal to E_{50} at the depth of 33 cm. The function defining the variation of the elasticity modulus with depth is described as follows:

$$E = E_{reference} + E_{increment} y \quad (3)$$

where y represents the depth in the sand layer.

Fig. 6 shows the elasticity modulus functions obtained in loose and dense sands for different values of $E_{reference}$. In order to study the effect of the elasticity modulus in loose and dense sand conditions, a series of analyses were carried out for four different values of $E_{reference}$ chosen at the beginning of the analyses. The results of the numerical analyses are summarized in Tables 2 and 3 for the loose and dense sand conditions, respectively. Figs. 7 and 8 illustrate the lateral load-lateral displacement relations observed at the pile head for the loose and dense conditions, respectively.

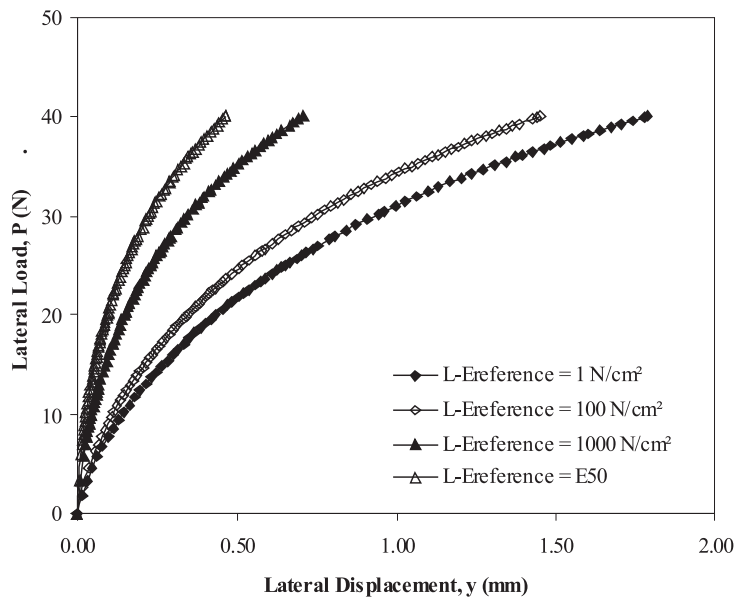


Figure 7. The effect of elasticity modulus of sand in the loose (*L*) sand condition.

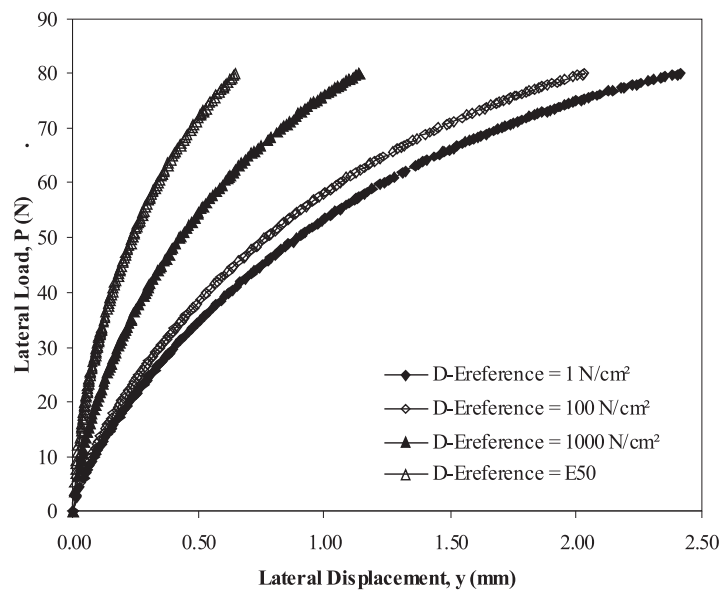


Figure 8. The effect of elasticity modulus of sand in the dense (*D*) sand condition.

Table 2. The effect of the elasticity modulus in loose sand.

$E_{reference}$ (N/cm ²)	1	100	1000	$E_{50} = 2060$
$E_{increment}$ (N/cm ² /cm)	62.400	59.400	32.121	0
ψ (°)	8	8	8	8
R_{inter}	0.700	0.700	0.700	0.700
P (N)	40	40	40	40
$u_{x=0}$ (cm)	0.178	0.145	0.070	0.046
R_D (%)	73	72	66	62
R (°)	0.695	0.572	0.301	0.210

Table 3. The effect of the elasticity modulus in dense sand.

$E_{reference}$ (N/cm ²)	1	100	1000	$E_{50} = 3000$
$E_{increment}$ (N/cm ² /cm)	102	98.970	68.250	0
ψ (°)	14	14	14	14
R_{inter}	0.700	0.700	0.700	0.700
P (N)	80	80	80	80
$u_{x=0}$ (cm)	0.241	0.203	0.113	0.064
R_D (%)	70	69	64	59
R (°)	0.987	0.838	0.498	0.309

Similar behaviors were observed against the variation of the value of $E_{reference}$ in both loose and dense sand conditions.

As seen in Tables 2 and 3, as expected, the lateral displacements observed at the pile head decrease with an increasing value of $E_{reference}$. In addition, the depths of the rotation point move towards the sand surface. The value of the lateral displacement at the pile head in the case of $E_{reference}=E_{50}$ is approximately 74% smaller than that obtained in the case of $E_{reference}=1$ N/cm². However, the lateral load capacity in the case of $E_{reference}=1$ N/cm² is nearly 48% smaller than that of the case of $E_{reference}=E_{50}$ for the same lateral displacement in both loose and dense sand conditions. As shown in Figs. 7 and 8, the relations are non-linear for both loose and dense sand conditions. As seen in Figs. 7 and 8, the load-displacement behaviors are stiffer and provide a higher lateral load capacity with the increasing value of $E_{reference}$ for the same lateral displacement value in both loose and dense sand conditions.

In layered sand conditions, the depth to obtain an effective stress value equal to 100 kPa, considering the layer structure, was calculated using a similar procedure as in the homogeneous sand conditions. Then, the values of the $E_{reference}$ and $E_{increment}$ at the beginning of the dense sand layer were defined using the values of $E_{reference}$ and $E_{increment}$ chosen for the upper loose sand layer with respect to the results of the parametric analyses.

6.2 SAND DILATANCY

The internal friction angle (ϕ') is the principal parameter when predicting the behavior of laterally loaded piles embedded in sand using theoretical methods. However, these methods [12, 13, 14, 15] ignore the effect of the volume change characteristics of sands based on the dilatancy of the pile's response. However, the effect of the dilatancy of the sands on the lateral response of piles subjected to lateral loading cannot also be investigated experimentally by model test studies. Therefore, the role that sand dilatancy plays in the lateral load capacity of the pile remains unknown [1].

In order to investigate the effect of dilatancy on the behavior of laterally loaded short rigid piles founded in sand a series of non-linear FE analyses were carried out. In the analyses, two different approaches suggested by Bolton [33] and PLAXIS associated with the value of critical internal friction angle ($\phi'_{critical}$) of quartz sand were used to calculate the dilatancy angle of the sand. The values of the dilatancy angle were obtained using the following formula:

$$\phi' = \phi'_{critical} + \psi \quad (4)$$

The value of $\phi'_{critical}$ for quartz sand has been proposed as 33° by Bolton [33], while PLAXIS suggests this value

Table 4. The effect of the dilatancy angle in loose sand.

$E_{reference}$ (N/cm ²)	1	1
$E_{increment}$ (N/cm ² /cm)	62.400	62.400
ψ (°)	5	8
R_{inter}	0.700	0.700
P (N)	40	40
$u_{x=0}$ (cm)	0.207	0.178
R_D (%)	73	73
R (°)	0.807	0.695

Table 5. The effect of the dilatancy angle in dense sand.

$E_{reference}$ (N/cm ²)	1	1
$E_{increment}$ (N/cm ² /cm)	102	102
ψ (°)	11	14
R_{inter}	0.700	0.700
P (N)	80	80
$u_{x=0}$ (cm)	0.284	0.241
R_D (%)	70	70
R (°)	1.168	0.987

should be 30°. The internal friction angles were 38° and 44° for the loose and dense sand conditions, respectively, in the analyses. The analyses were conducted in both loose and dense sand conditions. The results of the analyses are presented in Tables 4 and 5 for the loose and dense sand conditions, respectively. The plots of the lateral load-lateral displacement relations at the pile head for different dilatancy angles are shown in Figs. 9 and 10 for the loose and dense sand conditions, respectively.

As seen in Tables 4 and 5, for both loose and dense sand conditions, the lateral displacement observed at the pile head decreases by nearly 15% with the increasing value of dilatancy angle. However, the depth of the rotation point is not affected by the variation of the dilatancy angle. Thus, it can be concluded that the volume of the

sand mass mobilized under the lateral load will be more in the case of higher dilatation values. As a result, the higher dilatation values will provide greater lateral load capacities.

As shown in Figs. 9 and 10, for both loose and dense sand conditions, the effect of sand dilatancy on the lateral load capacity is seen more clearly with an increasing lateral displacement at the pile head. At first, especially for the small values of the lateral displacement, the effect of dilatancy is not distinct and the curves obtained for different dilatancy angles are overlapped. The sand mass compressed under the lateral loading becomes denser as the lateral displacement increases. As a result, the effect of the dilatancy property in sands arises as an extra contribution to their strengths.

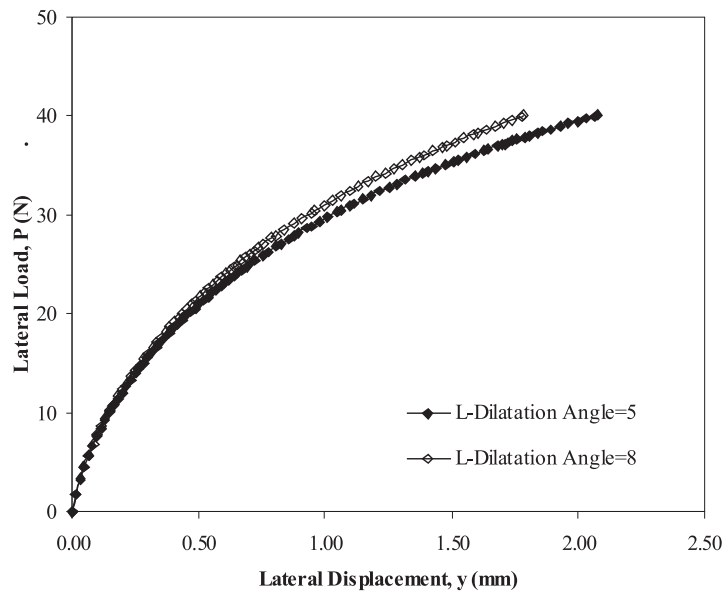


Figure 9. The effect of sand dilatancy in the loose (L) sand condition.

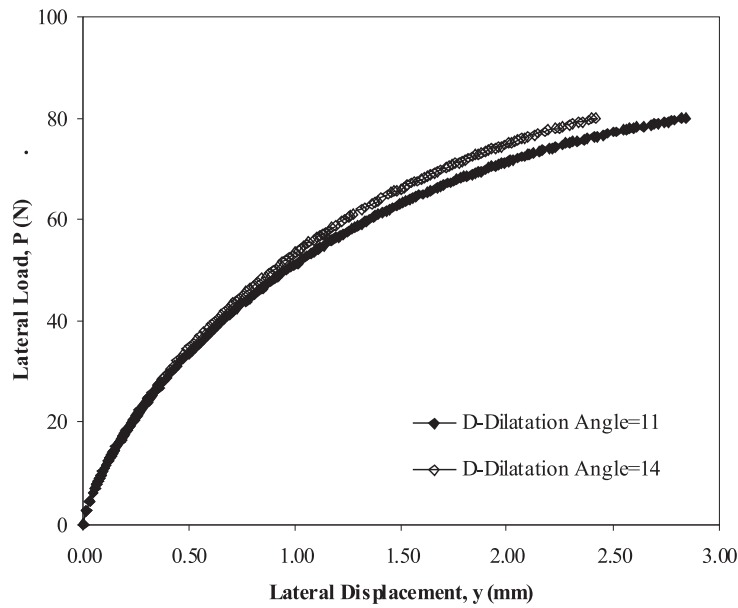


Figure 10. The effect of sand dilatancy in the dense (*D*) sand condition.

6.3 INTERFACE BEHAVIOR

The soil-structure interaction has a significant effect on the performance of buried structures. The correct modeling of the load-transfer characteristics of the soil-structure interface is very important in predicting the behavior of buried structures using numerical methods [38].

The main parameter represented the interface behavior is the strength-reduction factor (R_{inter}). The side friction between the pile and the soil is modeled by choosing a suitable value for R_{inter} . R_{inter} relates the interface strength to the soil strength. The interface properties are calculated from the soil properties in the associated data set and R_{inter} by applying the following rules;

$$c_i = R_{inter} c_{soil} \quad (5)$$

$$\tan\phi_i = R_{inter} \tan\phi_{soil} \leq \phi \tan\phi_{soil} \quad (6)$$

$$\psi_i = 0^\circ \text{ for } R_{inter} < 1, \text{ otherwise } \psi_i = \psi_{soil} \quad (7)$$

In general, for a real soil-structure interaction, the interface is weaker and more flexible than the associated soil layer, which means that the value of R_{inter} should be less than 1. PLAXIS, generally, assumes that the interface properties are equal to two-thirds of the soil properties (i.e. $R_{inter}=0.67$).

Some factors, such as the installation method of the pile, the relative density of the sand, the roughness

of the pile surface and pile material, would affect the behavior of the interface element. Therefore, the value of R_{inter} should be decided after considering these factors. On the other hand, the installation method of the pile cannot be taken into account in PLAXIS. In addition, the model pile used in the model test studies was a buried pile and the surface of the pile was smooth in all the tests. Further, when the grain size of the sand used in the model tests was considered, the value of 0.67 for R_{inter} may be unrealistic when analyzing the model tests. Hence, the value of R_{inter} was determined by a trial-and-error approach in the analyses performed in both loose and dense conditions by comparing the load-displacement relations obtained from numerical analyses and model tests.

The interface elements can transmit only shear forces along their surfaces when they are subjected to a compressive normal pressure. When the shear stress reaches the bond strength, governed by the Coulomb criterion, a large relative displacement (slip) occurs [38]. The distinction between the elastic behavior, where small displacements can occur within the interface, and plastic interface behavior, when permanent slip may occur, is made using the Coulomb criterion. For the elastic behavior of the interface, the shear stress τ is given by:

$$|\tau| < \sigma_n \tan\phi_i + c_i \quad (8)$$

$$|\tau| = \sqrt{\tau_{s1}^2 + \tau_{s2}^2} \quad (9)$$

where:

- τ_{s1} and τ_{s2} ; shear stresses in the two (perpendicular) shear directions,
- σ_n ; effective normal stress.

For plastic behavior τ is evaluated using the following formula:

$$|\tau| = \sigma_n \tan \phi_i + c_i \quad (10)$$

where:

- ϕ_i and c_i ; the friction angle and cohesion of the interface, respectively.

The numerical results are summarized in Table 6 and Table 7 for the loose and dense sand conditions, respectively. The results of the analyses are also presented in terms of lateral load-displacement relationships at the

pile head in graphical form in Figs. 11 and 12 for the loose and dense sand conditions, respectively.

Similar behaviors were obtained in both loose and dense sand conditions. As seen in Tables 6 and 7, the lateral displacement at the pile head decreases with the increasing value of the R_{inter} . However, the depth of the rotation point moves towards the sand surface as the value of R_{inter} increases.

As shown in Figs. 11 and 12, R_{inter} has a significant effect on the lateral load capacity of the short rigid pile for both loose and dense sand conditions. Such that, the lateral load capacity of the short rigid pile in loose sand in the case of $R_{inter}=0.03$ is equal to 16% of the lateral load capacity obtained in the case of $R_{inter}=0.70$ for the same lateral displacement. Similarly, in the dense sand condition, the lateral load capacity value obtained in

Table 6. The effect of the interface behaviour in loose sand.

$E_{reference}$ (N/cm ²)	1	1	1
$E_{increment}$ (N/cm ² /cm)	62.400	62.400	62.400
ψ (°)	5	5	5
R_{inter}	0.030	0.350	0.700
P (N)	40	40	40
$u_{x=0}$ (cm)	5.425	0.292	0.207
R_D (%)	90	75	73
R (°)	16.690	3.285	0.807

Table 7. The effect of the interface behaviour in dense sand.

$E_{reference}$ (N/cm ²)	1	1	1
$E_{increment}$ (N/cm ² /cm)	102	102	102
ψ (°)	11	11	11
R_{inter}	0.130	0.350	0.700
P (N)	80	80	80
$u_{x=0}$ (cm)	0.585	0.417	0.284
R_D (%)	81	73	69
R (°)	2.054	1.634	1.168

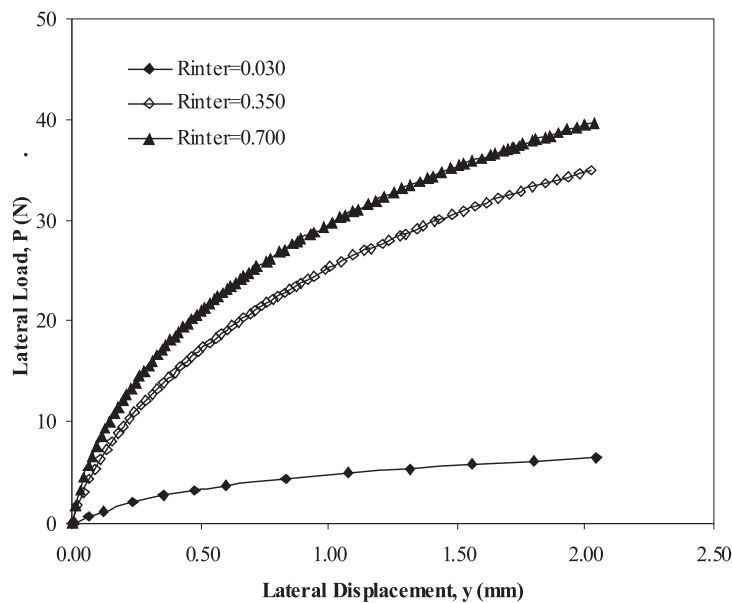


Figure 11. The effect of the interface behavior in the loose (L) sand condition.

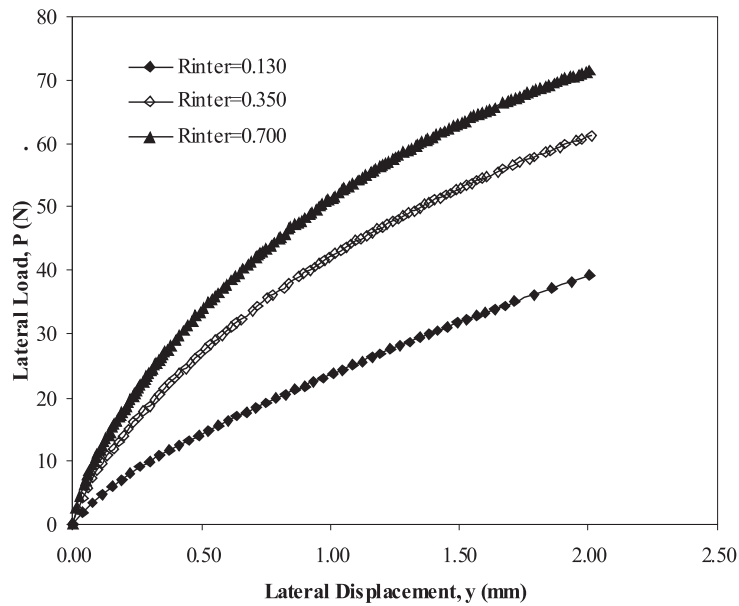


Figure 12. The effect of the interface behavior in the dense (D) sand condition.

the case of $R_{inter}=0.13$ is as well as the 54% of the value obtained in the case of $R_{inter}=0.70$ for the same lateral displacement. The load-displacement curves exhibit stiffer behavior depending on the increasing value of R_{inter} .

Fig. 13 indicates the effect of R_{inter} on the interaction between the sand and the pile. As shown in Fig. 13, the degree of permanent slipping behavior between the pile and the sand surfaces decreases depending on the decreasing value of R_{inter} . As a result, the frictional behavior between the surfaces decreases. Since the interface elements can not

transfer shear forces across their surfaces completely when they are subjected to a compressive normal pressure, the lateral load capacity of the pile will decrease.

On the other hand, the values of $\tan\phi_i$ and c_i are calculated by multiplying the R_{inter} value with the soil properties, as shown in eqs. 5 and 6. Therefore, even if the normal soil resistance in front of the pile is unchanged, the slipping behavior along the interface will occur at different shear strength values, depending on the chosen R_{inter} value and the criteria used in modeling the interface behavior.

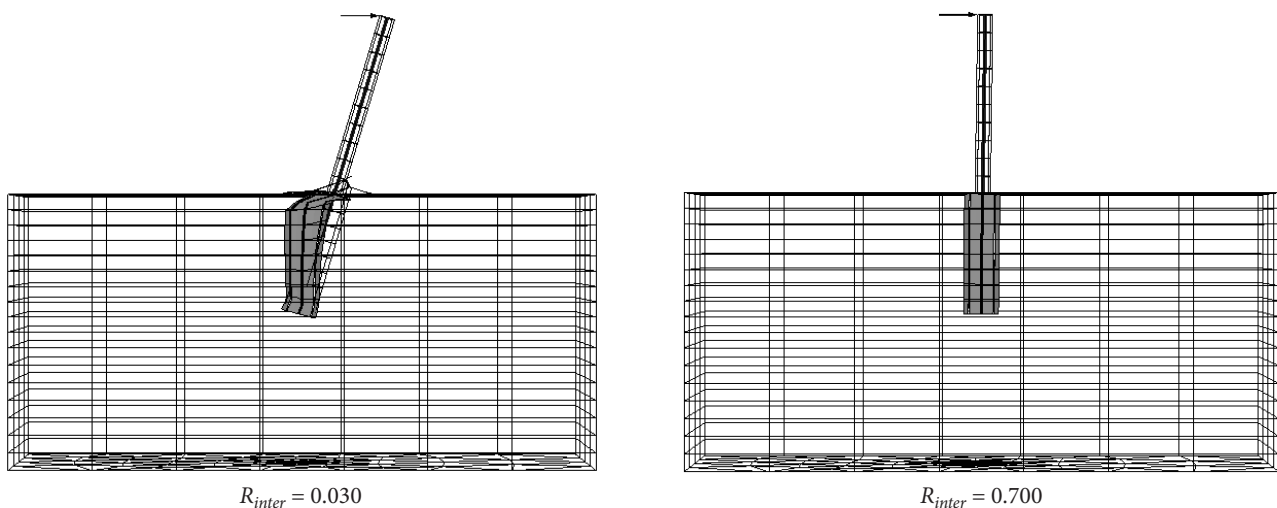


Figure 13. The effect of the R_{inter} on the interaction between the sand and the pile.

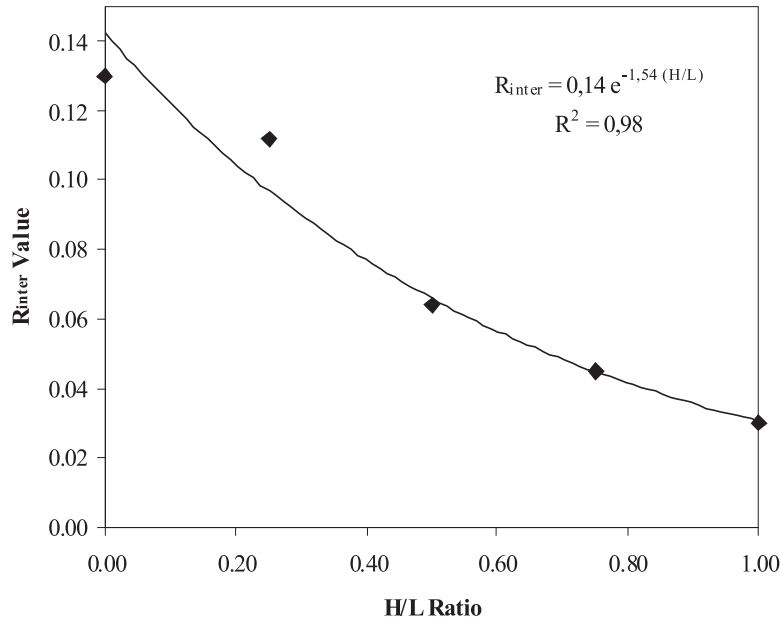


Figure 14. The variation of the R_{inter} with the H/L ratio.

The interface behavior is significantly dependent on the sand’s density. Therefore, it is not reliable to use the values of R_{inter} obtained for the homogeneous loose and dense sand in the layered sand conditions having different layer thicknesses. It is necessary to define the average value of R_{inter} that is valid through the layered sand profile for each of the layered structure. A series of analyses were performed in the layered sand conditions in order to define the R_{inter} values that belong to each layer of the structure. The lateral load-displacement curves obtained from numerical analyses were compared with the curves obtained from model tests to calibrate the values of R_{inter} . The relationship obtained between R_{inter} and H/L is shown in Fig.14. The relation between R_{inter} and H/L was fitted with the following equation:

$$R_{inter} = 0.14 e^{-1.54 (H/L)} \quad (11)$$

The R^2 value of the equation was obtained as 98%. Equation 11 has been obtained as an approximation of the results of the experimental studies and numerical analyses. This equation can only be used in the conditions valid in the model tests performed. This equation is not applicable for different soil conditions.

7 RESULTS AND DISCUSSION

At the end of the parametric studies, the values of the parameters that produced the most reliable results with respect to the model test results were obtained. The

Table 8. The selected values of parameters obtained from the finite-element analyses.

		$HD=H/L=0$	$H/L = 0.25$	$H/L = 0.50$	$H/L = 0.75$	$HL=H/L=1$
$E_{reference}$ (N/cm ²)	Loose	1	1	1	1	1
	Dense		313	625	937	
$E_{increment}$ (N/cm ² /cm)	Loose		62.40	62.40	62.40	
	Dense	102	108	118.75	129	62.400
$\gamma_{reference}$ (cm)	Loose	0	0	0	0	0
	Dense		-5	-10	-15	
ψ (°)	Loose		5	5	5	
	Dense	11	11	11	11	5
R_{inter}		0.130	0.112	0.064	0.045	0.030

* HD means the homogeneous dense sand¹

** HL means the homogeneous loose sand²

values of the parameters chosen at the end of the parametric analyses are listed in Table 8.

After the determination of the values of the parameters, finite-element models were analyzed under lateral loads

equal to the ultimate lateral load capacities obtained in the model tests for each of the soil conditions. Thus, as the distribution of the lateral effective stresses along the pile embedded depth, the failure regions occurred around the model pile and the deformation behavior of

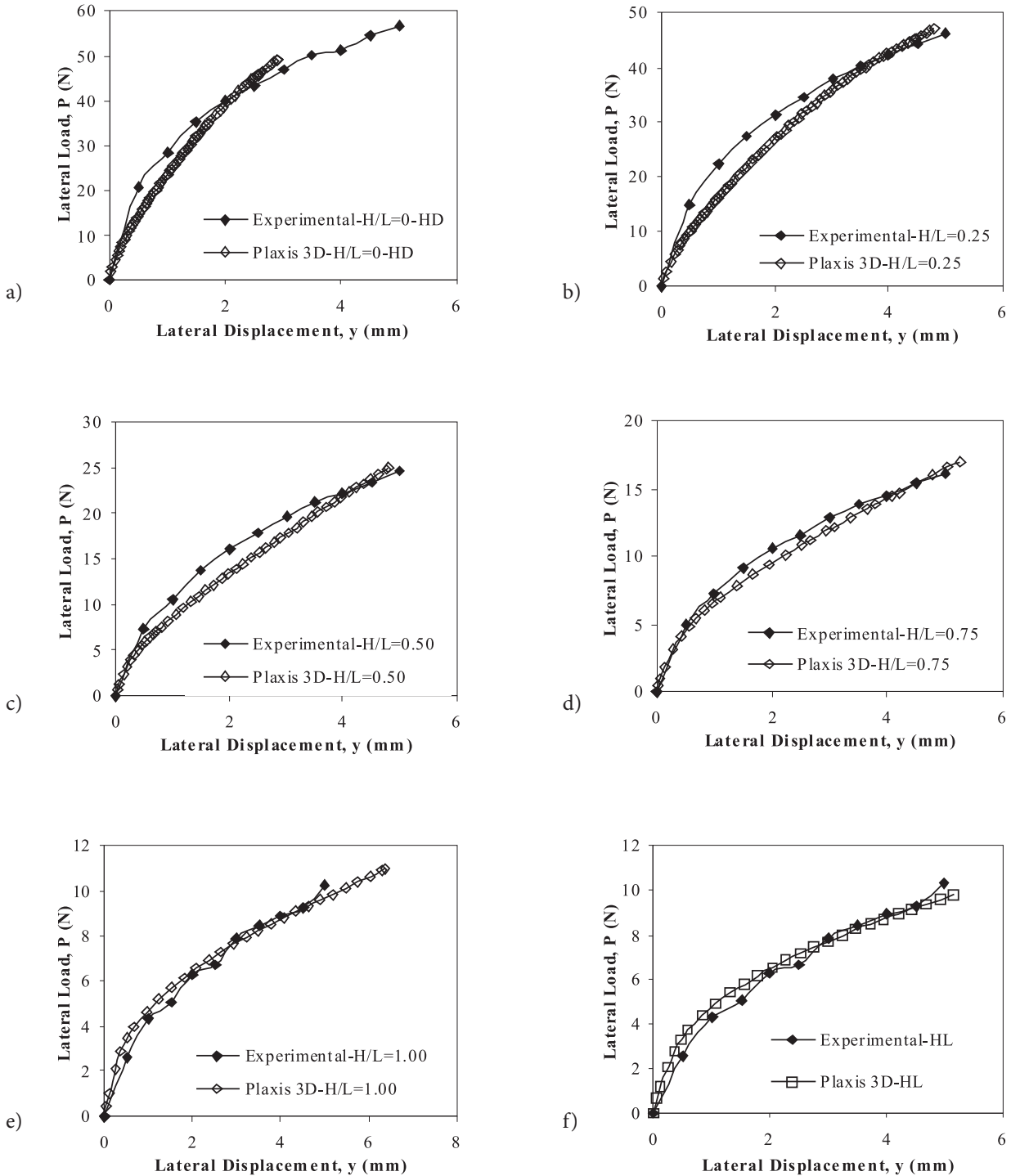


Figure 15. The lateral load-displacement relations at the pile head.

the system could be considered under the experimental conditions.

The lateral load-displacement relations at the pile head obtained from the experimental model studies and numeri-

cal analyses are compared in Fig. 15 for the cases of $H/L=0$ (Homogeneous dense sand condition), 0.25, 0.50, 0.75, 1.00 and the homogeneous loose sand condition, respectively. Since the tip resistance of the pile was neglected in the calculations, the homogeneous loose sand condition may

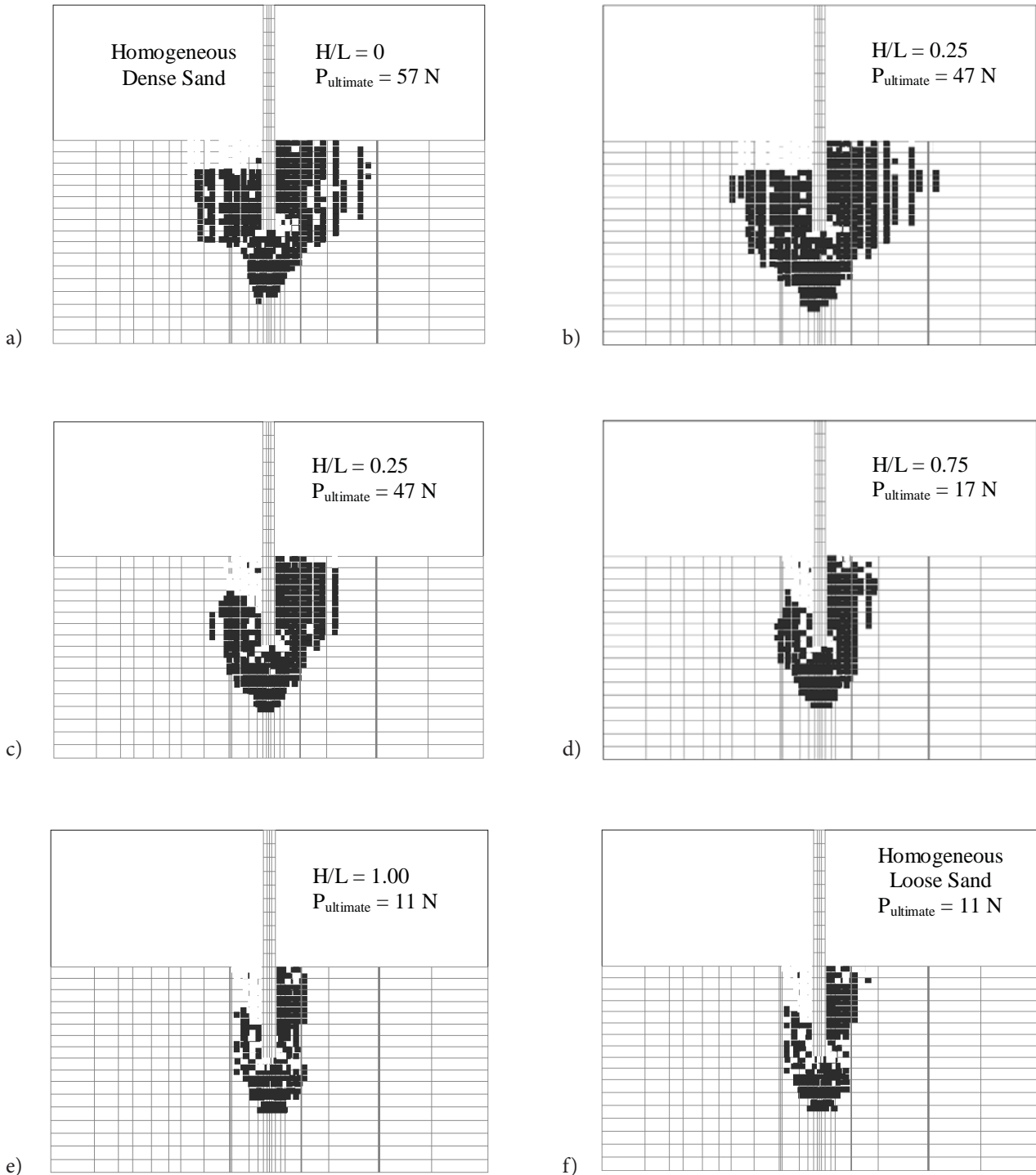


Figure 16. The failure regions developed around the pile.

be assumed as $H/L=1$. The results obtained from numerical analyses performed in the homogeneous loose sand and in the case of $H/L=1$ also confirm this assumption.

As seen in Fig. 15, in general, a very good agreement between the curves, especially for the cases of $H/L=0.75$, $H/L=1.00$ and homogeneous loose sand condition, was observed. The relationships between the lateral load and lateral displacement obtained from both experimental and numerical studies are non-linear in all the cases considered. As shown in Fig. 15 (a), in the analysis performed in the homogeneous dense sand condition, failure occurred at any loading step during the analysis and no peak lateral resistance was observed. This might be due to an associated flow rule when a strain hardening soil response was used. A more realistic analysis could be performed using a non-associated flow rule with strain softening and the reduction from peak to critical state friction angles could be taken into account as a function of plastic strains. It is clear that the void ratio extent of the soil will be smaller and the soil will be more compact and dense when the value of H/L decreases. If the lateral loads corresponding to the same lateral displacement in each of the soil conditions are compared, it can be concluded that the range in which the soil behaves elastically will be greater with decreasing thickness of the upper loose sand layer.

In the case of a short rigid pile the failure occurs as the lateral earth pressures reach the ultimate passive lateral resistance of the soil along the pile length. The pile rotates around a point somewhere along its length and causes the development of a passive resistance in the soil in front of the pile above the rotation point and the back side of the pile below the rotation point. Once the mobilizing passive resistance is equal to the limit state of the passive earth pressure, failure takes place and then a further displacement of the pile does not significantly effect the passive pressure. This phenomenon is well simulated by the non-linear 3D FE analyses.

The calculated failure regions when the pile head reaches the lateral displacement of 5 mm under the lateral load are depicted in Fig. 16. The failure regions are composed of plastic stress (shear yielding) points. Plastic stress point can be either a mohr-coulomb point or a tension cut-off point. The Mohr-Coulomb points shown in

the figure with a black color represent the mobilizing passive resistance in the sand. On the other hand, the white regions consist of tension cut-off points represent the mobilizing active pressure. As expected, the mohr-coulomb points develop not only in the sand in front of the pile above the rotation point but also at the back side and bottom. Similarly, the tension cut-off points develop not only in sand at the back side of the pile above the rotation point near the sand surface but also in front of the pile below the rotation point near the pile tip.

Although the failure zone that occurred in the case of $H/L=0.25$ is a little greater than the failure zone in the case of $H/L=0$, the ultimate lateral load capacity of the pile in the case of $H/L=0.25$ is nearly 19% smaller than that obtained in the case of $H/L=0$. The rotation points in the cases of $H/L=0$ and $H/L=0.25$ are almost at the same depths. Therefore, the passive resistances developed below the rotation point will be equal for these two cases. The difference between the ultimate lateral load capacities is due to the upper loose sand layer in the case of $H/L=0.25$. This is because the shallow zone close to the sand surface could not provide a contribution to the lateral resistance as well as in the case of $H/L=0$.

As seen in Fig. 16, the boundaries of the failure regions extend to greater depths and greater lateral distances with the decreasing thickness of the upper loose sand layer. However, the lateral load capacity of the pile in the layered sand condition is significantly affected by the length of the pile within the dense sand layer. In the case of $H/L=0$, the failure zone propagates to a lateral distance approximately five times that of the pile diameter from the front of the pile, while these distances are approximately 4D and 3D from the back side and the bottom, respectively. The distances of the failure regions from the in front, rear and tip of the pile for each of the soil conditions are summarized in Table 9. It is apparent from Fig. 16 that the relative density has a major effect on the lateral load capacity of short rigid piles.

In order to predict the ultimate lateral load capacity ($P_{ultimate}$) of short rigid piles it is necessary to know the distribution of the lateral effective stresses mobilized along the pile embedded length. Thus, the unknown value of $P_{ultimate}$ can be determined from the equilibrium

Table 9. The distances of the failure regions from the in front, rear and tip of the pile.

	$HD = H/L=0$	$H/L = 0.25$	$H/L = 0.50$	$H/L = 0.75$	$H/L = 1.00$	$HL=H/L=1$
Front	4D ~ 5D	4D ~ 5D	3D	2D	D	D
Rear	4D	4D	2D	D	D	D
Tip	3D	3D	3D	2D	2D	2D

condition of the horizontal forces acting on the pile and the moments calculated according to a point defined. The lateral effective stress (σ'_h) is an important factor affecting significantly the $P_{ultimate}$ values [39].

Brinch Hansen [12] presented a method to predict the lateral load capacity of short rigid piles in a general $c-\phi$ soil, where c and ϕ' are the cohesion and the effective internal friction angle of the soil, respectively. Brinch Hansen [12] proposed an empirical formula from which the depth of the rotation point is determined by means of trial and error. The passive lateral earth pressure areas developed above and below the rotation point yield equal moments at the point where the lateral load is applied. The difference between the two pressure areas gives the lateral load capacity of a short rigid pile subjected to a lateral load. The ultimate lateral resistance of cohesionless soil, $P_{ultimate}$, per unit length of the pile at a depth of z is calculated using the following equation:

$$P_{ultimate} = p_z K_{qz} D \quad (12)$$

where:

- p_z ; effective overburden pressure at a depth of z ,
- K_{qz} ; earth pressure coefficient which is a function of the pile diameter and friction angle,
- D ; diameter of the pile.

Meyerhof et al. [14] proposed a method to estimate the lateral load capacity of short rigid piles founded in two-layered soil deposits. This method calculates the

ultimate lateral load capacity of the pile assuming that the variation of lateral effective stresses with depth is linear. The three-dimensional characteristic of the lateral soil resistance is taken into account using shape factors. In this method, the depth to the pile rotation point is determined by solving the equations obtained from the equilibrium condition of the resultant horizontal forces and moments. Meyerhof et al. [14] suggested the following relationship to define the lateral load capacity of short rigid piles in layered sand.

$$Q_U = D (\gamma L^2 K_b F_b r_b s_b) \quad (13)$$

where:

- D : pile diameter,
- γ : average value of the unit weights of the sand layers,
- L : embedded length of the pile,
- K_b : net earth pressure coefficient defined as $K_b = [\tan^2(45+\phi/2) - \tan^2(45-\phi/2)]$,
- F_b : lateral resistance factor defined corresponding to the ratio of K_{b1} / K_{b2} ,
- r_b : moment reduction factor defined as $r_b = 1 / (1 + 1.4e / D)$,
- s_b : shape factor which is dependent on H/L , ϕ' and L/D ,
- e : load eccentricity.

The value of the lateral effective stress at a depth of z is calculated using the following equation:

$$\sigma'_h = \gamma z K_b s_b \quad (14)$$

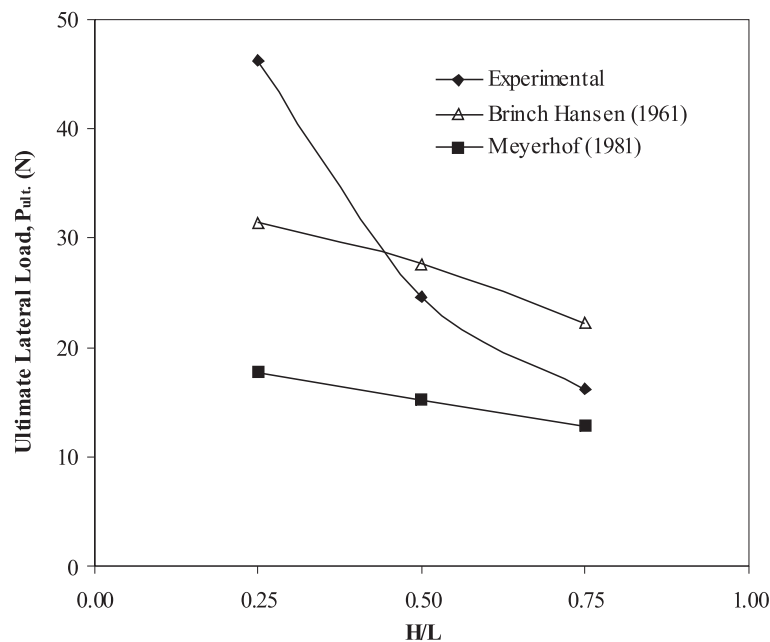


Figure 17. The comparison of the lateral load capacities with respect to H/L .

The ultimate lateral load capacities obtained for the cases of $H/L=0.25$, 0.50 and 0.75 from the method suggested by Brinch Hansen [12] and Meyerhof et al. [14] and model test studies are compared in Fig. 17. Also, the distributions of the lateral effective stresses along the pile embedded depth obtained from the methods proposed by Brinch Hansen [12] and Meyerhof et al. [14] and 3D non-linear FE analyses for the case of $H/L=0.25$ are shown in Fig. 18. Since the 3D FE analysis was carried out under the experimental lateral load level, the lateral effective stresses developed under the experimental loading level have been obtained.

As shown in Fig. 17, the lateral load capacities obtained from both methods proposed by Brinch Hansen [12] and Meyerhof et al. [14] and model test studies decrease with the increasing value of the H/L ratio. The reduction in the values of the ultimate lateral load capacities with respect to the H/L ratio is non-linear for the experimental results, while it is approximately linear for the values obtained from the methods suggested by Brinch Hansen [12] and Meyerhof et al. [14]. The difference between the two ultimate lateral load capacity ($P_{ultimate}$) values obtained from Brinch Hansen's method and the experimental study for the case of $H/L=0.25$ is approximately as well as the 30% of the experimental capacity, while this ratio is equal to 60% of the experimental capacity for the Meyerhof et al.'s method. Brinch Hansen's [12] method overestimates the $P_{ultimate}$ values with respect to the experimental results for the cases of $H/L=0.50$ and $H/L=0.75$. The $P_{ultimate}$ values differ as the ratio of 10% and 40% of the $P_{ultimate}$ values observed in the

experimental studies for the $H/L=0.50$ and $H/L=0.75$, respectively. The method suggested by Meyerhof et al. [14] underestimates the $P_{ultimate}$ values with respect to the experimental values in all of the combinations of the layered sand profile considered. The differences between two $P_{ultimate}$ values are the 37% and 20% of the experimental $P_{ultimate}$ value for the cases of $H/L=0.50$ and $H/L=0.75$, respectively. The ultimate lateral load capacities, in all three cases (i.e., $H/L=0.25$, $H/L=0.50$ and $H/L=0.75$), calculated using the Brinch Hansen's [12] method are approximately equal to 1.75 times the load-capacity values predicted from the method proposed by Meyerhof et al. [14].

Fig. 18 shows the distribution of the lateral effective stresses along the pile embedded length for the case of $H/L=0.25$. The distributions of the lateral effective stresses predicted from the methods proposed by Brinch Hansen [12] and Meyerhof et al. [14] are linear through the upper and lower sand layers. In these methods the maximum lateral effective stresses occur at the depth of rotation point in front of the pile. The depths of the rotation points were calculated as the depths equal to 77% and 67% of the embedded pile length for the methods of Brinch Hansen [12] and Meyerhof et al. [14], respectively. In the FE analysis, the value of the lateral effective stress is zero at the depth of the rotation point and has a maximum value at an average depth corresponding to 50% of the embedded pile length below the sand surface. On the back side of the pile below the rotation point, maximum pressure is developed at the vicinity of the pile tip. This result is in line with the conventional methods used in comparison.

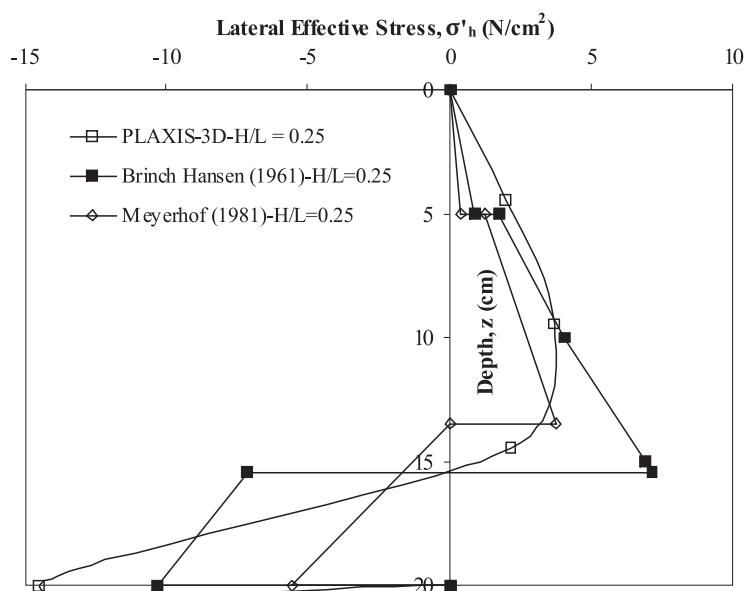


Figure 18. The distributions of the lateral effective stresses along the pile length.

The distribution of the lateral effective stresses computed by PLAXIS is non-linear through the layered sand profile. The rotation point is located at an average depth corresponding to 86% of the embedded pile length.

The discrepancies between the results of the conventional methods and among the conventional methods and model test studies and among the conventional methods and non-linear FE analysis could be attributed to the three-dimensional effect of the laterally loaded pile problem and selected distribution form in the conventional method for the lateral effective stresses. The conventional methods used in comparison adopt different expressions of lateral soil resistance with a differently assumed distribution of lateral soil pressure with depth. Conventional methods assume that the distribution of lateral effective stresses with depth is linear. On the other hand, in both homogeneous and layered sand conditions, the variation of the lateral effective stresses with depth would be non-linear. The value of the ultimate lateral load capacity could be significantly different, depending on the methods used. The three-dimensional effect of the problem is taken into account using a shape factor in the conventional method. However, in the FE method, 3D stress state can be taken into account and the problem can be considered as a whole in 3D space.

The base shear resistance, Q_b , for sand can be calculated using the equation given below [40].

$$Q_b = \frac{\pi}{4} D^2 \sigma_b \tan \delta_b \quad (15)$$

where:

σ_b is the overburden pressure at the pile tip,
 δ_b is the friction angle at the interface of the pile tip and soil (in this study, δ_b has been calculated as $\tan \delta_b = R_{inter} \tan \phi_{soil}$).

In the layered sand conditions, the parameters of eq. 15 such as the D and δ_b are the same for all cases since the model pile with 50 mm diameter was used in all of the analyses. The pile tip was located on the dense sand in all the cases considered. Therefore, eq.15 returns to the following form.

$$Q_b = 2.464 \sigma_b \quad (16)$$

Almost the same average values were calculated for the overburden pressure as equal to 0.33, 0.32 and 0.31 N/cm² for the cases of $H/L=0.25$, 0.50 and 0.75, respectively. The base resistance calculated at the pile tip in the case of $H/L=0.25$ is equal to 1.72% of the ultimate lateral load capacity. This ratio has been obtained as 3.14% and 4.47% for the cases of $H/L=0.50$ and 0.75, respectively.

For short rigid piles, the base shear resistance can be significant provided that an adequate horizontal movement occurs at the pile tip. The lateral displacements observed at the pile tip were equal to 1.45% of the pile diameter for the case of $H/L=0.25$ and 0.60% and 0.33% for the cases of $H/L=0.50$ and 0.75, respectively. In layered sand conditions, the depth of the rotation point moves toward the pile tip with the increasing thickness of the loose sand layer. As a result, the lateral displacement at the pile tip and therefore the contribution of the base resistance decreases. The calculated mobilized shear strength values when the pile head reaches the lateral displacement of 5 mm under lateral load in the case of $H/L=0.25$ are illustrated in Fig. 19. On the other hand, the vertical load and interface behavior and also the factors affecting the base resistance contribution. There is no vertical load applied to the pile except the self-weight of the model pile and pulling arm. Since the horizontal movement of the pile tip is insufficient for the fully mobilized base resistance it was ignored in the calculations. The tip resistance of the pile was assumed to have a small contribution to the overall lateral load capacity.

O' Neill pointed out that in large-drilled shafts, the push-pull resistance provided by the vertical side shear resistance occurred due to the rotation of the pile can resist partially the moment at the pile head. The effect of the push-pull resistance can be significant especially in rocks [41]. Yang [40] proposed a method based on parametric study results to estimate the push-pull resistance of short drilled shafts. In the proposed method, the dominant factor affecting the push-pull moment resistance is the coefficient of friction of the shaft-sand interface and the push-pull moment resistance increases linearly with the coefficient of friction of the interface. In the present study, the embedded model pile was used. The surface of the pile was smooth. The model soil was dry, uniform and poorly graded sand. Depending on these factors the values of the coefficient of friction of the pile-sand interface used in the analyses of the model tests obtained were too small considering the values of the interface friction coefficient used in the analyses of in-situ conditions. Both in the experimental studies and numerical analyses, it was observed that the depth of the rotation point in layered sand conditions moves toward the pile tip with increasing depth of the loose sand layer. As a result, the push-pull resistance of the pile will reduce because of the decreasing length of the push zone and coefficient of friction between the pile and sand. The push-pull moment values calculated using the method proposed by Yang [40] in loose and dense sand conditions were assumed as having small contributions to resist the moment at the pile head and therefore it was neglected evaluating the results.

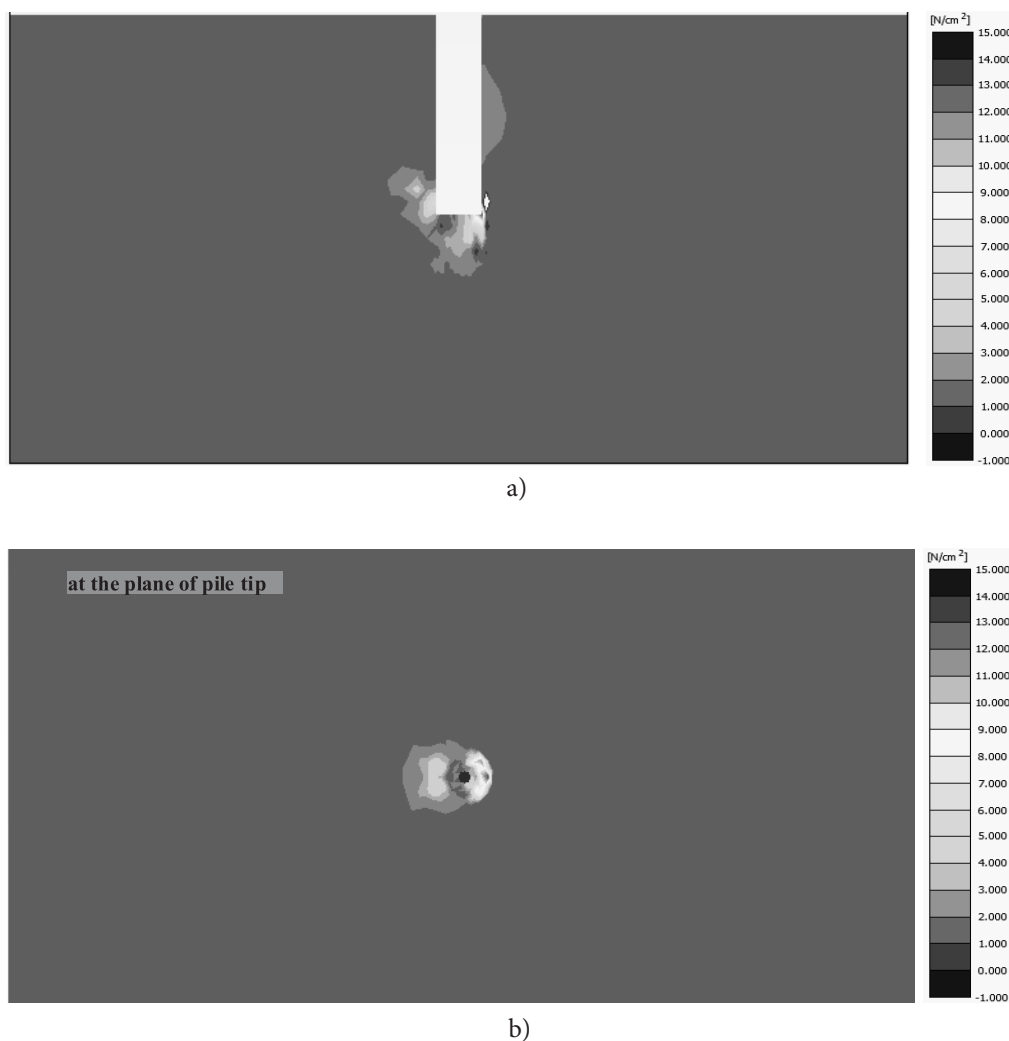


Figure 19. The distributions of the mobilized shear strengths at the ultimate condition in the case of $H/L=0.25$: a) along the pile embedment length, b) across the base of the pile.

8 LIMITATIONS

Full-scale loading test results are valid especially for in-situ conditions and for soil properties in which the test was performed. However, a full-scale loading test is not economic due to the expensive cost in time and money required for construction, instrumentation and testing. Therefore, small-scale model test studies are used widely as an alternative to full-scale loading tests. It is well recognized that small-scale model test studies carried out in cohesionless soils involve a scale-error [7, 31, 42].

In the present study, the model tests were conducted on 1/20-scale model piles, while the used sand particles were the same dimensions as in the prototype.

There are several recommendations related to the scale effect in the literature. Franke and Mutt [43] suggested that the scale-error can be neglected when the ratio of the pile diameter to the mean grain size is greater than 30. On the other hand, Ovesen [44] proposed that the ratio of the pile circumference to grain size should be in excess of 15-30 to avoid the scale effects. In the present study, the relationships between the dimensions of the model pile diameter and sand particle size satisfy the two recommendations mentioned above.

Despite all of these, this study should be evaluated a useful basis for further research and the results of this study should be supported with full-scale loading tests or centrifugal model test studies.

9 CONCLUSIONS

The behavior of short rigid piles subjected to a lateral load in two-layer sand deposits of different densities and thicknesses was investigated through model test studies and three-dimensional non-linear FE analyses. However, a parametric study was also performed to investigate the effects of the elasticity modulus of sand, sand dilatancy and interface behavior on the lateral load capacity of short rigid piles. Additionally, the lateral load capacities and the distribution of the lateral effective stresses were calculated using the methods proposed by Brinch Hansen [12] and Meyerhof et al. [14]. The results obtained from model test studies, numerical analyses and conventional methods were compared with each other. Based on the investigations the following main conclusions can be drawn.

- The soil packing effects the lateral load capacity of short rigid piles markedly. The lateral load capacity of the pile in homogeneous dense sand is approximately five times that in homogeneous loose sand.
- The lateral load capacities obtained in the layered sand conditions decrease non-linearly as the thickness of the upper loose sand layer increases. The reduction is mainly due to the smaller unit weight and lower stiffness of the upper loose sand layer.
- The lateral displacement observed at the pile head decreases due to a stiffer surface layer with the increasing value of $E_{reference}$.
- The volume of the sand mass mobilized under the lateral load will be more in the case of higher dilatation values. As a result, higher dilatation values will provide greater lateral load capacities and smaller lateral displacements.
- The interface behavior is significantly dependent on sand density. The degree of permanent slipping behavior between the pile and sand surfaces decreases depending on the decreasing value of R_{inter} .
- Failure zones developed around the pile propagate greater lateral distances and greater depths with the decreasing thickness of the upper loose sand layer.
- The laterally loaded pile problem has been modeled satisfactorily using a three-dimensional non-linear finite-element method.
- Contrary to the assumption made by conventional methods, the distribution of the lateral effective stresses is not linear along the pile embedded depth. The method suggested by Meyerhof et al. [14] produces very conservative lateral load capacities in the layered sand conditions considered.
- The value of the ultimate lateral load capacity could be significantly different depending on the methods used.

ACKNOWLEDGMENTS

The authors thank the Cukurova University Scientific Research Project Directorate for supporting this study (Project no: MMF2006D2).

REFERENCES

- [1] Fan, C.C. and Long, J.H. (2005). Assessment of existing methods for predicting soil response of laterally loaded piles in sand. *Computers and Geotechnics*, 32, 274-289.
- [2] Johnson, K., Lemcke, P., Karunasena, W. and Sivakugan, N. (2006). Modelling the load-deformation response of deep foundations under oblique loading. *Environmental Modelling and Software*, 21, 1375-1380.
- [3] Shen, C.K., Bang, S., Desalvatore, M. and Poran, C.J. (1988). Laterally Loaded Cast-in-Drilled-Hole Piles. *Transportation Research Record*, 1191, 155-165.
- [4] Nazir, R. (1994). *The moment-carrying capacity of short piles in sand*. Ph.D. thesis, University of Liverpool, U.K.
- [5] Laman, M. (1995). *The moment carrying capacity of short pier foundations in clay*. Ph.D. thesis, University of Liverpool, U.K.
- [6] King, G.J.W. and Laman, M. (1995). Conventional and centrifuge model studies of the moment-carrying capacity of short pier foundation in clay. *Canadian Geotechnical Journal*, 32, 976-988.
- [7] Dickin, E.A. and Nazir, R. (1999). Moment-carrying capacity of short pile foundations in cohesionless soil. *Journal of Geotechnical and Geoenvironmental Engineering*, ASCE, 125 (1), 1-10.
- [8] Dickin, E.A. and Laman, M. (2003). Moment response of short rectangular piers in sand. *Computers and Structures*, 81, 2717-2729.
- [9] Chae, K.S., Ugai, K. and Wakai, A. (2004). Lateral resistance of short single piles and pile groups located near slopes. *International Journal of Geomechanics*, 4(2), 93-103.
- [10] Hu, Z., McVay, M., Bloomquist, D., Herrera, R. and Lai, P. (2006). Influence of torque on lateral capacity of drilled shafts in sands. *Journal of Geotechnical and Geoenvironmental Engineering*, ASCE, 132 (4), 456-464.
- [11] Lee, S.W., Pickles, A.R. and Henderson, T.O. (2006). Numerical modeling of laterally loaded short pile. *Numerical Methods in Geotechnical Engineering-Schweiger (ed.)*. Taylor&Francis Group, London.

- [12] Brinch-Hansen, J. (1961). The ultimate resistance of rigid piles against transversal forces. *Geoteknisk Institut (The Danish Geotechnical Institute)*, Bulletin No. 12, 5-9.
- [13] Broms, B.B. (1964). Lateral resistance of piles in cohesionless soils. *Journal of Soil Mechanics and Foundations Division, ASCE*, 90 (3), 123-156.
- [14] Meyerhof, G.G., Mathur, S.K. and Valsangkar, A.J. (1981). Lateral resistance and deflection of rigid walls and piles in layered soils. *Canadian Geotechnical Journal*, 18, 159-170.
- [15] Prasad, Y.V.S.N. and Chari, T.R. (1999). Lateral capacity of model rigid piles in cohesionless soils. *Soils and Foundations*, 39 (2), 21-29.
- [16] Zhang, L., Silva, F. and Grismala, R. (2005). Ultimate lateral resistance to piles in cohesionless soils. *Journal of Geotechnical and Geoenvironmental Engineering, ASCE*, 131 (1), 78-83.
- [17] Muqtadir, A. and Desai, C.S. (1986). Three-dimensional analysis of a pile-group foundation. *International Journal for Numerical and Analytical Methods in Geomechanics*, 10, 41-58.
- [18] Brown, D.A. and Shie, C.F. (1990). Three-dimensional finite element model of laterally loaded piles. *Computers and Geotechnics*, 10, 59-79.
- [19] Trochanis, A.M., Bielak, J. and Christiano, P. (1991). Three-dimensional nonlinear study of piles. *Journal of Geotechnical Engineering, ASCE*, 117 (3), 429-447.
- [20] Wakai, A., Gose, S. and Ugai, K. (1999). 3-D Elasto-plastic finite element analyses of pile foundations subjected to lateral loading. *Soils and Foundations*, 39(1), 97-111.
- [21] Yang, Z. and Jeremic, B. (2003). Numerical study of group effects for pile groups in sands. *International Journal for Numerical and Analytical Methods in Geomechanics*, 27, 1255-1276.
- [22] Martin, G.R. and Chen, C.Y. (2005). Response of piles due to lateral slope movement. *Computers and Structures*, 83, 588-598.
- [23] Karthigeyan, S., Ramakrishna, V.V.G.S.T. and Rajagopal, K. (2006). Influence of vertical load on the lateral response of piles in sand. *Computers and Geotechnics*, 33, 121-131.
- [24] Karthigeyan, S., Ramakrishna, V.V.G.S.T. and Rajagopal, K. (2007). Numerical investigation of the effect of vertical load on the lateral response of piles. *Journal of Geotechnical and Geoenvironmental Engineering, ASCE*, 133 (5), 512-521.
- [25] Yang, Z. and Jeremic, B. (2005). Study of soil layering effects on lateral loading behavior of piles. *Journal of Geotechnical and Geoenvironmental Engineering, ASCE*, 131 (6), 762-770.
- [26] Yang, K. and Liang, R. (2006). Numerical solution for laterally loaded piles in a two-layer soil profile. *Journal of Geotechnical and Geoenvironmental Engineering*, 132 (11), 1436-1443.
- [27] Avaei, A., Ghotbi, A.R. and Aryafar, M. (2008). Investigation of pile-soil interaction subjected to lateral loads in layered soils. *American Journal of Engineering and Applied Sciences*, 1 (1), 76-81.
- [28] Czerniak, E. (1957). Resistance to overturning of single, short piles. *Journal of the Structural Division, Proceedings of the American Society of Civil Engineers*, 83 (2), 1188, 1-25.
- [29] Terzaghi, K. (1955). Evaluation of coefficients of subgrade reaction. *Geotechnique*, 5(4), 297-326.
- [30] El Naggar, M.H. and Wei, J.Q. (1999). Response of tapered piles subjected to lateral loading. *Canadian Geotechnical Journal*, 36, 52-71.
- [31] Sawwaf, M.E. (2006). Lateral resistance of single pile located near geosynthetic reinforced slope. *Journal of Geotechnical and Geoenvironmental Engineering*, 132 (10), 1336-1345.
- [32] Zienkiewicz, R.F. and Taylor, R.L. (1994). *The finite element method (4th edn)*. McGraw-Hill, London, U.K.
- [33] Bolton, M.D. (1986). The strength and dilatancy of sands. *Geotechnique*, 36(1), 65-78.
- [34] Laman, M., King, G.J.W. and Dickin, E.A. (1999). Three-dimensional finite element studies of the moment-carrying capacity of short pier foundations in cohesionless soil. *Computers and Geotechnics*, 25, 141-155.
- [35] Jaky, J. (1944). The coefficient of earth pressure at rest. *Journal for Society Hungarian Architects and Engineers*, 78, 355-358.
- [36] Maeda, K. and Miura, K. (1999). Confining stress dependency of mechanical properties of sands. *Soils and Foundations*, 39 (1), 53-67.
- [37] Matlock, H. and Reese, L.C. (1960). Generalized solutions for laterally loaded piles. *Journal of Soil Mechanics and Foundations Division, ASCE*, 86 (5), 63-91.
- [38] Ng, P.C.F., Pyrah, I.C. and Anderson, W.F. (1997). Assessment of the interface elements and modification of the interface element in CRISP90. *Computers and Geotechnics*, 21 (4), 315-339.
- [39] Lee, J., Kim, M. and Kyung, D. (2010). Estimation of lateral load capacity of rigid short piles in sands using CPT results. *Journal of Geotechnical and Geoenvironmental Engineering, ASCE*, 136 (1), 48-56.
- [40] Yang, K. (2005). Lateral capacity of drilled-shafts considering push-pull resistance. *Proceedings of Deep Foundations Institute 30th Annual Conference on Deep Foundations*, Chicago, IL, 527-536.

- [41] Reese, L.C. (1997). Analysis of laterally loaded piles in weak rock. *Journal of Geotechnical and Geoenvironmental Engineering, ASCE*, 123 (11), 1010-1017.
- [42] Hameed, R.A., Gunaratne, M., Putcha, S., Kuo, C. and Johnson, S. (2000). Lateral load behavior of jetted piles. *Geotechnical Testing Journal*, 23 (3), 358-368.
- [43] Franke, E. and Muth, G. (1985). Scale effect in 1g model tests on horizontally loaded piles. *Proceedings of the 11th International Conference of Soil Mechanics and Foundation Engineering*. San Francisco, 2, 1011-1014.
- [44] Ovesen, N.K. (1979). The use of physical models in design: the scaling law relationship. *Proceedings of the 7th European Conference on Soil Mechanics and Foundation Engineering*. 4, 318-323.

OCENA UDORA KOTLINE STARČA (HRVAŠKA) Z UPORABO STROJNEGA UČENJA ALGORITMOV

MILOŠ MARJANOVIĆ, MILOŠ KOVAČEVIĆ, BRANISLAV BAJAT,
SNJEŽANA MIHALIĆ IŃ BILJANA ABOLMASOV

o avtorjih

Miloš Marjanović
Palacky University,
Faculty of Science
Tř. Svobody 26, 77 146 Olomouc, Češka Republika
E-pošta: milos.marjanovic01@upol.cz

Miloš Kovačević
University of Belgrade,
Faculty of Civil Engineering
Bulevar kralja Aleksandra 73, 11000 Beograd, Srbija
E-pošta: milos@grf.bg.ac.rs

Branislav Bajat
University of Belgrade,
Faculty of Civil Engineering
Bulevar kralja Aleksandra 73, 11000 Beograd, Srbija
E-pošta: bajat@grf.bg.ac.rs

Snježana Mihalić
University of Zagreb,
Faculty of Mining, Geology and Petroleum Engineering
Pierottijeva 6, p.p. 390, 10000 Zagreb, Hrvatska
E-pošta: smihalic@rgn.hr

vodilni avtor

Biljana Abolmasov
University of Belgrade,
Faculty of Mining and Geology
Đušina 7, 11000 Beograd, Srbija
E-pošta: biljana@rgf.bg.ac.rs

izvleček

V tej raziskavi so avtorji primerjali algoritme strojnega učenja v okviru prognoze drsenja terena. Na osnovi GIS slojev področja kotline Starča, ki so vključevali geološke, hidrogeološke, morfometrijske in druge prostorske podatke, je napravljena klasifikacija mrežnih celic na (i) primerih »drsečega« in »stabilnega terena«, (ii) različnih tipih drsečega terena (»potencialen-neaktiven«, »stabiliziran-saniran« in »reaktiviran«). Po optimizaciji parametrov modela za C4.5 decision trees in Support Vector Machines so primerjali dobljene rezultate klasifikacije s pomočjo kappa statistike. Rezultati kažejo, da sta omenjena modela bolje razlikovala med različnimi tipi drsečega terena kot med drsečim in stabilnim terenom. Prav tako je bil klasifikator Support Vector Machines v vseh preizkusih nekoliko uspešnejši od C4.5. Spodbudne rezultate so dobili v eksperimentu, kjer so klasificirali različne tipe drsečega terena, uporabili pa so samo 20% od skupnega števila podatkov o drsečem terenu. V tem primeru so za oba klasifikatorja dobili vrednost kappa okoli 0.65.

ključne besede

plazovi, support vector machines, decision trees klasifikator, kotlina Starča

LANDSLIDE ASSESSMENT OF THE STARČA BASIN (CROATIA) USING MACHINE LEARNING ALGORITHMS

MILOŠ MARJANOVIĆ, MILOŠ KOVAČEVIĆ, BRANISLAV BAJAT,
SNJEŽANA MIHALIĆ and BILJANA ABOLMASOV

about the authors

Miloš Marjanović
Palacky University,
Faculty of Science
Tř. Svobodý 26, 77 146 Olomouc, Czech Republic
E-mail: milos.marjanovic01@upol.cz

Miloš Kovačević
University of Belgrade,
Faculty of Civil Engineering
Bulevar kralja Aleksandra 73, 11000 Belgrade, Serbia
E-mail: milos@grf.bg.ac.rs

Branislav Bajat
University of Belgrade,
Faculty of Civil Engineering
Bulevar kralja Aleksandra 73, 11000 Belgrade, Serbia
E-mail: bajat@grf.bg.ac.rs

Snježana Mihalić
University of Zagreb,
Faculty of Mining, Geology and Petroleum Engineering
Pierottijeva 6, p.p. 390, 10000 Zagreb, Croatia
E-mail: smihalic@rgn.hr

corresponding author

Biljana Abolmasov
University of Belgrade,
Faculty of Mining and Geology
Đušina 7, 11000 Belgrade, Serbia
E-mail: biljana@rgf.bg.ac.rs

abstract

In this research, machine learning algorithms were compared in a landslide-susceptibility assessment. Given the input set of GIS layers for the Starča Basin, which included geological, hydrogeological, morphometric, and environmental data, a classification task was performed to classify the grid cells to: (i) landslide and non-landslide cases, (ii) different landslide types (dormant and abandoned, stabilized and suspended, reactivated). After finding the optimal parameters, C4.5 decision trees and Support Vector Machines were compared using kappa

statistics. The obtained results showed that classifiers were able to distinguish between the different landslide types better than between the landslide and non-landslide instances. In addition, the Support Vector Machines classifier performed slightly better than the C4.5 in all the experiments. Promising results were achieved when classifying the grid cells into different landslide types using 20% of all the available landslide data for the model creation, reaching kappa values of about 0.65 for both algorithms.

keywords

landslides, support vector machines, decision trees classifier, Starča Basin

1 INTRODUCTION

Prior to any conceptualizing and modeling, dealing with the landslide phenomenology requires a profound understanding of the triggering and conditioning factors that are in control of the landslide process. Difficulties in landslide-assessment practice arise from the temporal and spatial variability of the triggering and conditioning factors and the changes in the nature of their interaction [1]. This research concentrates only on the spatial aspect of landslide distribution, i.e., delimiting landslide-prone areas, also known as landslide-susceptibility zoning. Only selected conditioning factors (geological, hydrological, morphological, anthropogenic, etc.) addressing natural ground properties and environmental conditions were included in the investigation.

A conceptual standard developed for the landslide assessment [2] was adhered to, and this involved: (i) generation of a landslide inventory, (ii) identification and modeling of a set of natural factors that are indirectly conditioning the slope instability, (iii) estimation of the relative contribution of these factors in generating slope failures, and (iv) classification of land surface into domains of different susceptibility degrees, in our case with respect

to (i). The essential idea behind it suggests that if there were landslide occurrences under certain conditions in the past, it is quite likely that a similar association of conditions will lead to new occurrences [2]. The estimation of the relative contribution of a factor in the overall stability (iii) (which herein comes down to a classification problem) ranges over a broad variety of methods [3]. These include the Analytical Hierarchy Process (AHP) [4], conditional probability [5], discriminant analysis [6], different kinds of regression models [7], Fuzzy Logics [8], Support Vector Machines (SVMs) [9], Artificial Neural Networks (ANNs) [10] and decision trees [11]. Relatively few researchers have dealt with the machine learning approach, but recently it is getting more popular in geoscientific communities, especially for comparative studies of landslide susceptibility [12], [13].

Following such a trend, we herein utilized C4.5 decision trees and SVM algorithms for mapping landslides and distinguishing between different landslide categories. Thus far, researchers did not experiment with multi-class classifications (usually binary classification case studies can be found in the literature) and here we challenged the classification in that context. The theoretical advantages of the chosen machine learning approaches are numerous, particularly regarding the handling of data with different scales and types, independence from statistical distribution assumptions (the drawbacks of regression and discriminant methods) and so forth [14], which was also one of the motifs for its implementation in present research.

The proposed model might serve for a landslide-susceptibility assessment in other areas of the City of Zagreb, under the assumption of similar terrain properties, primarily geological ones. These are urbanized and densely populated areas, hence less explorative for the field investigation of landslides. In such circumstances, the presented approach might lead to certain benefits, but more detailed investigations are needed to obtain reliable results. The latter involves testing the model against several pilot areas and tracking its performance. The biggest obstacle to the completion of that goal is a lack of detailed landslide inventories at the moment.

2 METHODS

The different stages of research called for different procedures, imposing a variety of methods, including the pre-processing of input attributes, machine learning implementation, and performance evaluation. All the related machine learning experiments and the subsequent algorithm-performance evaluation were placed in an open-source package, Weka 3.6 [15].

Assuming that our inputs are organized as raster sets where each grid element (pixel) represents a data instance at a certain point of the terrain, our approach leads to a classification task that places each pixel from any terrain attribute raster into an appropriate landslide category associated with that particular pixel. We will herein explain the classification problem and machine learning solution in depth, and from the perspective of their particular application in landslide-susceptibility assessment.

2.1 PROBLEM FORMULATION

Let $P=\{\mathbf{x}|\mathbf{x}\in R^n\}$ be a set of all the possible pixels extracted from the raster representation of a given terrain. Each pixel is represented as an n -dimensional real vector where the coordinate x_i represents a value of the i -th terrain attribute associated with the pixel \mathbf{x} . Further, let $C=\{c_1, c_2, \dots, c_l\}$ be a set of l disjunctive, predefined landslide categories ($j=1, l$). A function $f_c: P \rightarrow C$ is called a classification if for each $\mathbf{x}_i \in P$ it holds that $f_c(\mathbf{x}_i)=j$ whenever a pixel \mathbf{x}_i belongs to the landslide category c_j . In practice, for a given terrain, one has a limited set of m -labeled examples ($i=1, m$) which form a training set (\mathbf{x}_i, c_i) , $\mathbf{x}_i \in R^n$, $c_i \in C$, $i=1, \dots, m$ (m being a reasonably small number of instances). The machine learning approach tries to find a decision function f_c' which is a good approximation of a real, unknown function f_c , using only the examples from the training set and a specific learning method [16].

2.2 SUPPORT VECTOR MACHINES CLASSIFIER

Originally, a SVM is a linear binary classifier (instances could be classified to only one of the two classes), but one can easily transform an n -classes problem into a sequence of n (one-versus-all) or $n(n-1)/2$ (one-versus-one) binary classification tasks, where using different voting schemes leads to a final decision [17]. Given a binary training set (\mathbf{x}_i, y_i) , $\mathbf{x}_i \in R^n$, $y_i \in \{-1, 1\}$, $i=1, \dots, m$, the basic variant of the SVM algorithm attempts to generate a separating hyper-plane in the original space of n coordinates (x_i parameters in vector \mathbf{x}) between two distinct classes (Fig. 1). During the training phase the algorithm seeks out a hyper-plane that best separates the samples of binary classes (classes 1 and -1). Let $h_1: \mathbf{w}\mathbf{x} + b = 1$ and $h_{-1}: \mathbf{w}\mathbf{x} + b = -1$ ($\mathbf{w}, \mathbf{x} \in R^n$, $b \in R$) be possible hyper-planes such that the majority of class 1 instances lie above h_1 ($\mathbf{w}\mathbf{x} + b > 1$) and the majority of class -1 fall below h_{-1} ($\mathbf{w}\mathbf{x} + b < -1$), whereas the elements belonging to h_1, h_{-1} are defined as Support Vectors (Fig. 1). Finding another hyper-plane $h: \mathbf{w}\mathbf{x} + b = 0$ as the best separating (lying in the middle of h_1, h_{-1}), assumes calculating \mathbf{w} and b , i.e., solving the nonlinear convex programming problem.

The notion of the best separation can be formulated as finding the maximum margin M between the two classes. Since $M = 2\|\mathbf{w}\|^{-1}$ maximizing the margin leads to the constrained optimization problem of Eq. (1).

$$\min_{\mathbf{w}, b} \frac{1}{2}\|\mathbf{w}\|^2 + C\sum_i \varepsilon_i \quad (1)$$

w.r.t: $1 - \varepsilon_i - y_i(\mathbf{w} \cdot \mathbf{x}_i + b) \leq 0, \quad -\varepsilon_i \leq 0, \quad i = 1, 2, \dots, m$

Despite having some of the instances misclassified (Fig. 1) it is still possible to balance between the incorrectly classified instances and the width of the separating margin. In this context, the positive slack variables ε_i and the penalty parameter C are introduced. Slacks represent the distances of the misclassified points to the initial hyper-plane, while parameter C models the penalty for misclassified training points, that trades-off the margin size for the number of erroneous classifications (the bigger the C the smaller the number of misclassifications and the smaller the margin). The goal is to find a hyper-plane that minimizes the misclassification errors while maximizing the margin between classes. This optimization problem is usually solved in its dual form (dual space of Lagrange multipliers):

$$\mathbf{w}^* = \sum_{i=1}^m \alpha_i y_i \mathbf{x}_i, \quad C \geq \alpha_i \geq 0, \quad i = 1, \dots, m, \quad (2)$$

where \mathbf{w}^* is a linear combination of training examples for an optimal hyper-plane.

However, it can be shown that \mathbf{w}^* represents a linear combination of Support Vectors \mathbf{x}_i for which the corresponding α_i Lagrangian multipliers are non-zero values. Support Vectors for which the $C > \alpha_i > 0$ condi-

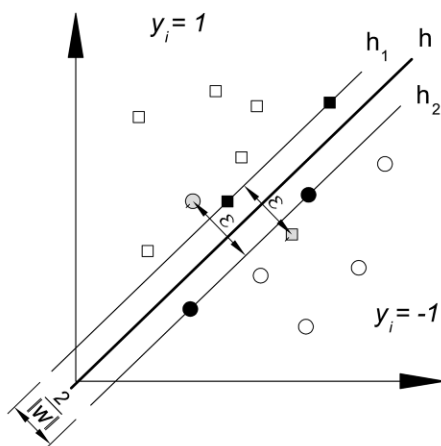


Figure 1. General binary classification case ($h_0: \mathbf{w}\mathbf{x}+b=0$; $h_1: \mathbf{w}\mathbf{x}+b=1$; $h_2: \mathbf{w}\mathbf{x}+b=-1$). Shaded points represent misclassified instances.

tion holds, belong either to h_1 or h_{-1} . Let \mathbf{x}_a and \mathbf{x}_b be two such Support Vectors ($C > \alpha_a, \alpha_b > 0$) for which $y_a = 1$ and $y_b = -1$. Now b could be calculated from $b^* = -0.5\mathbf{w}^*(\mathbf{x}_a + \mathbf{x}_b)$, so that the classification (decision) function finally becomes:

$$f(\mathbf{x}) = \text{sgn} \sum_{i=1}^m \alpha_i y_i (\mathbf{x}_i \cdot \mathbf{x}) + b^* \quad (3)$$

In order to cope with non-linearity even further, one can propose the mapping of instances to a so-called feature space of very high dimension: $\phi: R^n \rightarrow R^d, n \ll d$, i.e., $\mathbf{x} \rightarrow \phi(\mathbf{x})$. The basic idea of this mapping into a high-dimensional space is to transform the non-linear case into linear and then use the general algorithm, as already explained Eqs. (1-3). In such space, the dot-product from Eq. (3) transforms into $\phi(\mathbf{x}_i) \cdot \phi(\mathbf{x})$. A certain class of functions for which $k(\mathbf{x}, \mathbf{y}) = \phi(\mathbf{x}) \cdot \phi(\mathbf{y})$ holds are called kernels [18]. They represent dot-products in some high-dimensional dot-product spaces (feature spaces), and yet could be easily computed into the original space. After initial testing on our sets, a Radial Basis Function (Eq. 4), also known as a Gaussian kernel [19], gave encouraging results and was implemented in the experimental procedure.

$$k(\mathbf{x}, \mathbf{y}) = \exp(-\gamma\|\mathbf{x} - \mathbf{y}\|^2) \quad (4)$$

Now Eq. (3) becomes:

$$f(\mathbf{x}) = \text{sgn} \sum_{i=1}^m \alpha_i y_i k(\mathbf{x}_i \cdot \mathbf{x}) + b^* \quad (5)$$

After removing all the training data that are not Support Vectors and retraining the classifier by applying the function above, the same result would be obtained as in the case of classifying with all the available training instances [18]. Thus, the ones depicted, Support Vectors could replace the entire training set containing all the necessary information for the construction of the separating hyper-plane.

2.3 DECISION TREE CLASSIFIER (C4.5)

C4.5 is a well-known univariate decision-tree classifier [20]. In this approach, an instance (described with a set of attributes) is classified by testing the value of one particular attribute per each node, starting from the root of the tree. It then follows a certain path in the tree structure, depending on the tests in previous nodes and finally reaches one of the leaf nodes labeled with a class label. Each path leading from the root to a certain leaf node (class label) can be interpreted as a conjunction of tests involving attributes on that path. Since there could be more leaf nodes with the same class labels, one could interpret each class as a disjunction of conjunctions of constraints on the attribute values of instances from

the dataset. The interpretability of the derived model enables a domain expert to have a better understanding of the problem and in many cases could be preferable to functional models such as SVMs.

Let us briefly explain how the tree can be derived from the training data (x_i, c_i) , $i=1, \dots, m$, where c_i is one of k disjunctive classes. C4.5 deals both with numerical and categorical attributes, but for the sake of simplicity we first made an assumption that all attributes are categorical. The tree construction process performs a greedy search in the space of all possible trees starting from the empty tree and adding new nodes in order to increase the classification accuracy on the training set. A new node (candidate attribute test) is added below a particular branch if the instances following the branch are partitioned after the test in such way that the distinction between the classes becomes more evident. If the test on attribute A splits the instances into subsets in which all elements have the same class labels that would be a perfect attribute choice (those subsets become leaf nodes). On the other hand, if the instances are distributed so that in each subset there are equal numbers of elements belonging to different classes, then A would be the worst attribute choice. Hence, the root node should be tested against the most informative attribute concerning the whole training set. C4.5 uses the *Gain Ratio* measure [21] to choose between the available attributes and is heavily dependent on the notion of Entropy. Fig. 2 explains the calculation of *Gain Ratio*.

Let S_{in} be the set of N instances for which the preceding test in the parent node forwarded them to the current node. Further, let n_i be the number of instances from S_{in} that belong to class c_i , $i=1, \dots, k$. The entropy $E(S_{in})$ is defined as a measure of impurity (with respect to the class label) of the set S_{in} as:

$$E(S_{in}) = - \sum_{i=1}^k \frac{n_i}{N} \log_2 \frac{n_i}{N} \quad (6)$$

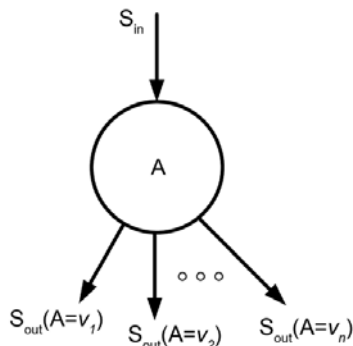


Figure 2. Calculating *Gain Ratio* of an attribute in the internal node of the growing tree.

If all instances belong to the same class then the entropy is zero. On the other hand, if all classes are equally present, the entropy is a maximum $(\log_2 k)$. In our problem the setting A denotes the candidate attribute of an instance x . Since by assumption A is categorical and can take n different values v_1, v_2, \dots, v_n , there are n branches leading from the current node. Each $S_{out}(A=v_i)$ represents the set of instances for which A takes the value v_i . The informative capacity of A concerning the classification into k predefined classes can be expressed by using the notion of *Information Gain*:

$$IG(S_{in}, A) = E(S_{in}) - \sum_{v \in \{v_1, \dots, v_n\}} \frac{|S_{out}(A=v)|}{N} E(S_{out}(A=v)) \quad (7)$$

In Eq. (7) $|S_{out}(A=v)|$ represents the number of instances in the set $S_{out}(A=v)$ and $E(S_{out}(A=v))$ is the entropy of that set calculated using Eq. (6). The higher is the IG , the more informative is the A for the classification in the current node, and vice versa [14].

The main disadvantage of the IG measure is that it favors attributes with many values over those with fewer. This leads to wide trees with many branches starting from corresponding nodes. If the tree is complex and has a lot of leaf nodes, then it is expected that the model will overfit the data (it will learn the anomalies of the training data and its generalization capacity, i.e., the classification accuracy on unseen instances, will be decreased). In order to reduce the effect of overfitting C4.5 further normalizes IG by the entropy calculated with respect to the attribute values instead of class labels (*Split Information*) to obtain the *Gain Ratio* (GR):

$$SI(S_{in}, A) = - \sum_{v \in \{v_1, \dots, v_n\}} \frac{|S_{out}(A=v)|}{N} \log_2 \frac{|S_{out}(A=v)|}{N} \quad (8)$$

$$GR(S_{in}, A) = \frac{IG(S_{in}, A)}{SI(S_{in}, A)}$$

C4.5 uses GR to drive the greedy search over all possible trees. If the attribute is numerical (this is the case for most attributes in our application) C4.5 detects the candidate thresholds that separate the instances into different classes. Let (A, c_i) pairs be $(50, 0)$, $(60, 1)$, $(70, 1)$, $(80, 1)$, $(90, 0)$, $(100, 0)$. C4.5 identifies two thresholds on the boundaries of different classes: $A < 55$ and $A < 85$. A now becomes a binary attribute (true or false) and the same GR procedure is applied to select from among the two thresholds, when considering the introduction of this attribute test into the growing tree.

Finally, C4.5 uses the so-called post-pruning technique to reduce the size of the tree (complexity of the model). After growing the tree that classifies all the training examples as

well as possible (overfitted model) it converts the tree into a set of equivalent rules, one rule of the form *if* $A=v$ *and* $B<w$ *and* ... *then* c_i per each leaf node (a path from the root to a leaf). It then prunes the rules by removing every condition that does not affect the estimated rule accuracy, and then sorts the pruned rules by their estimated accuracy. In the operational phase, C4.5 uses sorted pruned rules for the classification of unseen instances.

C4.5 calculates observed estimates for rules using the training set as a whole (the number of correctly classified instances/number of total instances per each leaf) and then calculating the standard deviation assuming a binomial distribution. For a given confidence level, the lower bound estimate is taken as the measure of the rule accuracy. There are many variants of the pruning technique, but all of them can be compared with the adjusting parameter C in the SVM algorithm, since both trade-off the training error versus the model complexity in order to increase the generalization power of the induced classification model. In this paper we used the Weka J48 implementation of the C4.5 algorithm.

2.4 EVALUATION MEASUREMENT

The quality of the classification could be simply estimated as a relation between the correctly classified and misclassified instances, but the problem of proper evaluation of spatial outputs turns out to be more complex [22], and requires more sophisticated solutions. Herein, a parameter called κ (kappa)-index was proposed.

It represents a measure of the agreement between compared entities, rather than the measure of the classification performance [23]. It turns out to be quite convenient for a comparison of the maps with the same classes [24], as was the case in this. The best way to compute the κ -index is to derive it from a confusion matrix, an $n \times n$ cross-tabulation table (n being the number of classes) in which x_{rc} represents the number of pixels from the actual class c that are classified by a classifier as the class r .

$$\kappa = (N \sum_i x_{ii} - \sum_i x_{i+} x_{+i}) / (N^2 - \sum_i x_{i+} x_{+i}) \quad (9)$$

In Eq. (9) N represents the total number of tested pixels, while x_{i+} and x_{+i} are the total numbers of observations in a particular row and column of the confusion matrix, respectively. The idea of the κ -index is to remove the effect of the random agreement between the two experts (here between a referent landslide inventory and a classifier). The obtained index ranges from -1 for the complete absence of agreement, to $+1$ for the absolute agreement, while a zero value suggests that the agreement is random. Based on [25] κ values falling in the 0.61 – 0.81 range are categorized as substantial, and values higher than 0.81 are considered as nearly perfect.

3 CASE STUDY AND INPUT DATA

The Starča Basin encompasses 12.25 km^2 of a hilly landscape (up to 300 m in elevation) on the outskirts of the Samobor Mountains, which represent the western

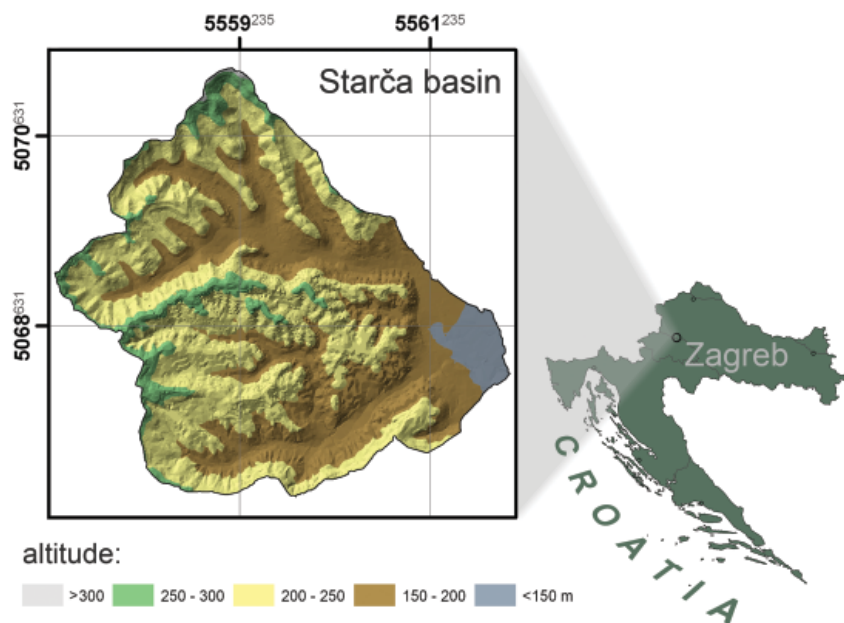


Figure 3. Geographic location of the study area (Gauss Krüger projection, zone 5).

border of the City of Zagreb, Croatia (Fig. 3). This area is composed of the Upper Miocene and Plio-Quaternary sediments. The ground conditions, morphological settings and urbanization of the area could be considered as the primary causal factors for numerous shallow and relatively small landslides triggered by physical (e.g., intense, short period rainfall) or man-made processes.

The resources for generating the input dataset of the Starča Basin included: landslide inventory; Digital Terrain Model (DTM); geological map; hydrogeological map; and a land-cover map. From the above-mentioned resources, the input dataset was generated as an assembly of attributes. Using the advantages of GIS software platforms (ArcGIS and SagaGIS) the input data were processed, i.e., referenced and normalized (where applicable) and stored in a raster image format so that every pixel (every center node of the pixel to be more exact) represents one instance. Every attribute within the input dataset contained 122513 instances with a 10-m cell resolution.

3.1 LANDSLIDE INVENTORY

A detailed geomorphological landslide map was prepared through a systematic field survey (in the period of March–April 2004) at 1:5000 scale (Fig. 4). The total mapped landslide area reached only 0.87 km² (or 7.1% of the study area, which is statistically speaking, an undesirable proportion), with a density of about 0.1 slope failures per km². The landslide inventory was prepared in the form of a GIS database in which information on the location, features and abundance of 230 mapped landslides is archived [26]. The main landslide characteristics were described according to standard WP/WLI (1993) recommendations [27]. Landslides were classified as (shallow) slide type according to Cruden and Varnes Classification [28], with the age and state of activity determined according to the morphological indicators.

Active, suspended and reactivated landslides have clearly recognizable fresh scars, without any vegetation cover, because of movement within the past few years (59 slides). Most of the landslides are inactive and they are classified as: dormant landslides (95 slides) have recognizable scars covered by vegetation during the period of inactivity; abandoned landslides (72 slides) are characterised by a hummocky surface topography and relics of scars completely smoothed during the period of inactivity; and stabilized landslides included those mitigated by engineering measures (4 slides). Relict landslides (40 slides) are difficult to recognize, because the only indicator of movement is a typical roughly undulating slope morphology: concave depletion zone in the upper part and convex accumulation zone in the lower part.

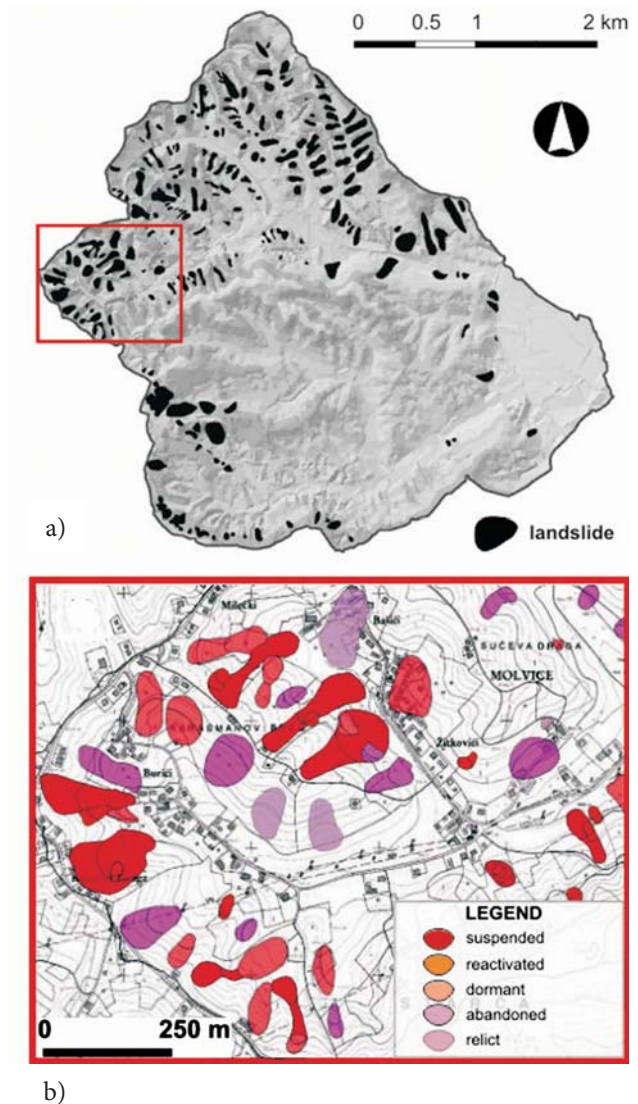


Figure 4. a) Landslide distribution in the basin area, b) Enlargement of a geomorphological landslide map, original scale 1:5000.

The size of the landslides varies from 270 m² to 25.073 m². Most of the landslides range in size from 400 m² to 1600 m². Regarding activity style, there are single movements (150 slides) as well as complex, composite, successive and multiple movements (120 slides). ‘Parent-child’ relationships were also defined during the mapping. The relict slides are excluded from any further analysis because of the mapping uncertainty.

For the purpose of this research, the landslide inventory is used only in a raster-image form. The landslide inventory was somewhat simplified for the purpose of this research in order to enhance the statistical representativeness of the categories (the merging of the original categories was based on the activity stage).

3.2 CONDITIONING FACTORS – TERRAIN ATTRIBUTES

The landslide-conditioning factors involved a variety of input layers, some being directly digitized from the original thematic maps, others derived from additional spatial calculations and modeling. In effect, 15 input-raster layers, with the same 10 m cell resolution, were available for further analysis. These could be divided into three thematic groups: geological, morphological, and environmental factors. Note also that the factors that turned more dominant in this research are somewhat detailed in the description.

Geological factors included layers derived from the 1:5000 geological map, indicating the main geological units in the area and the approximately located faults [29]:

- Lithology (representing 10 rock units as categorical classes¹) Eight main lithological types can be distinguished (Fig. 5a): eluvial clay and silty clay with gravel (Quaternary), alluvial gravel with silty clay (Quaternary), gravel with silty clay (Plio-Pleistocene), coarse-grained sand (Plio-Pleistocene), sandy silt and silt (Pontian), marl with silt and calcareous siltstone (Pannonian), laminated marl with calcareous sandstone (Sarmatian) and marl (Badenian). Considering the relatively high proportion of clayey and marly units, the lithological model suggests that shallow to deep-seated landslides could be hosted on a significant part of the area (Fig. 5a)
- Proximity to the fault lines

A high precision terrain surface model (± 1 m) was developed through the photogrammetric technique, in

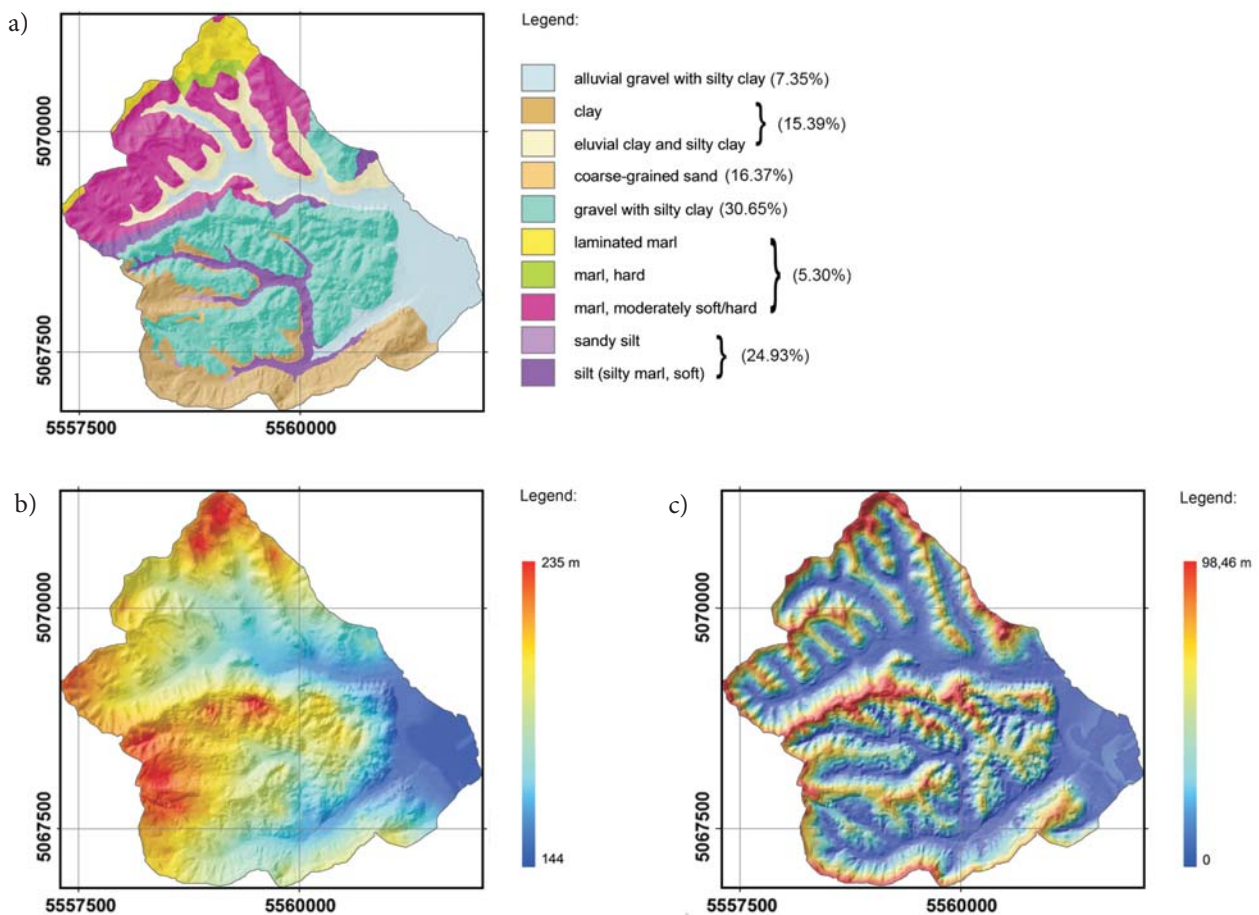


Figure 5. a) Attribute *lithological units* with the breakdown of the percentage proportion of unit groups, b) Attribute *channel network base levels*, c) Attribute *altitude above channel network*; Note that the selection of these three thematic layers corresponds with the three most important attributes in Table 2.

¹The categorical attributes were extended into n binary attributes, coding n different initial values (e.g., class 1 and 4 of Lithology are coded as 1000000000 and 0001000000, respectively, while the same classes for Land Use were 1000 and 0001), in order to give equal preference to every class.

the framework of orthophotomaps production of the Zagreb City area, at a scale of 1:5000. The terrain model was subsequently transformed to a DTM by means of vector-to-raster conversion. A host of morphometric parameters with a proven relevance for landslide assessment [30] were derived from the DTM:

- Slope
- Downslope gradient (ratio of the slope angle and the elevation)
- Aspect
- Profile Curvature (terrain curvature in the steepest slope direction)
- Plan Curvature (terrain curvature along the contour)
- Convergence Index (slope angle convergence)
- LS factor (ratio of the slope length and the length standardized by the Universal Soil Loss Equation)
- Channel network base level elevations are values calculated as a vertical difference between the real DTM elevations and the elevations of the (interpolated) channel network (Fig. 5b). It provides information on how far each cell is from the local flow, just by interpreting the higher differences as more remote than the lower ones (in channel cells the attribute's value is zero, while in non-channel cells the value is increasing with the distance from the flow)
- Altitude above the channel network is another standard morphometric terrain attribute, yet sometimes important to determine the relief energy based on potential energy differences (height differences) between each cell and its local erosional basis (Fig. 5c). It is basically a DTM downshifted by the value of the channel cells elevations.
- Stream Power Index (potential power of the flows given by a relation of the local drainage area and the local slope gradient)
- Topographic Wetness Index (topographic water retention potential given by a relation of the upslope drainage area and the slope gradient)

Piezometric map, an interpolation of the maximum piezometric pressure heads, measured in a rainy period of 2004, was used to generate the attribute:

- Groundwater table depth (depths from the measurements of the minimal water levels in wells, interpolated by the nearest-neighbor method, ranged by 4 classes with 0.5 m intervals, i.e., 0–0.5, 0.5–1, 1–1.5 and >1.5 m)

The Land Use map was prepared by a direct visual interpretation of a 1:5000 orthophoto according to the CORINE classification. The map was generalized as the attribute:

- Land Use (a categorical attribute with 4 thematic classes, similarly arranged as in the case of Lithology. The classes included: Agricultural areas 30%, Artificial surfaces 4%, Forests and semi-natural areas 65%, Water bodies 1%)

4 RESULTS AND DISCUSSION

The experimental design was governed by the characteristics of the dataset, particularly the unbalanced distribution of the landslide inventory classes. Since the non-landslide class turned out to be predominant over all the landslide classes combined, the sampling strategy was tuned accordingly. Two different dataset cases were induced:

- S01 with a binary class labels, i.e., class c_1 – absence of landslides, and class c_2 – presence of landslides (Fig. 6a). It contained 20% of the original dataset (randomly selected), or 24500 out of 122513 instances.
- S123 included only landslide instances (Fig. 6b) from the original dataset distributed in three different classes: c_1 – dormant and abandoned, c_2 – stabilized and suspended, and c_3 – reactivated landslides (a total of 10500 instances).

Thus, the classifier trained by the first set was used to locate the landslides throughout the area, while the classifier trained by the second set was used to discern between three landslide types. In this way, featured expert judgment is simulated and could be applied to the remaining part of the terrain, as well as to the adjacent ground. Both sets passed through the identical experimenting protocol discussed subsequently.

For the C4.5 algorithm we used the default parameters of Weka explorer: 0.25 for *confidence level for pruning*, while the *minimum number of objects in leaf* was held at 2. The optimization of SVM also comes down to the fitting of only two parameters: the margin penalty C and the kernel width γ . The parameters are found in a well-established cross-validation procedure² over the training set in each performed experiment [31], [32]. It turns out that the optimal parameters ($C=100$, $\gamma=4$) are the same for all the performed experiments.

- Experiment#1: testing was performed on S01 (24500 instances) and S123 (10500 instances) data in a single run (no iterations), through 10-fold cross-validation (10-CV). The value of the representative κ was

² In k -fold cross-validation (k -CV), the entire set is partitioned into k disjoint splits of the same size. Validation is completed in k iterations, each time using a different split for the validation, and merging the remaining $k-1$ splits for training.

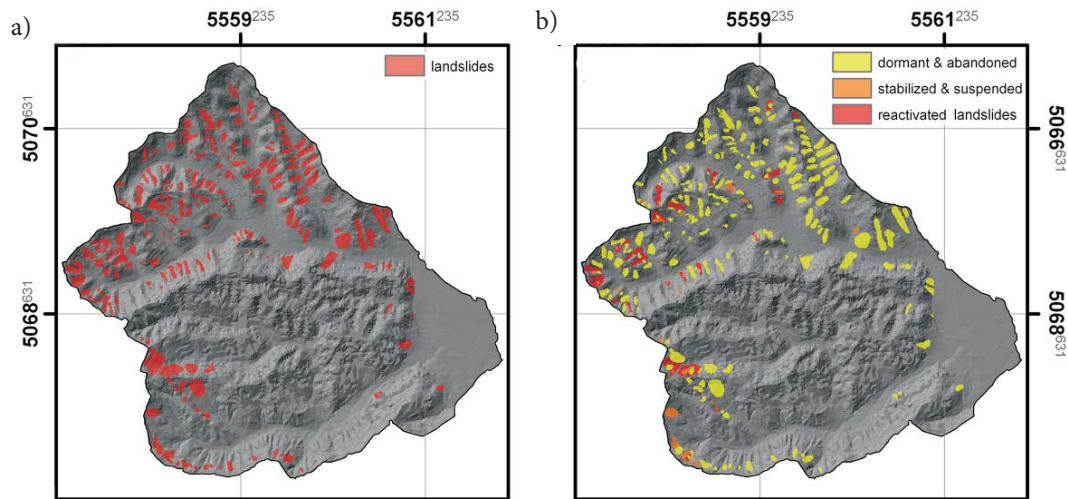


Figure 6. a) Landslide inventory map for S01, b) Different landslide categories (dormant and abandoned 1, stabilized and suspended 2, reactivated 3) for S123.

obtained directly after the cross-validation was run. For the C4.5 algorithm it reached 0.52 in the S01 and 0.82 in the S123 data set. The SVM algorithm reached a very similar performance, i.e., a fraction higher in S01 (Table 1), meaning that it is somewhat more reliable in mapping landslides but equal in discerning between different types of landslides.

- Experiment#2: Both sets were randomly divided into 20–80% splits. The training was performed on 20% of the data (5000 instances in S01 and 2000 instances in S123). In order to obtain statistically relevant results, five different 20–80% splits were generated and the median among the obtained κ values was considered as being representative (Table 1). As expected, the performance drops significantly, especially in S01. It is also apparent that SVM is slightly better than the C4.5 in this set, while in S123 the algorithms are leveled.
- Experiment#3: generating seven 15–85% splits (3800 instances in S01 and 1500 instances in S123 for training purposes), otherwise analogue to the previous. A further decrease of the average κ is noticeable, as well as a slightly advantageous performance of the SVM algorithm (Table 1).
- Experiment#4: generating ten 10–90% splits (2500 instances in S01 and 1000 instances in S123), otherwise analogous to the previous. The dropping trend continues, as κ values became rather temperate for both algorithms within both sets (Table 1).

Viewing the experiment results altogether, a slight preference for the SVM over the C4.5 is obvious in both S01 and S123 data sets, due to the smaller κ decrements (0.03–0.05) with a reduction of the training sample size.

Table 1. Performance evaluation of the C4.5 and SVM classifiers by κ -index.

Experiment	S01		S123	
	C4.5	SVM	C4.5	SVM
#1 (10–CV)	0.52	0.58	0.82	0.82
#2 (5x20–80%)	0.38	0.47	0.63	0.65
#3 (7x15–85%)	0.33	0.44	0.58	0.60
#4 (10x10–90%)	0.31	0.40	0.48	0.55

In all the experiments the algorithms exhibit a better generalization with the S123 set, meaning that they are better in categorizing landslides than actually mapping them, concerning the present study area and the chosen sampling strategy. Preliminary results suggest that using the same input attributes, it would be interesting to impose the algorithms over adjacent areas (which are urbanized, but have similar terrain features) in order to suggest to the expert which types of landslides are present prior to the real field mapping.

Since we have been using a classifier based on information gain values (C4.5), we evaluated the ranking of the input features according to their *IG* values (Table 2). It appears that the most informative layers are Lithology, Channel Network Base Elevations, Altitude Above Channel Network, while surprisingly Slope turned out to be mediocre to low, hand in hand with the terrain Convergence Index and Land Use for instance. One possible way to explain this is an exaggeration of the geological and, to some extent, the hydrogeological influence on the landslide occurrence, so that they obscure the effects of slope steepness and land use for instance.

Table 2. Information Gain (*IG*) ranking of the input layer attributes.

Terrain attribute	<i>IG</i>	rank
Lithology	0.06157	1
Channel Network Base Elevations	0.04034	2
Groundwater Table	0.0268	7
Stream Power Index	0.03038	4
Aspect	0.02828	5
Altitude above channels	0.03078	3
Topographic Wetness Index	0.02789	6
Land Use	0.02129	10
Downslope Gradient	0.02413	8
LS factor	0.02241	9
Slope	0.021	11
Convergence Index	0.01723	12
Plan Curvature	0.008	14
Buffer of Faults	0.00938	13
Profile Curvature	0.00605	15

5 CONCLUSIONS

The general conclusion that can be attached to this study is that it brought about a constructive facet on the machine learning application by challenging the capability of mapping the landslide instances and/or the landslide categories, between two different classifiers. It yielded partly eligible solutions for the posited landslide-assessment problem, especially in terms of particularizing between different types of landslides. Although the classification was not so promising in terms of landslide instances' mapping ($\kappa=0.47$, model derived from 20% of total points), the research gave some encouraging results in terms of categorizing landslide types ($\kappa=0.65$, model derived from 20% of total points). Distinguishing between landslides and non-landslides gave acceptable results only in the case with the maximum training data (90% for training).

When comparing the two algorithms, a small advantage was observed for the SVM over the C4.5 in terms of both aspects (landslide instances mapping versus instances' categorizing). The SVM generalizes better than the concurrent algorithm, especially over smaller training samples, but the C4.5 is less time-consuming and hardware-demanding, and thus should have some preference if time and hardware factors are the prevailing criteria. This research lacked in testing of the model against unknown instances, i.e., instances of adjacent terrains, thus, a major guideline to further the research

is the inclusion of adjacent terrains within the urbanized area of the City of Zagreb, in order to prove or negate the plausibility of the method. The results could then be represented as preliminary landslide forecast map products, not just as performance-evaluation parameters (as in this research), but visually too.

In the future research we plan to estimate the potential increase in the classification accuracy by using an ensemble of different classifiers (C4.5, SVM, Logistic Regression, etc.) and then to combine their individual decisions through various schemes, such as voting or weighting techniques.

REFERENCES

- [1] Carrara, A. and Pike, R. (2008). GIS technology and models for assessing landslide hazard and risk. *Geomorphology* 94, No. 3-4, 257-260.
- [2] Crosta, G.B. and Shlemon, R.J. (eds) (2008). Guidelines for landslide susceptibility, hazard and risk zoning for land use planning. *Engineering Geology* 102, <http://www.australiangeomechanics.org/common/files/lrm/LRM2007-a.pdf>
- [3] Chacón, J., Irigaray, C., Fernández, T. and El Hamdouni, R. (2006). Engineering geology maps: landslides and geographical information systems. *Bulletin of Engineering Geology and the Environment* 65, No. 4, 341-411.
- [4] Komac, M. (2006). A landslide susceptibility model using the Analytical Hierarchy Process method and multivariate statistics in perialpine Slovenia. *Geomorphology* 74, No. 1-4, 17-28.
- [5] Clerici, A., Perego, S., Tellini, C. and Vescovi, P. (2002). A procedure for landslide susceptibility zonation by the conditional analysis method. *Geomorphology* 48, No. 4, 349-364.
- [6] Donga, J.J., Tunga, Y.H., Chenb, C.C., Liaoc, J.J. and Panc, Y.Z. (2009). Discriminant analysis of the geomorphic characteristics and stability of landslide dams. *Geomorphology* 110, No. 3-4, 162-171.
- [7] Nefeslioglu, H.A., Gokceoglu, C. and Sonmez, H. (2008). An assessment on the use of logistic regression and artificial neural networks with different sampling strategies for the preparation of landslide susceptibility maps. *Engineering Geology* 97, No. 3-4, 171-191.
- [8] Kanungo, D.P., Arora, M.K., Sarkar, S. and Gupta, R.P. (2006). A comparative study of conventional, ANN black box, fuzzy and combined neural and fuzzy weighting procedures for landslide susceptibility zonation in Darjeeling Himalayas. *Engineering Geology* 85, No. 3-4, 347-366.

- [9] Yao, X., Tham, L.G. and Dai, F.C. (2008). Landslide susceptibility mapping based on support vector machine: A case study on natural slopes of Hong Kong, China. *Geomorphology* 101, No. 4, 572-582.
- [10] Saito, H., Nakayama, D. and Matsuyama, H. (2009). Comparison of landslide susceptibility based on a decision-tree model and actual landslide occurrence: The Akaishi Mountains, Japan. *Geomorphology* 109 No. 3-4, 108-121.
- [11] Yeon, Y.K., Han, J.G. and Ryi, K.H. (2010). Landslide susceptibility mapping in Injae, Korea using a decision tree. *Engineering Geology* 116 No. 3-4, 274-283.
- [12] Brenning, A. (2005). Spatial prediction models for landslide hazards: review, comparison and evaluation. *Natural Hazards and Earth System Sciences* 5, 853-862.
- [13] Yilmaz, I. (2009). Comparison of landslide susceptibility mapping methodologies for Koyulhisar, Turkey: conditional probability, logistic regression, artificial neural networks, and support vector machine. *Environmental Earth* 61, No. 4, 821-836.
- [14] Mitchell, T.M. (1997). *Machine learning*. McGraw Hill, New York.
- [15] Hall, M., Frank, E., Holmes, G., Pfahringer, B., Reutemann, P. and Witten, I.H. (2009). The WEKA Data Mining Software: An Update. *SIGKDD Explorations* 11/1, 10-18.
- [16] Burges, C.J.C. (1998). A tutorial on support vector machines for pattern recognition. *Data Mining and Knowledge Discovery* 2/1, 121-167.
- [17] Belousov, A.I., Verzakov, S.A. and Von Frese, J. (2002). Applicational aspects of support vector machines. *Journal of Chemometrics* 16, No. 8-10, 482-489.
- [18] Cristiani, N. and Shawe-Taylor, J. (2000). An Introduction to Support Vector Machines and other kernel-based learning methods. *Cambridge University Press*, Cambridge
- [19] Abe, S. (2005). Support Vector Machines for pattern classification. *Springer*, London.
- [20] Quinlan, J.R. (1993). C4.5: Programs for Machine Learning. *Morgan Kaufman*, San Mateo, CA.
- [21] Quinlan, J.R. (1986). Introduction to Decision Trees, *Machine Learning* (1), 81-106.
- [22] Frattini, P., Crosta, G., and Carrara, A. (2010). Techniques for evaluating performance of landslide susceptibility models. *Engineering Geology* 111, No. 1-4, 62-72.
- [23] Landis, J. and Koch, G.G. (1977). The measurement of observer agreement for categorical data. *Biometrics* 33, No. 1, 159-174.
- [24] Bonham-Carter, G. (1994). Geographic information system for geosciences – Modeling with GIS. *Pergamon*, New York.
- [25] Fielding, A.H. and Bell, J.F. (1997). A review of methods for the assessment of prediction errors in conservation presence/absence models. *Environmental Conservation* 24, 38-49.
- [26] Mihalić, S., Oštrić, M. and Vujnović, T. (2008). A Landslide susceptibility mapping in the Starca Basin (Croatia, Europe). *Proceedings of: 2nd European Conference of International Association for Engineering Geology*, 2008, Madrid, Spain
- [27] WP/WLI International Geotechnical Societies UNESCO Working Party on World Landslide Inventory. (1993). A suggested method for describing the activity of a landslide. *Bulletin of the International Association of Engineering Geology* 47, 53-57.
- [28] Cruden, D.M. and Varnes, D.J. (1996). Landslides Types and Processes. In: Turner A.K., Schuster, R.L. (eds) *Landslides: Investigation and Mitigation. Transportation Research Board special report* 247, 36-75.
- [29] Vrsaljko, D. (2003). Biostratigraphy of the Miocene deposits of Zumberak Mt. and Samoborsko Gorje Mts. on the base of mollusca (In Croatian). *PhD thesis*, University of Zagreb, 143 p.
- [30] Van Westen, C.J., Rengers, N. and Soeters, R. (2003). Use of geomorphological information in indirect landslide susceptibility assessment. *Natural Hazards* 30, No. 3, 399-419.
- [31] Marjanović, M., Bajat, B. Kovačević, M. (2009). Landslide Susceptibility Assessment with Machine Learning Algorithms. *Proceedings of: Intelligent Networking and Collaborative Systems*, 2009. INCOS '09, Barcelona, Spain, 273-278.
- [32] Marjanović, M., Kovačević, M., Bajat, B. and Voženílek, V. (2011). Landslide susceptibility assessment using SVM machine learning algorithm. *Engineering Geology* 123, No. 3, 225-234

STABILNOST POVRŠINE IZKOPA PLITVIH GRAD- BENIH IN RUDARSKIH PREDOROV

PIERPAOLO ORESTE

o avtorju

Pierpaolo Oreste
Politecnico di Torino,
Department of Land, Environment and Geotechnology Engineering
Torino, Italija
E-pošta: pierpaolo.oreste@polito.it

izvleček

Stabilnost površine izkopa plitvih predorov, ki so bili izkopani na problematičnih tleh, je danes relevanten problem na področju gradnje tunelov in rudarstva. Čeprav je ojačitev s palicami iz steklenih vlaken učinkovita, še vedno ni zanesljivih analiz in obsežnih metod. V tem prispevku je prikazan nov računski postopek, ki analizira statične pogoje površine v plitvih predorih, tudi če so ojačani s steklenimi vlakni. Postopek temelji na omejeni ravnotežni metodi, uporabljeni na zemljišču pod površino. Najpomembnejši rezultat izračuna je, da lahko varnostni faktor izkopavanja površine izračunamo tudi, če je predor ojačan, iz česar potem lahko nadaljujemo z dimenzioniranjem posega. P. Oreste je izvedel postopek na dveh primerih in je dosegel zadovoljujoče rezultate.

ključne besede

palice iz steklenih vlaken, ojačitev površine, površinski predor, omejena ravnotežna metoda, varnostni faktor

THE STABILITY OF THE EXCAVATION FACE OF SHALLOW CIVIL AND MINING TUNNELS

PIERPAOLO ORESTE

about the author

Pierpaolo Oreste
Politecnico di Torino,
Dep. of Land, Environment and Geotechnology Engineering
Torino, Italy
E-mail: pierpaolo.oreste@polito.it

abstract

The stability of the excavation face of shallow tunnels excavated in difficult ground conditions is currently a relevant problem in the sector for tunnelling and mining. Even though face-reinforcement interventions with fibreglass dowels have proved to be efficient, there is still no reliable analysis and dimensioning method available. A new calculation procedure is illustrated in this paper for the analysis of the face static condition in shallow tunnels, also when reinforcement interventions with fibreglass dowels are used. The procedure is based on the limit-equilibrium method applied to the ground core ahead of the face. The main result of the calculation is that the safety factor of the excavation face is also obtained in the presence of reinforcements and from this it is then possible to proceed with the dimensioning of the intervention. The procedure has been applied to two real cases and satisfactory results have been obtained.

keywords

fibreglass dowels, face reinforcement, surface tunnel, limit equilibrium method, factor of safety

1 INTRODUCTION

Full-face excavation in tunnels, even in poor grounds, is currently being used increasingly often and when used advantage is taken of the potentiality of the machines, the equipment and the large dimensioned plants to reduce the construction times, limit the costs and guarantee better safety conditions [1, 2]. An excavation face, however, can be instable for medium-large excavation sections when the ground has poor geotechnical

characteristics. In order to guarantee the stability of the excavation face, it is necessary to intervene at the excavation face with fibreglass reinforcements. They allow an increase in the stabilising forces on the core and a reduction in the destabilizing ones. These result in a very efficient intervention that can even render the excavation face stable in very difficult conditions and which is at the same time flexible (easy to change in the function of the geotechnical characteristics of the ground and of the stress conditions in the site), easy to use and reliable.

In spite of the successes that have been obtained when using fibreglass reinforcements at the excavation face, no adequate calculation instruments have yet been developed that are able to proceed quickly with the analysis of their behaviour and therefore with their dimensioning. In particular, it is currently problematic to define the number and type of reinforcements that must be used: simplified analysis methods introduce such large approximations that the results of the calculations are no longer reliable, while numerical methods, as it is necessary to use tri-dimensional ones, require very long calculation times and complex operations in order to be able to set up a model and to correctly interpret the obtained results.

This paper illustrates a new calculation procedure for the analysis and dimensioning of fibreglass reinforcements at the excavation face of surface mining and civil tunnels. This procedure is based on the limit-equilibrium method applied to the ground core ahead of the face. By evaluating the interaction between each reinforcement element and the surrounding ground in detail, it has been possible to determine the maximum static contribution that the reinforcements are able to develop.

2 STABILITY ANALYSIS OF THE EXCAVATION FACE USING THE LIMIT-EQUILIBRIUM METHOD (LEM)

The stability of an excavation face in a surface tunnel can be studied using the limit-equilibrium method (LEM),

dividing the ground ahead of the face into two portions that are considered infinitely rigid and which can present relative displacements both between each other and with respect to the remaining part of the ground (the Horn mechanism) (Figure 1). For the sake of simplicity, the face section is approximated as being rectangular; the prism opposite the face, which is free to slide, can allow the upper parallelepiped to move vertically and produce the so-called "rise" effect, which has obvious repercussions on the ground surface. Indeed, in the case of shallow tunnels, excavation-face instability can lead to the formation of a subsidence basin on the ground surface. There have been many cases in which accidents have occurred, sometimes rather serious ones, concerning existing buildings on the surface, due to the impossibility of contrasting the face-instability mechanism.

The LEM is based on the following main hypotheses:

- the potentially unstable mass is represented by one or more monoliths that are considered infinitely rigid (undeformable), inside which failure cannot occur;
- the kinematics of the block occurs due to sliding on simple surfaces known a priori as far as the shape and dimensions are concerned;
- it is a static-type analysis, in that only the possibility of the initial displacement of the ground blocks is proved and the evolution of the potential instability phenomenon is not considered in any way whatsoever;
- the possibility of 'progressive failure' occurring along the sliding surfaces is not taken into consideration.

It is evident that the LEM is based on particular simplifications of the hypothesised instability mechanisms and

therefore requires that the results should be considered in a particularly critical manner. The use of the LEM in the analysis of many instability mechanisms is, however, very common in the geotechnical and geomechanical fields, thanks to its simplicity, the intuitive nature of the approach and the possibility of evaluating the degree of stability through the safety factors.

In order to evaluate the stability condition of the face, it is necessary to define the resisting (limit equilibrium condition) and the active forces on the instable ground zone so that their ratio can be computed along the potentially feasible displacement direction. This implies a set of logical operations:

- 1) identification of the geometry of the possible unstable ground zones, varying the slope angle ϑ ;
- 2) evaluation of their geometry (vertexes, volume and areas of the unstable ground zones);
- 3) computation of the resultants of the volume and surface forces acting on the unstable zones;
- 4) evaluation of the resisting forces;
- 5) static analysis, that is, computation of the safety factor or of the force that induces the limiting equilibrium condition.

In the specific case under examination (Figure 2), block 1 (a triangular prism) is enclosed by the planes 1, 2 and 3 and by the parallel planes a and d, on which the triangular bases rest. Plane 2 represents the sliding surface. Block 2 is instead enclosed by planes 3, 4 and 5, by the parallel planes b and e, and by the ground surface.

The vertical force V that block 2 applies to block 1 is given by the weight of block 2, by the possible pressure applied to the surface and by the strength that

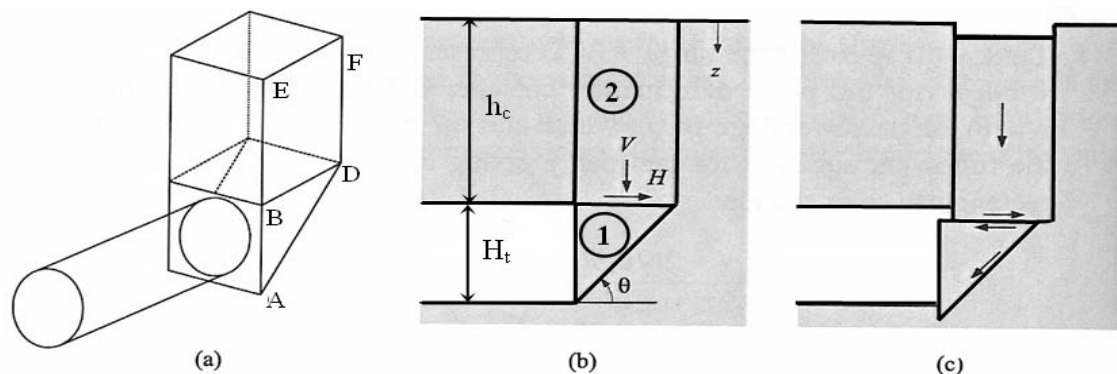


Figure 1. a) The Horn mechanism used for the analysis of the stability of the excavation face [3]; b) longitudinal section with the two blocks of ground (block 1 is prismatic and block 2 parallelepiped) under the hypothesis of failure of the face in a surface tunnel; c) admissible kinematics, for the two identified blocks, during failure of the excavation face. Key: V and H : forces that block 2 applies to block 1; ϑ : angle that is formed between the sliding surface of block 1 and the horizontal plain; z : depth from the ground surface; H_t : height of the tunnel; h_c : depth of the tunnel crown from the ground surface.

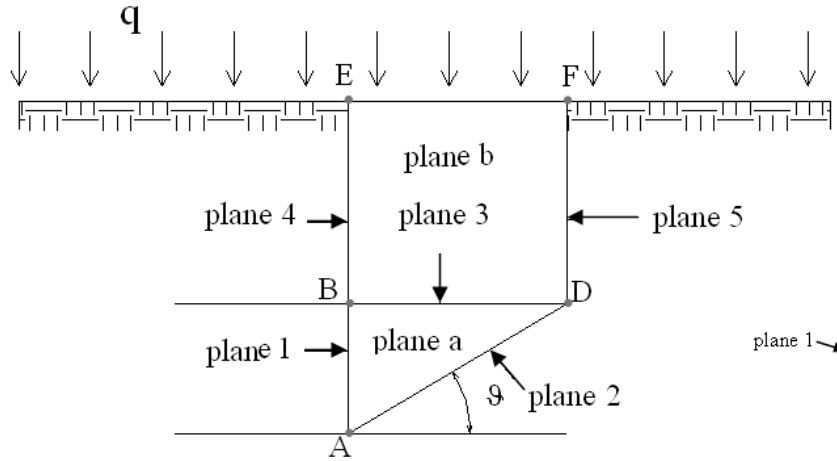


Figure 2. Longitudinal section of the zone close to the excavation face, with the scheme of the geometry adopted in the simplified analysis of the face stability.

can develop on the lateral surfaces of this block at the moment in which it tends to move downwards:

$$V = W_2 + q \cdot \left(\frac{B \cdot H_t}{\tan \vartheta} \right) - (c + \sigma'_{n,m,2} \cdot \tan \varphi) \cdot 2 \cdot \left(B + \frac{H_t}{\tan \vartheta} \right) \cdot h_c; \quad V \geq 0 \quad (1)$$

where: W_2 : the weight of block 2: $W_2 = \gamma \cdot \left(\frac{B \cdot H_t}{\tan \vartheta} \right) \cdot h_c$

- γ : the specific weight of the ground;
- q : the load applied to the ground surface;
- B and H_t : the width and height of the excavation face;
- ϑ : the inclination of plane 2 with respect to the horizontal;
- c and φ : cohesion and friction angle inside the ground, adopting the Mohr-Coulomb failure criterion;
- $\sigma'_{n,m,2}$: the mean normal effective stress on the lateral surfaces of block 2.

V is only considered when positive; if it is negative, it is made equal to 0 so as not to consider the possibility that block 1 is hanging from block 2.

The horizontal force H that block 2 applies to block 1 in correspondence to plane 3 is produced from the shear strength of the ground that can develop when a relative horizontal displacement between block 1 and block 2 occurs:

$$H = \left[V - u_3 \cdot \left(\frac{B \cdot H_t}{\tan \vartheta} \right) \right] \cdot \tan \varphi + c \cdot \left(\frac{B \cdot H_t}{\tan \vartheta} \right); \quad H \geq 0 \quad (2)$$

where:

- u_3 : the mean pore pressure of the underground water in correspondence to plane 3.

$H = 0$ is also given for $H < 0$.

Block 1, in incipient movement conditions, is also subject to two other forces, due to the shear strength of the ground, which act in the direction of the displacement vector, but in an opposite versus to it: force R_2 on the sliding surface (eq.3) and force R_a on the lateral planes a (eq.3):

$$R_2 = [(W_1 + V) \cdot \cos \vartheta + (H - X_1) \cdot \sin \vartheta - U] \cdot \tan \varphi + c \cdot \left(\frac{B \cdot H_t}{\sin \vartheta} \right); \quad R_2 \geq 0 \quad (3)$$

where:

- W_1 : the weight of block 1: $W_1 = \gamma \cdot \left(\frac{H_t^2}{2 \cdot \tan \vartheta} \right) \cdot B$
- X_1 : the horizontal filtration force in block 1, due to the movement of the underground water, if present, towards the excavation face;
- U : the hydraulic under thrust force on the sliding surface: $U = u_2 \cdot \left(\frac{B \cdot H_t}{\sin \vartheta} \right); \quad (4)$
- u_2 : mean pressure of the underground water on plane 2.

$$R_a = (c + \sigma'_{n,m,ad} \cdot \tan \varphi) \cdot 2 \cdot \left(\frac{H_t^2}{2 \cdot \tan \vartheta} \right); \quad R_a \geq 0 \quad (5)$$

where:

- $\sigma'_{n,m,ad}$: the mean normal effective stress on the lateral surfaces a of block 1.

A more detailed study of the effect of the groundwater filtration on the static of the excavation face was developed by Oreste [4].

Once the forces acting on block 1 have been determined (W_1 , V , H , R_2 , R_{ad} , and X_1), it is possible to determine the safety factor in the function of the angle ϑ :

$$F_{s,\vartheta} = \frac{R_2 + R_{ad} + H \cdot \cos \vartheta}{(W_1 + V) \cdot \sin \vartheta + X_1 \cdot \cos \vartheta} \quad (6)$$

where the forces that oppose the sliding of block 1 appear in the numerator, i.e., the forces mobilized by the ground strength on surfaces 2 (sliding surface) and on planes a, and the component H parallel to plane 2; while the forces that tend to induce sliding, i.e., the components parallel to surface 2 of the forces W_1 , V and X_1 , appear in the denominator.

As the angle ϑ of the potential sliding surface is not known a priori, the minimum value of $F_{s,\vartheta}$ is assumed for ϑ variables from 0 to 90° as the safety factor F_s :

$$F_s = \min[F_{s,\vartheta}]_{\vartheta=0 \div 90^\circ} \quad (7)$$

3 FIBREGLASS-REINFORCEMENT SYSTEM AT THE EXCAVATION FACE

The reinforcement of the ground core at the excavation face with fibreglass elements in shallow tunnels has the main purpose of increasing the ground strength; this, as a consequence, leads to the stability of both the excavation face itself and of the ground surface, even when excavating large tunnels in poor or very poor ground (Figures 3 and 4).

The technique consists of inserting sub-horizontal fibreglass dowels into the core ahead of the excavation face. These dowels are connected in a continuous way to the surrounding ground through the injection of mortar in the boreholes; they therefore act in a traction and shear dominion and have no external constraint system. The reinforcement elements are then demolished during excavation.

The use of this reinforcement system has become very common in recent years with a tendency of advancing using a full face excavation even in difficult geotechnical conditions. Fibreglass elements (generally hollow bars with an external diameter of 60 mm and a thickness of about 20 mm or filled bars of various types) are characterised by high degrees of strength and low levels of specific weight, but also by a remarkable fragility that makes it possible to carry out the excavation with traditional ground-excitation machines, without any particular problems for the tools. The fibreglass pipes are produced



Figure 3. Example of face reinforcement in a shallow tunnel using longitudinal fibreglass pipes (Avigliana Tunnel, Turin, Italy): a) view of the face during the drilling stage; b) details of the reinforcement intervention with the pipes already in place.

with thermo-hardening polyester resin, reinforced with glass fibres, whose content in weight is higher than 50 %.

The reinforcement elements are usually arranged on the excavation face in concentric circles, with a certain regularity, trying to maintain a constant density as the distance from the centre of the section changes.

The intervention is marked by a high flexibility (its characteristics can easily change during advancement without the necessity of having to change machines) and an operative simplicity. However, this intervention requires that the excavation operations should be stopped for a few days in large tunnels and in the presence of a high density of reinforcements.

The dimensioning of the intervention should be able to define the most important geometric parameters: the number, the length and the section of the elements that it is necessary to use to make the excavation face stable,

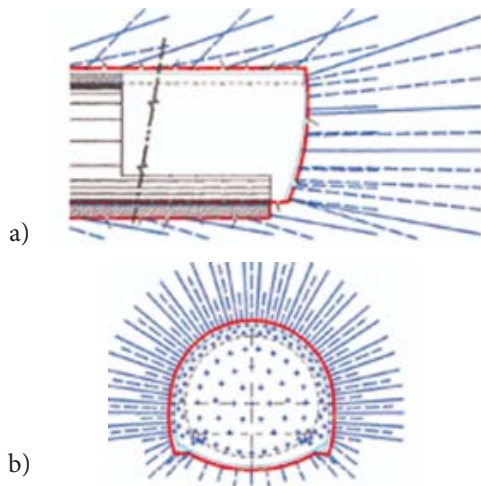


Figure 4. Typical scheme of a face-reinforcement intervention using longitudinal fibreglass elements: a) longitudinal section; b) transversal section [5]. A large number of elements, which are placed divergent from the tunnel axis, are often concentrated around the perimeter of the face to allow a crown of ground around the tunnel to be reinforced.

with an adequate safety margin. It is just as important to define the minimum residual length that the elements can have at the end of the advancement stage, before proceeding with the reinforcement of a subsequent tract.

4 SIMPLIFIED ANALYSIS METHODS TO EVALUATE THE ACTION OF REINFORCEMENTS

The reinforcement of the ground at the excavation face in surface tunnels is at present often dimensioned through simplified approaches. The number and the type of the reinforcement elements is defined in an empirical manner, in an analogous way to similar cases in which the intervention was performed successfully, or using simplified analytical formulas. Recourse to numerical calculations that are able to simulate in detail each reinforcement element and each construction stage of the tunnel is still rare outside research practice; a tri-dimensional numerical modelling with very small model elements in order to be able to precisely capture the reinforcement-ground interaction, and also the simulation of each single excavation and support stage of the tunnel are in fact required. All these aspects make an adequate numerical calculation complex and not suitable for the parametric analyses that are necessary to obtain a correct dimensioning of a reinforcement intervention.

Empirical methods are mainly based on acquired experience in the construction of structures with characteristics

similar to those of the project or on experimental models set up in the laboratory, which reproduce the phenomenon under examination, though on a reduced scale.

An application of these methods, which is very common and has been well tested for structures both in rock and in ground, is that of the use of technical classifications which, however, consider the overall stability of the void and do not generally deal with the problem of the stability of the excavation face in a specific way.

Broms and Bennermark [6], on the basis of observations of real cases and laboratory tests that consisted in extruding clayey materials through a circular hole, revealed that the stability conditions of the excavation face are guaranteed if the stability index N_f is lower than 6-7, where N_f is equal to:

$$N_f = \frac{\sigma_v - p_f}{c_u} \quad (8)$$

where:

- σ_v : the vertical stress at the depth of the centre of the excavation face;
- p_f : the pressure applied to the excavation face;
- c_u : the undrained shear strength.

Kimura and Mair [7], on the basis of centrifuge tests on clay reconsolidated in the laboratory, obtained values of the N_f index between 5 and 10 for the condition of stability of the excavation face and were able to demonstrate the marked dependence of N_f on the depth.

The reinforcement elements should therefore be able to guarantee the development of a fictitious pressure p_f (and therefore of a force S that is equal to such a pressure multiplied by the excavation face area A_f) so as to obtain an index N_f that is lower than 6-7, with a certain margin of safety.

It is also possible to obtain the horizontal force S that is necessary to apply to the excavation face to obtain the required safety factor using the LEM. Once the desired value of F_s has been decided, the force H is back calculated from equations 3, 6 and 7 (H^*). S is then derived by the difference ($H^* - H$), that is the difference between the value of H obtained from the back analysis and the value of H calculated from eq. 2.

Once the force S is known through empirical laws or using the LEM, the reinforcement elements can be simply dimensioned, hypothesising that they perform their static function only by developing an axial force on their inside (a hypothesis of flexural stiffness nil of the reinforcement system).

This hypothesis makes it possible to limit the verification of the behaviour of the reinforcement elements to the following three inequalities:

$$\frac{S}{n} \leq \sigma_{adm} \cdot A_{bar} \quad (9)$$

$$\frac{S}{n} \leq \tau_{adm} \cdot (\pi \cdot \phi_{hole} \cdot L_a) \quad (10)$$

$$\frac{S}{n} \leq \tau_{adm} \cdot (\pi \cdot \phi_{hole} \cdot L_p) \quad (11)$$

where:

- σ_{adm} : the maximum allowed traction stress in the fibreglass;
 τ_{adm} : the maximum allowed shear stress at the mortar-ground interface;
 Φ_{hole} : the diameter of the hole;
 L_a : the length of the dowel in prismatic block 1;
 L_p : the length of the dowel in the stable portion of the ground;
 n : the number of dowels foreseen at the excavation face;
 A_{bar} : section area of each single element.

It is possible to define A_{bar} , L_a , L_p and n from equations 9-11, though not in a univocal manner.

5 DETAILED ANALYSIS OF THE GROUND-DOWEL INTERACTION

In order to perform an accurate analysis of the ground-dowels interaction, a new analytical formulation is presented in the following; it is able to provide a reasonable evaluation of the behaviour of a single dowel and it also allows a quick dimensioning of the reinforcement system.

The unknown factors are the global forces (axial N , shear T and bending M stresses) that develop along the dowels and which are functions of a small dislocation displacement of the potentially unstable block.

The design of the dowels can take place through a sequence of trials, assuming different reinforcement schemes, until the safety factor of the potentially unstable block at the excavation face is higher than the minimum allowed value.

After having defined the safety factor of the excavation face in its natural state (i.e., without reinforcement), according to the criteria reported in section 2, and having verified the needs of reinforcement to increase the safety factor, the main stages of the design can be summarised as follows:

- a) definition of the chosen reinforcement scheme (number, position and dimensions of the dowels);
- b) assignment of a value to the angle ϑ ;
- c) assignment of an arbitrary displacement δ to unstable block 1 along the sliding direction; evaluation of the components of such a displacement-vector acting in the normal δ_t and axial δ_n dowel directions (Figure 5);
- d) based on δ_t and δ_n , evaluation of the shear force T , of the bending moment M , of the axial tensile force N and of the relative dowel-rock displacement v_r , induced along each dowel. In order to design the dowels and analyse the stability of the face, the values of T , N and M at the sliding surface (plan 2) (where the maximum values of the shear force and the traction axial force develop) are of particular importance;
- e) calculation of the "local" safety factors for failure of the bar and of the dowel-ground connection, for each dowel, on the basis of the values of T , N and M and of the displacements v_r evaluated in d);
- f) evaluation of the ratio η between each calculated local safety factor and the corresponding previously imposed minimum allowable value;
- g) the minimum value of η for each local safety factor and each dowel at the face, multiplied by the arbitrary displacement δ applied to the block, represents the maximum displacement δ_{max} that the unstable block can sustain before at least one of the local safety factors drops below its minimum allowable value;
- h) evaluation of the N and T forces in each single dowel at the sliding surface, for a displacement of the block equal to δ_{max} ; such forces represent the maximum contribution that each dowel can offer to the stability of the block;
- i) determination of the "global" safety factor of the unstable block 1, considering the contribution of the dowels, for the assigned value of ϑ ;
- j) repetition of steps b)-i), increasing the value of ϑ at each cycle until $\vartheta = 90^\circ$; the "global" safety factor of the unstable block is obtained at each cycle for the assigned value of ϑ ;
- k) the minimum value of the obtained global safety factors is then considered as the safety factor of the reinforced excavation face; if this value is lower or much higher than the minimum allowable value, return to point a), change the reinforcement scheme and repeat the whole procedure until the reinforcement scheme that is suitable for stabilising the face is obtained.

The detail of the proposed mathematical procedure is developed in Oreste [4]. The global safety factor $F_{s,\vartheta}$ of the unstable block 1 must now be evaluated, taking into consideration the stabilising forces produced by each dowel ($i=1 \div n$)

$$F_{s,\vartheta} = \frac{R_2 + R_{ad} + H \cdot \cos \vartheta + \left[\left(\sum_{i=1 \div n} N_{0,\delta_{max},i} \right) \cdot \cos \vartheta + \left(\sum_{i=1 \div n} T_{0,\delta_{max},i} \right) \cdot \sin \vartheta \right]}{(W_1 + V) \cdot \sin \vartheta + X_1 \cdot \cos \vartheta} \quad (12)$$

where R_2 is now given by the following expression, which substitutes eq. 3:

$$R_2 = \left[(W_1 + V - \sum_{i=1 \div n} T_{0,\delta_{max},i}) \cdot \cos \vartheta + \left(H - X_1 + \sum_{i=1 \div n} N_{0,\delta_{max},i} \right) \cdot \sin \vartheta - U \right] \cdot \tan \varphi + c \cdot \left(\frac{B \cdot H_t}{\sin \vartheta} \right); R_2 \geq 0 \quad (13)$$

where $N_{0,\delta_{max}}$ and $T_{0,\delta_{max}}$ are the axial force and shear force in the dowel at the dowel-sliding surface intersection when $\delta = \delta_{max}$.

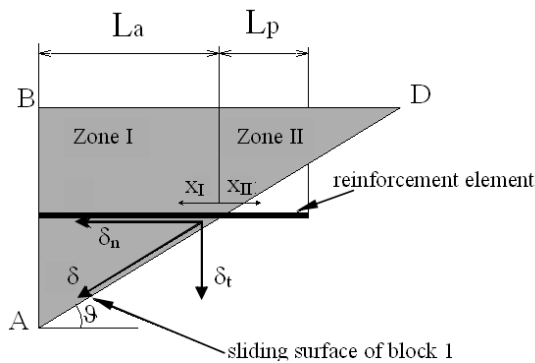


Figure 5. Breakdown of the displacement δ imposed on block 1. Key: δ displacement of block 1 along the sliding direction; δ_n and δ_t components of the displacement in the axial and normal directions of the dowel; L_a length of the dowel in the ground block 1 (zone I); L_p length of the remaining part of the dowel in the stable ground (zone II); x axial coordinate; ϑ : angle between the sliding direction and the horizontal plane; A, B, and D vertices of ground block 1.

The presence of the dowels obviously induces an increase in the safety-factor value in relation to the characteristics of the chosen reinforcement system.

The calculations developed in steps b)-i) are repeated for different values of ϑ , increasing it at each cycle, for example by 5° , until $\vartheta=90^\circ$ is reached; at each cycle the “global” safety factor of the unstable block 1 is obtained for the assigned value of ϑ . The safety factor of the reinforced excavation face is therefore the minimum value of the obtained $F_{s,\vartheta}$.

If the increase in the safety factor of the face due to the reinforcement system is still not sufficient, or when it is considered excessive, it is necessary to modify the reinforcement scheme on the basis of the obtained results and to repeat the procedure from stage a) to stage k).

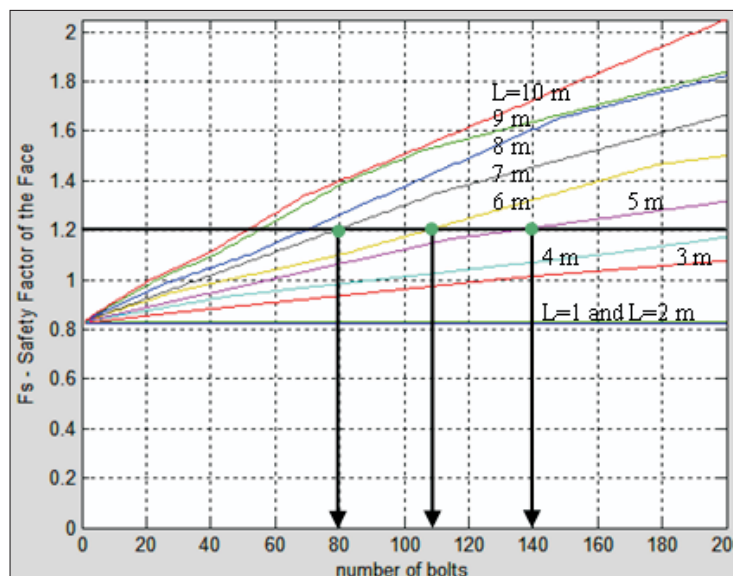


Figure 6. Example of the procedure for the determination of the number and the minimum length of the reinforcements at the face. Each line of the graph refers to a different length of the dowels at the excavation face

The dimensioning of the intervention is generally limited to a definition of the number of reinforcements and their minimal residual length. The total length of each reinforcement is subsequently identified by the maximum length that can be obtained without deviations of the hole. From the proposed procedure it is possible to obtain a summarizing graph (the results of a calculation example are shown in Figure 6) in which the safety factors of the face are reported with a variation in the number of reinforcements and their length (which should be intended as the minimum residual length).

After having fixed the desired safety factor (1.2 in the example of Figure 6), it is possible to define the necessary intervention scheme: 80 dowels with a minimum residual length of 7 m, or 110 dowels with a minimum residual length of 6 m, or even 140 dowels with a minimum residual length of 5 m. The total length of the reinforcements does not usually exceed 22 m.

Two real cases, both of which occurred in the North-West of Italy, in which failure of the excavation face occurred in sandy quartzite grounds of medium to coarse size, were studied by applying the proposed calculation method. The examined tunnels, of polycentric shape and areas of about 104 m², belong to the same zone in the Province of Biella (Italy). In both cases, loose sand formations (arkose sands) derived from the decay of the rocky granite substratum were being crossed. The reinforcement scheme at the excavation face in both cases foresaw the use of 40 injected fibreglass pipes with a total length of 14 m, 5 m of which were overlapping. The hole diameter (Φ_{hole}) was 150 mm. The tunnels were full section excavated.

In the first case a sliding of the face occurred during the excavation in correspondence to the second steel set after having realised the reinforcement phase (the residual length of the dowels at the face was therefore 12 m), when the overburden was about 10 m.

In the second case the collapse occurred when the residual length of the dowels at the face was 10 m. The overburden on the crown, at the moment of the failure, was about 5 m.

From the results obtained using the proposed calculation method it was possible to see how the safety factor of the excavation face in both cases is slightly lower than unity and this justifies the failures that occurred. These results make it possible to confirm the causes of the previously identified events (insufficient drainage system and an imperfect construction of the pre-support structure) and also to validate the proposed calculation procedure.

6 CONCLUSIONS

The problem of excavation-face stability in surface tunnels in poor ground currently represents one of the most interesting challenges in the tunnel sector. Cases in which the excavation faces collapse in spite of the fact that they have previously been reinforced with fibreglass dowels are in fact not so rare. A new calculation procedure for the analysis of reinforcement interventions using fibreglass dowels at the excavation face in surface tunnels has been illustrated in this paper. The procedure, which is based on the limit-equilibrium method applied to the ground core ahead of the excavation face, is able to evaluate, in detail, the interaction between each reinforcement element and the surrounding ground and it permits the maximum static contribution that each reinforcement element is able to give to the stability of the face to be determined.

The calculation procedure has been applied to two real cases of tunnel-face collapse in the presence of fibreglass reinforcement intervention and the results show a safety factor just below unity for both cases, which is in agreement with the events that have occurred. This has made it possible, on the one hand, to consider the presented procedure reliable, and on the other, to confirm the hypotheses initially advanced concerning the causes of the collapses.

REFERENCES

- [1] Likar J. (2004). Back analysis of time-dependent displacement at the Trojane tunnel construction. *Acta geotech. Slov.*, 1, 1, 21-36.
- [2] Likar J., Vesel G., Dervaric E. and Jeromel G. (2006). Time-dependent processes in rocks. *RMZ-mater. geoenviron.*, 53, 3, 285-301.
- [3] Anagnostou G. and Kovari K. (1996). Face Stability Conditions with Earth-Pressure-Balanced Shields. *Tunn.&Undergr. Space Techn.*, 11, 165-173.
- [4] Oreste P. (2009). Face stabilisation of shallow tunnels using fibreglass dowels. *Proceedings of ICE, Geotechnical Engineering*, 162, 2, 95-109.
- [5] Lunardi, P. (2000). The design and construction of tunnels using the approach based on the analysis of controlled deformations in rocks and soils. http://www.rocksoil.com/p_d_f/t_and_t_rocksoil_supp.pdf.
- [6] Broms B.B. and Bennermark H. (1967). Stability of Clay at Vertical Openings. *ASCE Journal of Soil Mech. and Found. Div.*, 93.

- [7] Kimura T. and Mair J.R. (1981). Centrifugal Testing of Model Tunnels in Soft Clay. 10th Int. Conf. of Soil Mech. and Found. Eng., Stockholm (Sweden).

VPLIV VROJENE SUKCIJE NA VOLUMENSKO OBNAŠANJE ZGOŠČENIH ZEMLJIN MED VLAŽENJEM

MATEJ MAČEK, BOJAN MAJES IN ANA PETKOVŠEK

o avtorjih

vodilni avtor

Matej Maček
Univerza v Ljubljani,
Fakulteta za gradbeništvo in geodezijo
Jamova 2, 1000 Ljubljana, Slovenija
E-pošta: matej.macek@fgg.uni-lj.si

Bojan Majes
Univerza v Ljubljani,
Fakulteta za gradbeništvo in geodezijo
Jamova 2, 1000 Ljubljana, Slovenija
E-pošta: bojan.majes@fgg.uni-lj.si

Ana Petkovšek
Univerza v Ljubljani,
Fakulteta za gradbeništvo in geodezijo
Jamova 2, 1000 Ljubljana, Slovenija
E-pošta: ana.petkovsek@fgg.uni-lj.si

izvleček

Vlaga zgoščenih zemljin se po vgradnji v zemeljske objekte uravnoteži z okolico. V pogojih vlažne in zmerne klime se glinene zemljine, ki so se kompaktirale na suhi strani Proctorjeve krivulje, dodatno navlažijo. Proces vlaženja spremlja zniževanje sukcije in dodatne deformacije, ki so lahko nabrekanje ali strukturni kolaps. Preiskave zemljin iz glinenih nasipov so pokazale, da se sukcija uravnoteži pri vrednostih pod ca. 300 kPa. V prispevku predstavljamo rezultate raziskav, opravljenih na zgoščenih zemljinah, v okviru katerih smo konvencionalne raziskave dopolnili z meritvami sukcije. Na izbranih vzorcih, ki smo jim določili retencijsko krivuljo, smo merili sukcijo pri različnih stopnjah zgoščenosti. Po preplavitvi smo v edometru opazovali deformacije, ki so se v odvisnosti od začetnega stanja odražale kot nabrekalni dvižki ali kolaps. S primerjavo podatkov smo ugotovili, da začetna sukcija nabitih vzorcev pomembno vpliva na značaj deformacij ob vlaženju in bi v prihodnje lahko služila kot pomemben kazalnik uporabnosti glinenih zemljin za inženirske nasipe.

ključne besede

edometrski test, sukcija, nabrekanje, kolaps

INFLUENCE OF MOULD SUCTION ON THE VOLUME-CHANGE BEHAVIOUR OF COMPACTED SOILS DURING INUNDATION

MATEJ MAČEK, BOJAN MAJES and ANA PETKOVŠEK

about the authors

corresponding author

Matej Maček
University of Ljubljana,
Faculty of Civil and Geodetic Engineering
Jamova 2, 1000 Ljubljana, Slovenia
E-mail: matej.macek@fgg.uni-lj.si

Bojan Majes
University of Ljubljana,
Faculty of Civil and Geodetic Engineering
Jamova 2, 1000 Ljubljana, Slovenia
E-mail: bojan.majes@fgg.uni-lj.si

Ana Petkovšek
University of Ljubljana,
Faculty of Civil and Geodetic Engineering
Jamova 2, 1000 Ljubljana, Slovenia
E-mail: ana.petkovsek@fgg.uni-lj.si

abstract

After construction, compacted clayey soils in different earth structures equilibrate their water content and suction with the local environment. In wet climatic conditions the compaction on the dry side of the Proctor curve, which enables a high layer stiffness during construction, may result in permanent deformation and softening during the lifetime of the structure. This paper presents the results of the tests, performed on a relatively large number of compacted test specimens, where the conventional index parameters, used to identify compacted soils, were supplemented with a suction–water-content curve and measurements of “mould” suction. Correlations were established between the optimum water content and the suction–water-content curve for representative samples, and the influence of the mould suction on the vertical deformation of the compacted samples during inundation in oedometers was studied.

keywords

oedometer tests, suction, swelling, collapse

1 INTRODUCTION

Compacted fine-grained soils have been used in the construction of roads, railroad embankments, earth embankment dams and other types of earth structures for centuries. Conventional compaction criteria have been developed empirically and are, in general, based on three parameters:

- the minimum relative compaction of the compacted layer, defined by a standard or modified Proctor test,
- the range of water content during compaction, defined by the allowable deviation from the optimum water content determined with a standard or modified Proctor test
- the required stiffness measured as the layer deformation modulus (E_{v1} , E_{v2} , E_{vd} , M_E).

The first two criteria prevent large settlements of the embankment and the last one prevents deformations by heavy vehicles. However, a large number of other factors that influence the behaviour of compacted soils are not measured or are difficult to control during compaction. Past experiences show that the highest layer stiffness is achieved when the maximum dry density is reached on the dry side of the Proctor curve. From the standpoint of a road engineer, the criteria of layer stiffness often prevail over the criteria of the required water content and many road embankments and clayey sub-grades have been compacted at water contents that are 3-10% lower than that required by the national technical recommendations [1], [2] to fulfil the criteria of the required stiffness. As a consequence, the maintenance of “dry of optimum” conditions during compaction was one of the key tasks when fine-grained soils were used as a construction material in the past. Due to wet climatic conditions (Fig. 1) the initially “dry of optimum” compacted soil wetted and the stiffness of the compacted soil was reduced.

Seasonal water-content changes in road sub-bases may seriously affect the bearing capacity, stiffness and the life time of pavements - especially on low-level roads

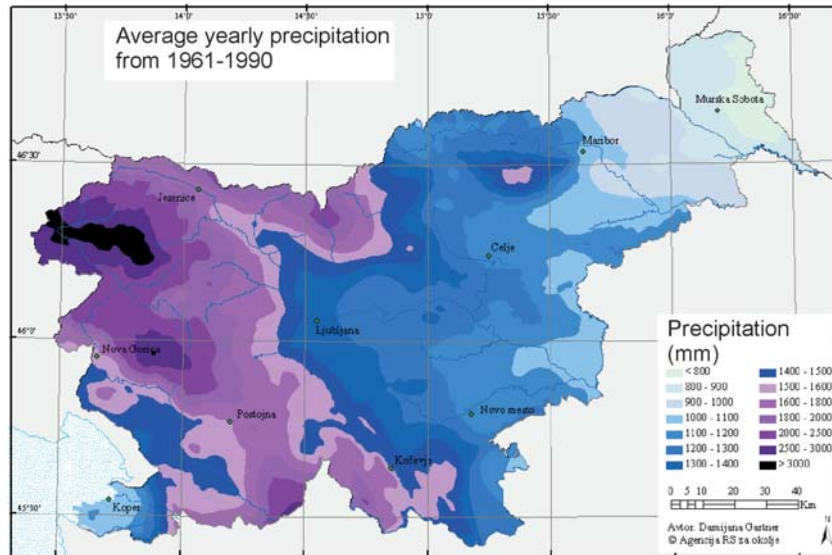


Figure 1. A map of average rainfall in Slovenia for the period 1961-1990 [3].

with thin bituminous layers. Post-construction damages recorded on pavements constructed on stiff, “too dry” sub-bases susceptible to moisture changes in poor drainage conditions are frequent [4], [5], [6]. Besides the seasonal soil-moisture changes that affect the behaviour of pavements, shallow foundations and sub-surface layers, the global environmental changes result in water content and volume changes inside the embankments and additional settlement or heave may seriously affect even very old earth structures.

Slovenia, like the whole of central Europe, has been facing significant climatic changes and extreme weather conditions in the past decade [7], [8]. The year 2003 was, for instance, exceptionally dry and hot (Fig. 2). After the autumn rain, unexpected deformations were observed on numerous Slovenian roads, embankments and slopes in deep cuttings. One of the newly constructed motorway

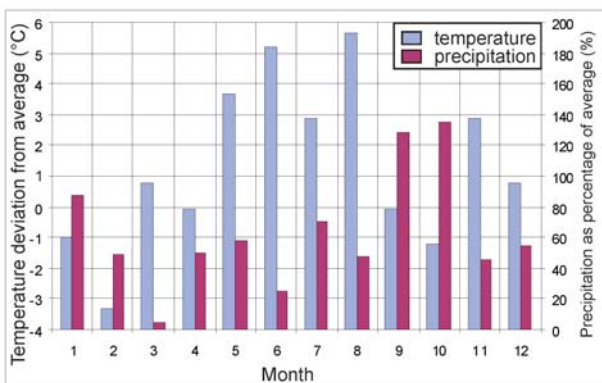


Figure 2. Temperature and precipitation conditions in Slovenia in 2003 compared with the 20-year average conditions [10].

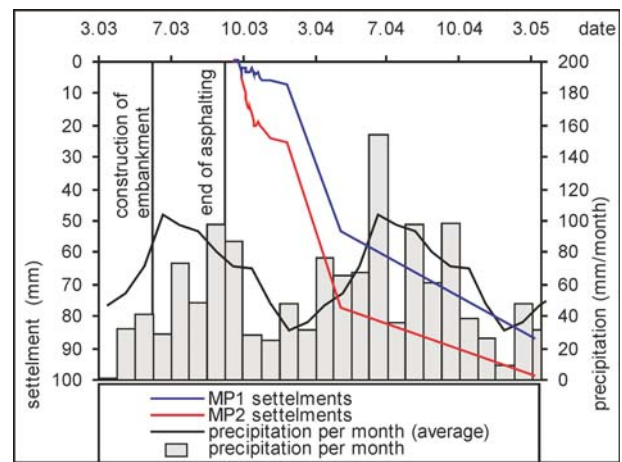


Figure 3. Deformation, measured on a motorway embankment (Eastern Slovenia), after a wet period, followed the extremely dry summer of 2003.

embankments in eastern Slovenia was so seriously damaged that in December 2003 the outermost driving lanes had to be closed to traffic (Fig. 3) [9].

A forensic investigation with deep boreholes and excavation pits, made through the pavement, showed that the soil-water content in the damaged motorway embankment increased from 2 to 12% within the 7-m-high and approximately 400-m-long embankment. The equilibration of the suction was recognized as a key driving parameter that caused the compacted soil to absorb additional water and deformation to appear. A few days after the beginning of the rain, a road heave and spreading of the slopes were observed by geodetic observation. Later on a collapse was observed. When the

deformation of the embankment stopped in May 2004, the average additional settlements exceeded 7 cm and the soil suction in the embankment equilibrated at 80 to 300 kPa, as detected in the laboratory on intact samples. The layer modulus, measured with a light falling weight plate, was reduced from $E_{vd} = 25$ MPa to less than 10 MPa.

Several elastoplastic constitutive models presently available can predict the volumetric deformations of unsaturated soils subjected to soil suction and the mean stress changes [11], [12], [13]. Due to its complex nature the Barcelona expansive model [13], [14], [15] was mainly used to predict the behaviour of natural soils or artificial sand - bentonite mixtures designed for the barriers at nuclear waste storages [16], [17], [18]. Farulla and Ferrari [19] also applied the Barcelona expansive model in a study of volume deformations in compacted soils during cyclic suction changes between 10 and 800 kPa.

In conventional earth works in Slovenia, the application of unsaturated soil mechanics still lags behind the state-of-the-art knowledge, because the implementation of the unsaturated soil mechanics is time consuming and requires expensive laboratory tests and experienced laboratory staff [20]. For the purpose of the design of conventional earth structures the volumetric deformations of compacted soils are mainly studied between the initial ("mould") and zero suction, following one of the standard procedures, either in an oedometer cell according to the ASTM standard [21] or other standards using the CBR mould [22]. This simplified approach gives the engineer an estimation of the volume changes in the embankment, or due to different compactions in the laboratory and on the worksite, the sensitivity of the embankment to volume deformations. For countries with a wet climate this approach is also valid when clayey soils with a suction of over 300 kPa are built in the embankments. Such soils equilibrate at a suction of around 30-80 kPa and only the first or first two meters are prone to seasonal suction changes [9].

When the properties and applicability of the available fill material are studied for new earth structures, the intersection of the key requirements should be found. Daniel and Benson [23], for instance, proposed such an intersection for hydraulic fills (Fig. 4).

2 THE OBJECTIVE OF THE RESEARCH

The objective of the research presented in this paper is focused on an investigation of the volume-change response of compacted clayey soils with a known mould

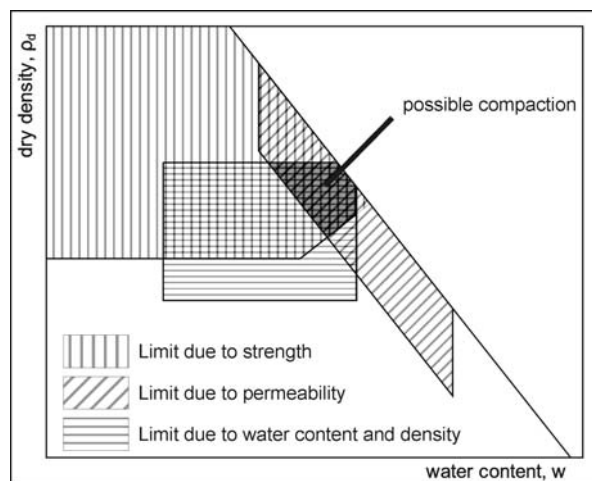


Figure 4. Intersection of acceptable shear strength, hydraulic conductivity and compaction [23].

suction, subjected to wetting in classical oedometers. The term "mould suction" used in this paper describes the suction, measured on the laboratory compacted soil. The volume-change response is discussed and interpreted in the context of the influence of the suction-water-content curve and the mould suction on the volumetric behaviour of the soil during wetting. The main goal of the research was to find out whether the data of the "single point" soil-suction measurement during compaction could be used as a tool for a better estimation of a potential risk of post-construction volumetric deformation due to seasonal or permanent wetting. The following points are examined and presented:

1. The index soil properties, used in the research program together with the initial state parameters (dry density, degree of compaction, degree of saturation)
2. The suction-water-content curve and the corresponding mould suction at different levels of compaction and water content
3. The influence of the initial mould suction on the volumetric deformation during wetting in the oedometer
4. The discussion about the acceptable range of the mould soil suction at which the compacted soils will not be prone to volumetric changes in future climatic conditions.

3 MATERIALS

Tests were carried out on three natural and two artificial soils. The artificial soils were pure calcite/stone flour (Calcivit CV, Stahovica, Slovenia) and calcium bentonite (Bentonak, Kriva Palanka, FYRM), both industrially

produced and available on the market. Calcite flour represents the inert, non-plastic and non-swelling soil, while the bentonite represents the soil with a high swelling potential. The natural soils were obtained from sites at Ljubno, where stiff marine clays of the Oligocene era appear, and from the flysch formation in the Vipava valley. From both sites, difficulties with volumetric deformations on the embankments and slopes in deep cuts have already been reported [24], [25]. The last soil is a brick clay from Renče used in the construction of a protective cover layer at the Boršt landfill. No volumetric deformations were observed on site.

The main soil properties are given in Table 1 and the suction–water-content curve is given in Fig. 5. This figure also shows the suctions, defined at the optimum water content.

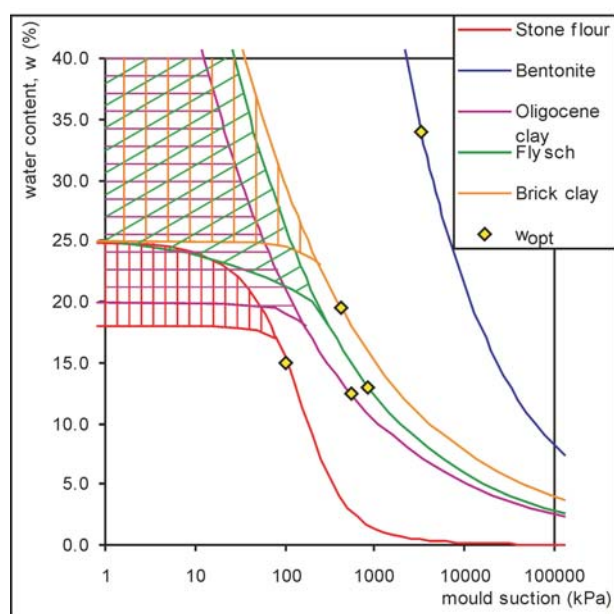


Figure 5. Suction - water content curve for tested materials and mould suction at optimum water content. Hatched areas presents suction variation due to different void ratio.

Table 1. Main properties of the soils used in the research.

material	w_L %	w_P %	I_P %	w_A %	MB_f g/kg	w_{opt} %	ρ_{dmax} t/m ³
Stone flour	23	/	/	32	2.0	14.9	1.76
Bentonite	210	35	175	297	125	33.9	1.22
Oligocene clay	40	14	26	62	38	12.5	1.83
Flysch	45	18	27	58	60	12.0	1.81
Brick clay	57	18	39	73	44	19.5	1.68

w_L is liquid limit, w_P is plastic limit, I_P is plasticity index all after CEN ISO/TS 17892-12, MB_f is methylene blue value on fines after EN 933-9, w_A is water absorption after DIN 18132, w_{opt} and ρ_{dmax} are optimal water content and maximum dry density after DIN 18127.

The suction–water-content curve was drawn from the suction measurements performed on various compacted specimens. It is important to emphasize the influence of the density, soil structure and the macro-pore distribution of each single specimen compacted with the standard Proctor effort on the measured soil suction [18], [26]. As a consequence of the structure, every single specimen lies on its own soil-water characteristic curve. However, the influence of the void ratio and the structure on the suction is much more significant at low suctions [27].

4 METHODS

The bentonite and calcite flour were industrially processed to fines passing a 63- μm sieve. The natural soils were pre-treated in the laboratory. They were firstly oven-dried at 105 ± 5 °C to a constant mass, carefully crushed with a rubber mallet and then sieved through a 2-mm sieve to eliminate the biggest particles.

In the first step samples were prepared at different water contents by mixing dry soil with different quantities of water. Samples were carefully mixed by hand and then placed in plastic bags for 24 hours to achieve uniform water-content conditions and were later compacted using a standard Proctor effort in a mould with a diameter of 10 cm [28]. After compaction, the soil suction of each compacted specimen was measured using the filter paper method [29]. A specimen was put out of a mould and cut into two pieces. A dry Whatman No. 42 filter paper was placed on the lower piece and the upper piece was placed on top of the filter paper. The specimen was put in an air-tight jar and then into a thermo-isolated chest to reduce the temperature fluctuations. After two weeks the water content of the filter paper was measured. The suction was obtained through the suction-water content for wetting of the filter paper curve. The equation for the suction-water content for wetting of the filter paper curve was used from the ASTM standard D5298 [29] for Whatman No. 42 paper. The validity of the equation was checked on KCl solutions.

Table 2. Suction measured using filter paper method and dew point potentiometer on compacted specimens.

material	suction at $w_{opt} - 2\%$ kPa	suction at w_{opt} kPa	suction at $w_{opt} + 2\%$ kPa
Stone flour	130	105	80
Bentonite	3800	3300	2900
Oligocene clay	940	540	330
Flysch	1400	860	550
Brick clay	610	420	300

Later on the suction–water-content curves were completed with suction measurements performed in a dew-point potentiometer WP4-T (Decagon devices) on soil specimens compacted at different water contents. The specimens in the dew-point potentiometer were 38 mm in diameter and 6 mm high and were much smaller than the specimens compacted in the Proctor mould. As a result of the different specimen sizes the soil structure is different too. As the mould-suction measurements after the filter paper method and the dew-point potentiometer are within the expected error, there is no significant influence of sample size. The ranges of suction, measured on the compacted soils during compaction, are given in Table 2.

In the second step, each cylinder of compacted soil was divided into three to five specimens for the oedometer test. Altogether, 52 specimens were cut out from the compacted cylinders. The tests were performed in slightly different ways than suggested by ASTM D4546 [21]. To avoid difficulties when comparing the results, both methods are described as follows:

TEST METHOD A

The cut-out specimens of compacted samples were put in the oedometer with a dry filter paper, installed on dry porous stones. A moist paper towel was put around the oedometer cell and both the towel and the oedometer cell were wrapped in a plastic foil. The specimens were first loaded with vertical stresses of 50, 100, 200 and 400 kPa and then unloaded in a reverse stress path under dry conditions. Each loading and/or unloading step was ended in 5 minutes and the final displacements were measured.

After the last unloading stage the specimens were inundated and the plastic foil and paper towel were discarded. The deformations were measured continuously until the end of the primary swelling/settlement. After that, the specimens were loaded in steps of 50, 100, 200 and 400 kPa and the deformations were observed during each loading step. At the end of the test, the specimens were unloaded again.

The swelling deformation is calculated from the void ratios during the first loading and after inundation at the same vertical stress [21].

$$\frac{\Delta h}{h_0} = \frac{(e_{v0} - e_0)}{(1 + e_0)} \quad (1)$$

where Δh is the change in the specimen height, h_0 is the specimen height before inundation, e_{v0} is the void ratio after the end of the swelling, and e_0 is void ratio before inundation.

TEST METHOD B

The specimens were prepared using the same procedure as for test method A. The main difference compared with method A was that each specimen was loaded with the selected vertical stress and the deformation under the load was measured after 5 minutes. After that the specimens were inundated and the plastic foil and paper towel were discarded. The deformations were measured continuously under a single selected load until the equilibration, and after that the specimens were unloaded.

The swelling deformation was calculated according to Equation 1.

Two major differences exist between methods A and B. In method A the free swell deformations were measured, and the swelling deformations at other vertical stresses were estimated on the same specimen during secondary loading. In method B each individual specimen was exposed to a selected vertical load and the deformations realized as swelling or collapse for the selected loads were measured.

5 TEST RESULTS AND INTERPRETATION OF THE RESULTS

The parameters determined during the tests are presented in Table 3 and Table 4.

Table 3. Results of oedometer tests, performed on compacted specimens, method A.

	w_i (%)	$\rho_{d,i}$ (t/m ³)	D_{pr} (%)	S_{ri} (%)	mould suction ¹ (kPa)	σ_v (kPa)	$\Delta h/h_0$ (kPa)
Stone flour	12.4	1.58	91	47	140	50	-1.4
						100	-1.9
						200	-2.8
						400	-3.5
	13.0	1.60	92	51	130	50	-0.1
						100	-0.4
						200	-0.8
						400	-1.3
	15.5	1.64	94	64	100	50	-0.3
						100	-0.2
						200	-0.3
						400	-0.4
21.7	1.66	95	92	0	50	n.p. ²	
					100	n.p.	
					200	n.p.	
					400	n.p.	
Oligocene clay	13.4	1.74	95	63	430	50	3.0
						100	1.7
						200	0.1
						400	-2.2
	17.4	1.78	97	88	190	50	-0.2
						100	-0.5
						200	-0.6
						400	-0.5
	22.9	1.68	92	99	80	50	n.p.
						100	n.p.
						200	n.p.
						400	n.p.
Flysch	7.0	1.51	84	23	5700	50	2.1
						100	-1.3
						200	-4.8
						400	-8.7
	10.1	1.63	90	40	1900	50	5.2
						100	2.4
						200	-0.6
						400	-4.3
	14.3	1.68	93	62	640	50	5.5
						100	3.2
						200	0.9
						400	-1.9
18.8	1.69	93	82	270	50	3.3	
					100	1.9	
					200	0.6	
					400	-1.0	
Brick clay	17.5	1.70	101	79	600	50	7.3
						100	5.2
						200	2.6
						400	0.1
	17.7	1.61	96	69	590	50	4.3
						100	1.4
						200	-1.5
						400	-3.8
	21.1	1.67	99	90	320	50	2.3
						100	2.4
						200	0.9
						400	-0.3
21.6	1.65	98	90	300	50	5.2	
					100	4.9	
					200	2.8	
					400	1.1	
29.9	1.45	87	93	140	50	n.p.	
					100	n.p.	
					200	n.p.	
					400	n.p.	

¹ the values of mould suction are obtained from suction – water content curve² n.p. – not possible to determined, deformations are too small or influence of primary loading is too big

Table 4. Results of oedometer tests, performed on compacted specimens, method B.

	specimen	w_i (%)	ρ_{di} (t/m ³)	D_{pr} (%)	S_{ri} (%)	mould suction ¹ (kPa)	σ_v (kPa)	$\Delta h/h_0$ (%)
Stone flour	A	11.4	1.62	92	45	160	50	-0.5
	A	10.4	1.56	89	38	160	100	-2.8
	A	11.7	1.57	90	44	160	200	-2.7
	B	13.6	1.62	92	54	120	50	-0.2
	B	13.0	1.61	92	51	130	100	-0.3
	B	13.1	1.60	92	51	130	200	-0.4
	C	15.9	1.66	95	67	94	50	-0.2
	C	16.0	1.67	96	69	94	100	-0.3
	C	15.8	1.68	96	69	94	200	-0.2
	D	18.0	1.69	97	80	0.1	50	0.0
	D	19.1	1.68	96	83	0.1	100	0.0
	D	22.2	1.62	93	89	0.1	200	0.0
	Bentonite	A	39.4	1.28	105	99	2300	200
A		38.6	1.25	103	93	2400	400	7.2
A		38.0	1.27	104	95	2500	800	2.6
A		42.0	1.19	97	92	2000	1200	1.0
Oligocene clay	A	11.5	1.83	100	62	710	50	1.7
	A	11.4	1.82	99	62	710	200	0.4
	A	11.4	1.73	94	53	710	500	-3.0
	B	16.2	1.82	99	87	230	50	0.2
	B	15.9	1.86	102	91	250	200	0.0
	B	16.2	1.87	102	94	230	500	-0.1
	C	20.8	1.71	93	94	110	50	0.0
	C	20.7	1.71	94	94	110	100	0.0
	C	20.7	1.69	92	90	110	200	-0.1
	Flysch	A	4.7	1.66	92	20	19000	50
A		4.1	1.70	94	18	30000	200	-4.3
A		4.5	1.67	92	19	22000	256	-8.3
B		7.0	1.79	99	36	5700	50	2.4
B		7.2	1.76	97	35	5200	200	-2.5
B		7.2	1.78	98	36	5300	500	-4.3
C		11.8	1.86	103	68	1200	50	1.9
C		11.9	1.86	103	69	1100	200	0.1
C		11.6	1.89	104	70	1200	500	-0.1
D		17.0	1.80	100	89	380	100	0.9
D		16.2	1.76	97	79	440	200	-2.5
D		17.0	1.81	100	90	380	500	-0.2
E		21.0	1.71	94	95	200	50	0.8
E		21.6	1.70	94	96	180	100	0.3
E		21.0	1.70	94	94	200	200	0.0

¹ the values of mould suction are obtained from suction – water content curve

5.1 VERTICAL HETEROGENEITY OF THE COMPACTED SPECIMEN

One very important finding derived from the results, presented in Table 4, is that the scatter of the mould-water content ($\pm 1.5\%$) and the mould dry density (± 0.06 t/m³) inside a single Proctor compacted specimen were immense. Fleureau et al. [30] also reported the vertical heterogeneity of a compacted soil. However, the scatter in their results was much lower than registered in this paper.

5.2 MOULD WATER CONTENT (SUCTION) AND ITS IMPORTANCE FOR VOLUMETRIC BEHAVIOUR

Fig. 6 shows the results of the deformation behaviour recorded in the oedometer tests on Flysch specimens performed after method B. The first graph (Fig. 6a) presents the relationship between the void ratio and the vertical stress at a mould-water content of 7.2% (specimen B), while the second graph (Fig. 6b) corresponds

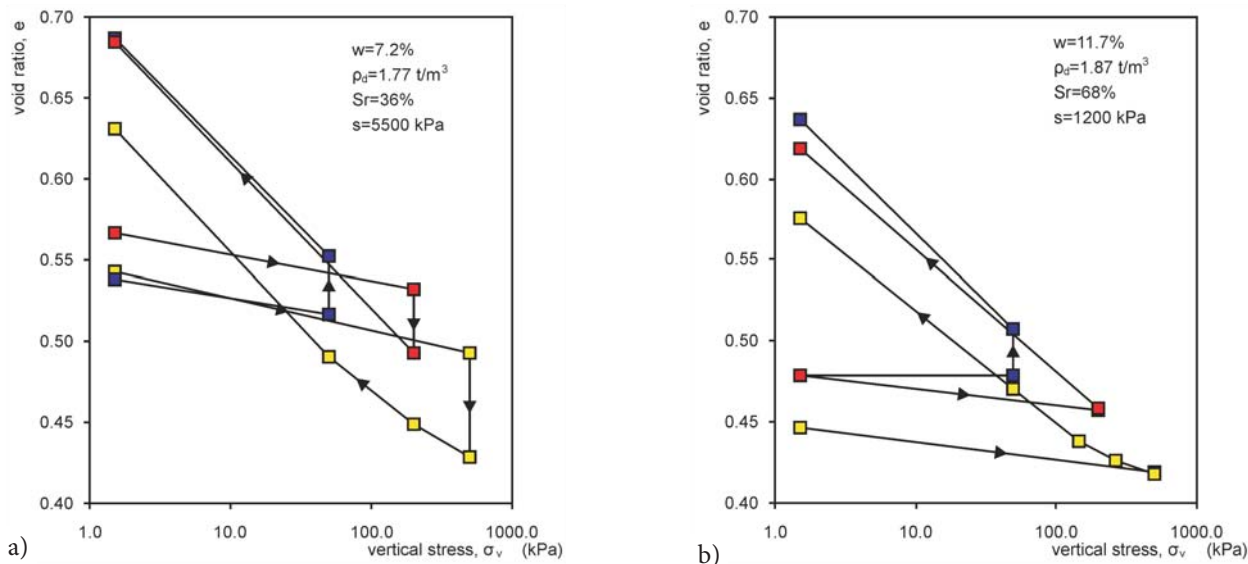


Figure 6. Deformation of compacted flysch. Loading path is marked by arrows.

to the specimen with a 11.8% water content (specimen C). Swelling deformations were observed for both specimens inundated at 50 kPa. However, a significant collapse was detected at a vertical load of 200 and 500 kPa only for the dryer specimen (Fig. 6a). Fig. 7 shows the influence of the mould-water content on the deformation behaviour at different vertical loads. From the measured values it could be concluded that specimens compacted on the dry side of the Proctor curve are much more sensitive to volumetric changes during wetting.

5.3 INTERSECTION OF MOULD-WATER CONTENT, DRY DENSITY, SUCTION AND DEFORMATION

Following the idea of Daniel and Benson [23], the Proctor curve, the suction–water-content curve and the deformation measured for different vertical loads in the oedometer, are presented in the same diagrams (Fig. 8). The black rectangles represent the area of the common requirements for the compaction given in the Slovenian specifications for earth works on roads [2].

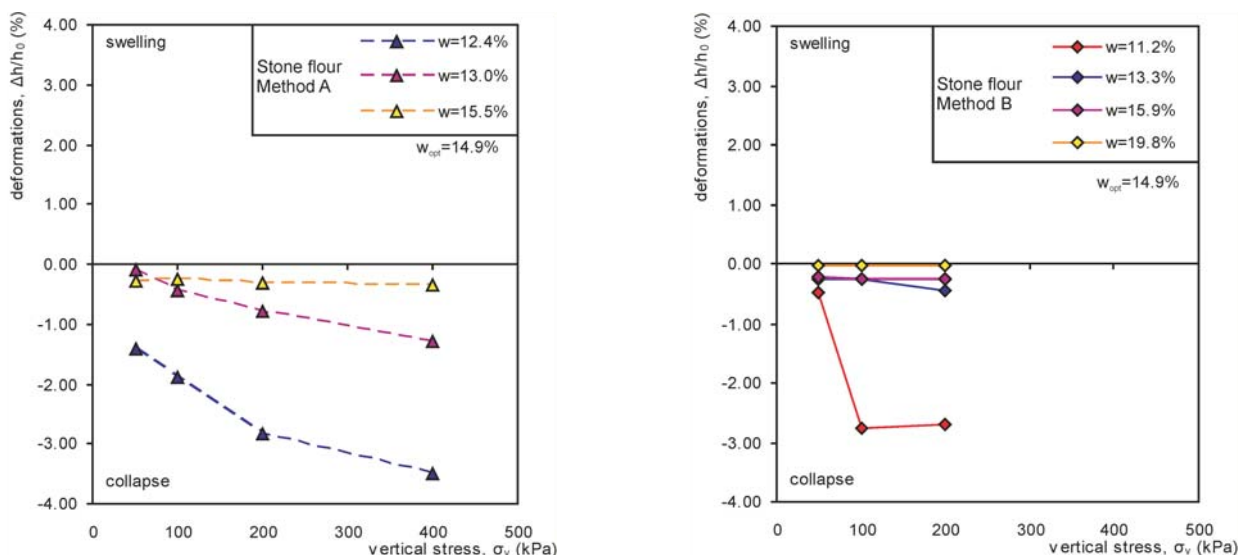
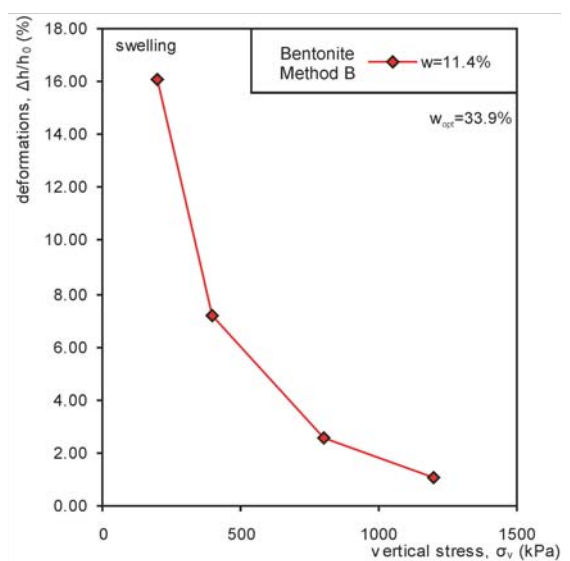
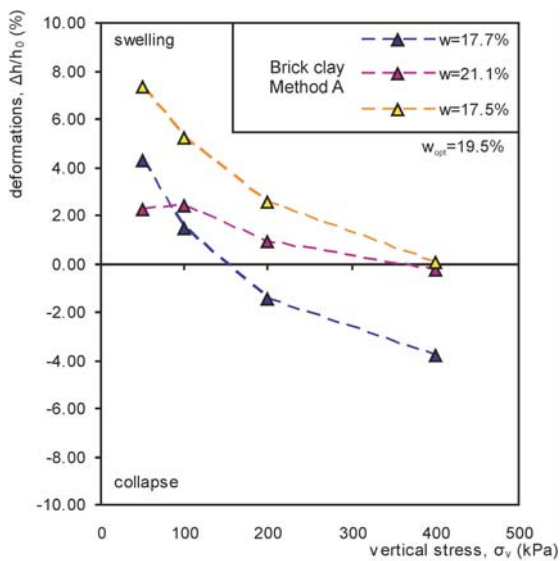
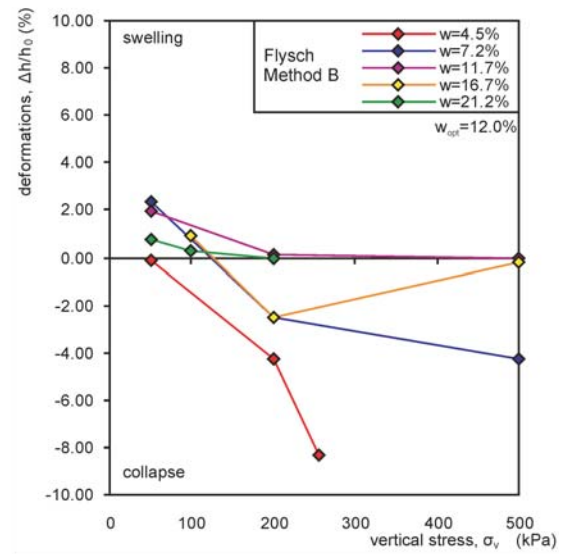
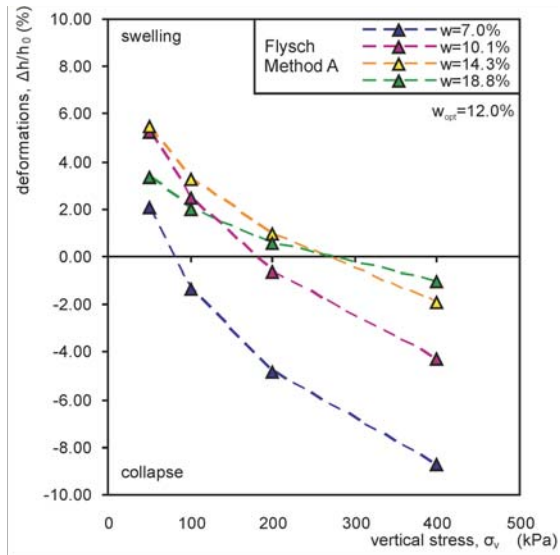
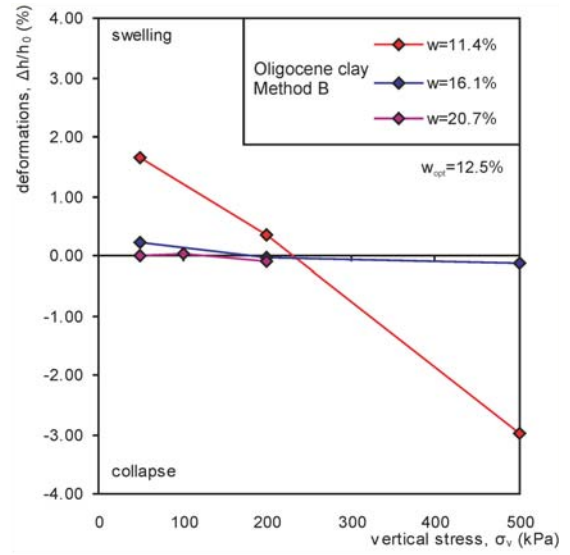
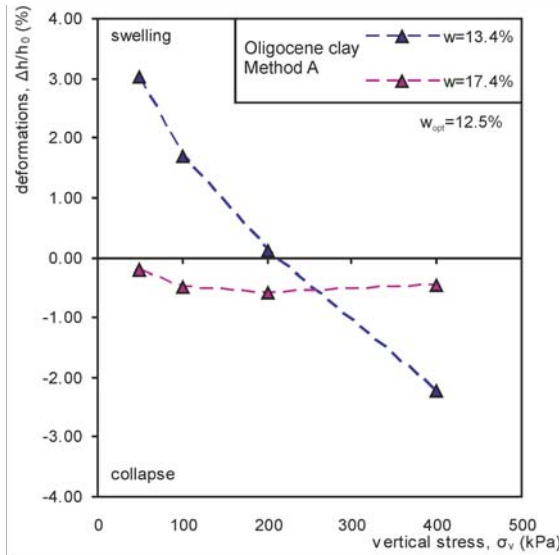


Figure 7. Influence of mould water content on the deformation behaviour of compacted specimens (continued on opposite page).



The coloured areas indicate three classes divided on the basis of absolute deformations measured after inundation in the oedometers. The first class (green) belongs to the specimens that exhibited deformations lower than 2%, the second class (blue) belongs to the specimens with deformations between 2 and 4% and the third class (red) indicates specimens with deformations higher than 4%. The hatched red area also represents the area of suction where the suction-water content relationship is significantly influenced by the specimen structure. Even more interesting is the graph given in Fig. 9. For a mould suction lower than 250 kPa the compacted specimens exhibited negligible heave or collapse after inundation. For the mould suction of 250–600 kPa, deformation due to heave or collapse can reach up to 4%. For mould suctions higher than 1500 kPa, the compacted specimens did not fulfill the required minimum degree of compaction and the expected deformations were higher than 6%.

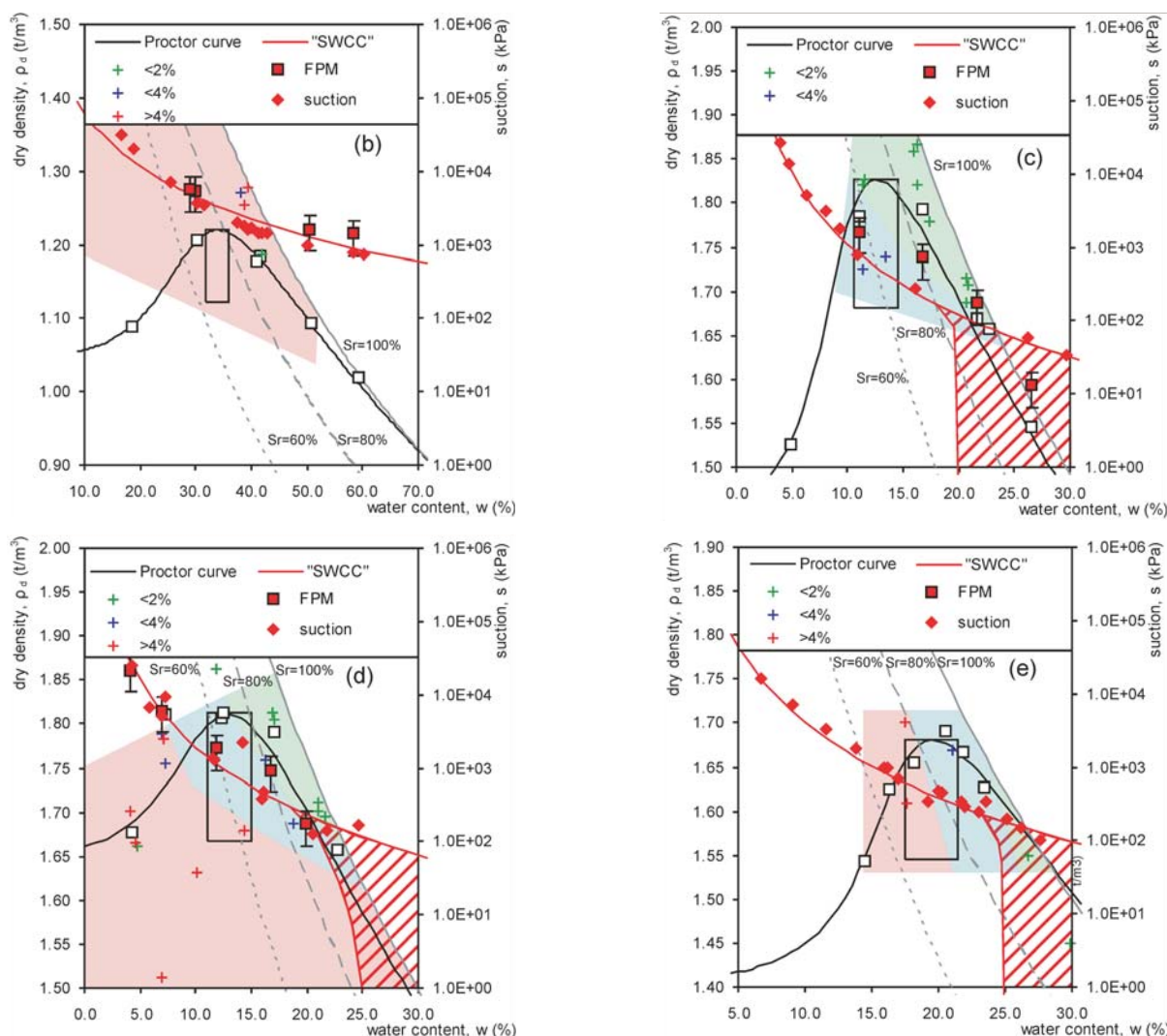


Figure 8. Comparison of Proctor curve and the suction - water content curve for tested soils with the information about the range of deformations, measured in oedometers (a) stone flour, (b) bentonite, (c) Oligocene clay, (d) flysch and (e) brick clay; FPM – suction measured by filter paper method, suction – suction measured by dew point potentiometer.

As was expected, the properly compacted stone flour exhibited negligible deformation after inundation. The mould soil suction was lower than 120 kPa. However, specimens compacted at too low a degree of compaction (less than 92% of the relative compaction) exhibited some settlements, which is a well-known phenomenon. The mould suction of bentonite at the optimum water content was between 2900 and 3800 kPa. Due to the high suction the compacted specimens of bentonite exhibited very large swelling deformations, even under a high vertical load. In Fig. 8 we already marked the range of the optimum water content for different soils. We can conclude that the “mould” suction at the optimum water content increases with the increasing plasticity of the soil and can be used as an important parameter when the volumetric behaviour of compacted soils is considered.

When studying the results of real soils, special attention should be paid to the behaviour of flysch material. Highly over-consolidated stiff clay from Flysch formation can also be treated as a soft, clay bearing bedrock. Although the index parameters given in Table 1 did not indicate any significant differences between the Oligocene clay and the flysch, the deformation behaviour of the flysch is much more unfavourable from the engineering point of view. One of the possible and reasonable explanations is that the time of 24 hours was not long enough to ensure a homogenous water-content distribution throughout the sample and that the single grains of flysch remained drier than the average soil mixture during compaction.

6 DISCUSSION

The relationship between the optimum water content, the liquid limit and the mould suction at the optimum water content is given in Fig.10 for the investigated soils and compiled with the data from Fleureau et al. [30]. From Fig. 10 it could be observed that the samples with a higher optimum water content tend to have a higher liquid limit and a higher mould suction. These results complement the results presented in Figures 8 and 9.

The swelling behaviour of the compacted soils could be evaluated using different methods, following local experiences and national guidelines. The fines content, the liquid limit, the plasticity index and the methylene blue value are some of the most indicative parameters that offer a first insight into the soil's volumetric characteristics for engineers in practice [31], [32]. The liquid limit, the plasticity index, the methylene blue value only evaluate the tendency of the soil to undergo large swelling deformations. Mould suction, on the other hand, evaluates the tendency of the soil to undergo large volume deformations for a given test specimen and range of water content with a low tendency to large volume deformations could be observed. From the results presented in this study it can be concluded that with measurements of mould suction (Fig. 9), the index properties could be excellently complemented for the evaluation of the behaviour of compacted soils.

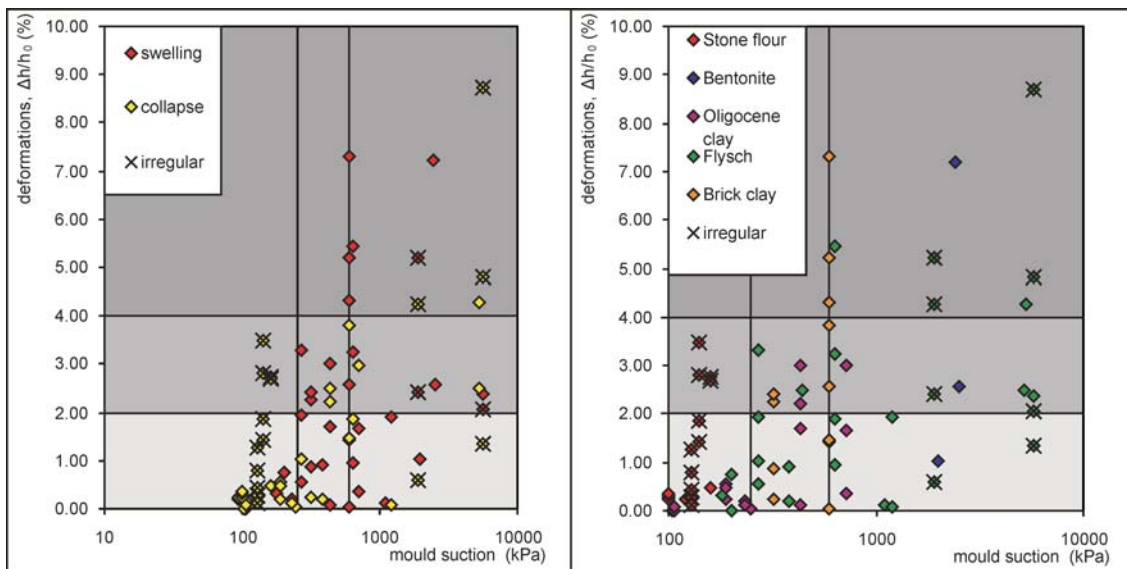


Figure 9. Evolution of vertical deformations (heave and collapse) after inundation at different suctions (left) and the evolution of absolute vertical deformations for different compacted samples (right). “Irregular” specimens have a degree of compaction less than 92% of the maximum Proctor dry density.

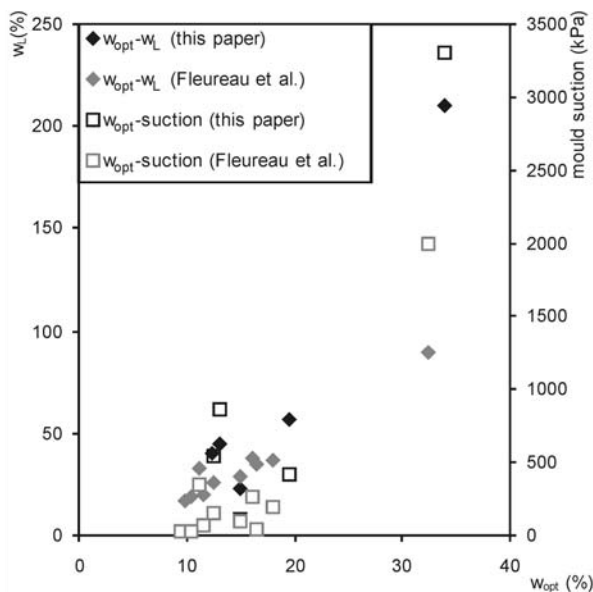


Figure 10. Relationship between the optimum water content, the liquid limit and the mould suction at optimum water content for the investigated material and compiled with the data from Fleureau et al. [30].

7 CONCLUSIONS

The aim of this paper was to give a simplified overview of the volumetric behaviour of compacted clayey soils during wetting. Soil wetting is common in countries with wet climates, like Slovenia, when soil with high suction is used for embankment construction and exposed to weather. For a study of the volumetric behaviour, conventional geotechnical laboratory tests were combined with soil-suction measurements, using the simplest and very basic laboratory tests, which could be used in a commercial laboratory.

The mould-soil suction was recognized as an important factor that can indicate the volumetric behaviour of a compacted soil at very early stages of a preliminary investigation. It was found that the most simple and low-cost soil-suction measuring devices, like the filter paper method and the dew-point potentiometer, offer a new alternative to conventional practice in the field of earthworks. The main finding was that the soil that exhibits high mould suction after compaction will exhibit higher deformation during wetting. High mould suctions can also indicate compaction or a non-uniform arrangement of water and density in the soil. The field measurements of suction in three old Slovenian motorway embankments, which suffered from unpredicted deformation, proved that the soil suction in the real clay embankment equilibrated at values lower than 300 kPa, regardless

of the suction at which the soil was compacted during construction [9].

The authors of this paper are aware that the described simple approach cannot compete with fundamental researches, performed using the most advanced laboratory equipment. The scatter of the results presented in the study is significant. However, it is important to stress that compacted soils are the most widely used construction material and the Proctor compaction test is still the most widely used reference test to control the quality of compaction. The deficiencies of the Proctor test are well known, but at the moment there is no better test. The heterogeneity of the densities and the water contents, the differences in microstructure and macrostructure of the compaction layers do exist in the field and the earth structure will deform or fail when the most vulnerable part of the structure fails.

The results, gathered from five different soil samples and 52 specimens, compacted at different dry densities and water contents, show that the mould soil suction measurement can complement the conventional geotechnical tests and they can be used as a good tool during the preliminary as well as the quality-assurance and quality-control tests. A lot of additional investigations will have to be made before the recommendations about the allowable value of the mould suction are prepared for use in different local geo-environments. However, the results indicate that for conventional earth structures, the mould suction of the compacted soil should not exceed 600 kPa in wet climate conditions.

REFERENCES

- [1] ZTVE (1997). *Zusätzliche Technische Vertragsbedingungen und Richtlinien für Erdarbeiten im Straßenbau (Supplementary Technical Terms and Conditions of Contract and Guidelines for Earthworks in Road Construction)* ZTVE-StB94. FGSV Verlag, Cologne.
- [2] PTP. (1989). *Posebni tehnični pogoji za zemeljska dela na cestah (Special Technical Conditions for earth works on roads)*. SCS Ljubljana, Slovenia.
- [3] <http://www.arso.gov.si/vreme/podnebje/karte/karta4028.html>. Accessed 7 July 2011.
- [4] Petkovšek, A., Pavšič, P., Kokot, D. and Leben, B. (2006). Using dielectric measurements to predict seasonal water movement in unbound road base and sub-grade layers. *Proceedings of the XIIIth Danube-European Conference on Geotechnical Engineering*, Ljubljana, Slovenia, 29-31 May 2006.

- [5] Zapata, C. E., Andrei, D., Witczak, M. W. and Houston, W. N. (2005). Incorporation of environmental effects in pavement design. *International Workshop on Water in Pavements-WIP 2005*. Madrid, Spain. 27 October 2005.
- [6] Chen, D. H. and Scullion, T. (2008). Forensic Investigations of Roadway Pavement Failures. *Journal of Performance of Constructed Facilities* 22 No. 1, 35-44
- [7] Corti, T., Muccione, V., Köllner-Heck, P., Bresch, D. and Senevirate, S. I. (2009). Simulating past droughts and associated building damages in France. *Hydrol. earth syst. sci. (Göttingen, Nemčija)* 13, 1739-1747.
- [8] Petkovšek, A., Fazarinc, R., Kočevar, M., Maček, M., Majes, B. and Mikoš, M. (2011). The Stogovce landslide in SW Slovenia triggered during the September 2010 extreme rainfall event. *Landslides*. [in press].
- [9] Maček, M., Bebar and M., Petkovšek, A. (2010) High embankments from highly plastic, stiff clays in North-East Slovenia. *Proceedings of the XIIIth Danube-European Conference on Geotechnical Engineering*, Bratislava, Slovak Republic, 2-4 June 2010.
- [10] Cegnar, T. (2004). Podnebne razmere v letih 2002 in 2003 (Climate in the Years 2002 and 2003). *Ujma* 17/18, 16-31.
- [11] Alonso, E.E., Gens, A. and Josa, A. (1990). A constitutive model for partially saturated soils. *Geotechnique* 40 No. 3, 405- 430.
- [12] Fredlund, D.G. and Rahardjo, H., (1993). *Soils Mechanics for Unsaturated Soils*. John Wiley and Sons, New York.
- [13] Gens, A. and Alonso, E.E., (1992). A framework for the behaviour of unsaturated expansive clays. *Can. Geotech. J.* 29, 1013- 1032.
- [14] Alonso, E.E., Vaunat, J. and Gens, A., (1999). Modelling the mechanical behaviour of expansive clays. *Eng. Geol.* 54, 173-183.
- [15] Alonso, E.E., Romero, E., Hoffmann, C. and Garcia-Escudero, E. (2005). Expansive bentonite-sand mixtures in cyclic controlled-suction drying and wetting. *Engineering Geology* 81. 213-226.
- [16] Bernier, F., Volckaert, G., Alonso, E.E. and Villar, M., (1997). Suction controlled experiments on Boom clay. *Eng. Geol.* 47, 325- 338.
- [17] Cuisinier, O. and Masrouri F. (2005). Hydromechanical behaviour of a compacted swelling soil over a wide suction range. *Eng. Geol.* 81, 204- 212.
- [18] Nowamooz, H. and Masrouri, F. (2009). Density-dependent hydromechanical behaviour of a compacted expansive soil. *Eng. Geol.* 106, 105-115.
- [19] Farulla, C. A. and Ferrari, A. (2007). Mechanical Behaviour of Compacted Scaly Clay During Cyclic Controlled-Suction Testing. *Experimental Unsaturated Soil Mechanics*. Springer.
- [20] Chin, K., Leong, E., and Rahardjo, H. (2010). A simplified method to estimate the soil-water characteristic curve. *Canadian Geotechnical Journal* 47. No. 12, 1382-1400.
- [21] ASTM. (2003). *One-dimensional swell or settlement potential of cohesive soils (D 4546 - 03)*.
- [22] SIST. (2006). *Hidravlično vezane zmesi - Specifikacije - 11. del: Izboljšanje zemljin z apnom (Hydraulically bound mixtures - Specifications - Part 11: Soil treated by lime) (SIST EN 14227-11:2006)*.
- [23] Daniel, D. E. and Benson, C.H. (1991). Water content-density criteria for compacted soil liners. *Journal of Geotechnical Engineering* 116, No. 12, 1811-1830.
- [24] Šuklje, L. (1980). Earth pressures on the underground power station Moste. *Gradbeni vestnik* 29, 201- 212.
- [25] Petkovšek, A. and Majes, B. (2001). Izkušnje z geotehničnimi problemi pri gradnji avtocestnega omrežja: je bila odločitev o gradnji visokih nasipov iz fliša na HC Selo - Šempeter pravilna?. 2. Šukljetovi dnevi Zbornik referatov. Maribor, 19 October 2001.
- [26] Nuth, M. and Laloui, L. (2008). Advances in modelling hysteretic water retention curve in deformable soils. *Computers and Geotechnics* 35, 835-844.
- [27] Kawai, K., Karube, D. and Kato, S. (2000). The model of water retention curve considering effects of void ratio. *Proc. Unsaturated soils for Asia*. Singapore, 18-19 May 2000.
- [28] DIN. (1997). *Proctorversuch (DIN 18127)*.
- [29] ASTM. (2003). *Standard test method for measurement of soil potential (suction) using filter paper (D 5298 - 03)*.
- [30] Fleureau, J.M, Verbrugge, J.C., Correia, A. G. and Kheirbek-Saoud, S. (2002). Aspects of the behaviour of compacted clayey soils on drying and wetting paths. *Can. Geotech. J.* 39, 1341-1357.
- [31] Chiappone, A., Marello, S., Scavia, C., and Setti, M. (2004). Clay mineral characterization through the methylene blue test: comparison with other experimental techniques and application of the method. *Canadian Geotechnical Journal* 41. 1168-1178.
- [32] Dapena, E. and Parrilla, A. (2009). Spanish technical regulations for road construction. *2nd International Seminar On Earthworks in Europe*. London, 3-4 June 2009.

NAVODILA AVTORJEM

VSEBINA ČLANKA

Članek naj bo napisan v naslednji obliki:

- Naslov, ki primerno opisuje vsebino članka in ne presega 80 znakov.
- Izvleček, ki naj bo skrajšana oblika članka in naj ne presega 250 besed. Izvleček mora vsebovati osnove, jedro in cilje raziskave, uporabljeno metodologijo dela, povzetek izidov in osnovne sklepe.
- Uvod, v katerem naj bo pregled novejšega stanja in zadostne informacije za razumevanje ter pregled izidov dela, predstavljenih v članku.
- Teorija.
- Eksperimentalni del, ki naj vsebuje podatke o postavitvi preiskusa in metode, uporabljene pri pridobitvi izidov.
- Izidi, ki naj bodo jasno prikazani, po potrebi v obliki slik in preglednic.
- Razprava, v kateri naj bodo prikazane povezave in posplošitve, uporabljene za pridobitev izidov. Prikazana naj bo tudi pomembnost izidov in primerjava s poprej objavljenimi deli.
- Sklepi, v katerih naj bo prikazan en ali več sklepov, ki izhajajo iz izidov in razprave.
- Vse navedbe v besedilu morajo biti na koncu zbrane v seznamu literature.

Dodatne zahteve

- Vrstice morajo biti zaporedno oštevilčene.
- Predložen članek ne sme imeti več kot 18 strani (brez tabel, legend in literature); velikost črk 12, dvojni razmik med vrsticami. V članek je lahko vključenih največ 10 slik. Isti rezultati so lahko prikazani v tabelah ali na slikah, ne pa na oba načina.
- Potrebno je priložiti imena, naslove in elektronske naslove štirih potencialnih recenzentov članka. Urednik ima izključno pravico do odločitve, ali bo te predloge upošteval.

ENOTE IN OKRAJŠAVE

V besedilu, preglednicah in slikah uporabljajte le standardne oznache in okrajšave SI. Simbole fizikalnih veličin v besedilu pišite poševno (npr. v , T itn.). Simbole enot, ki sestojijo iz črk, pa pokončno (npr. Pa, m itn.). Vse okrajšave naj bodo, ko se prvič pojavijo, izpisane v celoti.

SLIKE

Slike morajo biti zaporedno oštevilčene in označene, v besedilu in podnaslovu, kot sl. 1, sl. 2 itn. Posnete naj bodo v kateremkoli od razširjenih formatov, npr. BMP, JPG, GIF. Za pripravo diagramov in risb priporočamo CDR format

(CorelDraw), saj so slike v njem vektorske in jih lahko pri končni obdelavi preprosto povečujemo ali pomanjšujemo.

Pri označevanju osi v diagramih, kadar je le mogoče, uporabite oznache veličin (npr. v , T itn.). V diagramih z več krivuljami mora biti vsaka krivulja označena. Pomen oznake mora biti razložen v podnapisu slike.

Za vse slike po fotografskih posnetkih je treba priložiti izvirne fotografije ali kakovostno narejen posnetek

PREGLEDNICE

Preglednice morajo biti zaporedno oštevilčene in označene, v besedilu in podnaslovu, kot preglednica 1, preglednica 2 itn. V preglednicah ne uporabljajte izpisanih imen veličin, ampak samo ustrezne simbole. K fizikalnim količinam, npr. t (pisano poševno), pripišite enote (pisano pokončno) v novo vrsto brez oklepajev.

Vse opombe naj bodo označene z uporabo dvignjene številke¹.

SEZNAM LITERATURE

navedba v besedilu

Vsaka navedba na katero se sklicujete v besedilu, mora biti v seznamu literature. Neobjavljeni rezultati in osebne komunikacije se ne priporočajo v seznamu literature, navedejo pa se lahko v besedilu.

oblika navajanja literature

V besedilu: navedbe v besedilu se nanašajo na:

- a. enega avtorja: priimek avtorja (brez začetnice, razen če ni nejasnosti) in leto objave;
- b. dva avtorja: oba priimka avtorjev in leto objave;
- c. trije ali več avtorjev: najprej priimek avtorja sledi "et al." in leto objave.

Primeri:

(Caquot, 2001a, 2001b, 2003; Caquot in Jones, 1995)...
Mulilis et al. (2006) so pred kratkim pokazali ..."

V seznamu: Literatura mora biti urejena po abecedi in če je potrebno, dodatno še kronološko. Več navedb istega avtorja v istem letu morajo biti označene s črkami "a", "b", "c", itd.

Sklicevanje na objave v revijah:

Tuller, M., Or, D., Dudley, L. M., 1999. Adsorption and capillary condensation in porous media: Liquid retention and interfacial configurations in angular pores. *Water Resources Research* 35, 1949–1964.

Sklicevanje na knjigo:

Mitchell, J.K., Soga, K., 2005. Fundamentals of Soil Behavior, third ed. John Wiley and Sons, New York.

Sklicevanje na poglavje v monografiji:

Mettam, G.R., Adams, L.B., 1999. How to prepare an electronic version of your article, in: Jones, B.S., Smith, R.Z. (Eds.), Introduction to the Electronic Age. E-Publishing Inc., New York, pp. 281–304.

Sklicevanje na spletne objave:

Kot najmanj je potrebno podati celoten URL. Če so poznani drugi podatki (DOI, imena avtorjev, datumi, sklicevanje na izvorno literaturo), se naj prav tako dodajo.

PODATKI O AVTORJIH

Članku priložite tudi podatke o avtorjih: imena, nazive, popolne poštne naslove, številke telefona in faksa, naslove elektronske pošte. Navedite kontaktno osebo.

SPREJEM ČLANKOV IN AVTORSKE PRAVICE

Uredništvo si pridržuje pravico do odločanja o sprejemu članka za objavo, strokovno oceno mednarodnih recenzentov in morebitnem predlogu za krajšanje ali izpopolnitev ter terminološke in jezikovne korekture. Z objavo preidejo avtorske pravice na revijo ACTA GEOTECHNICA SLOVENICA. Pri morebitnih kasnejših objavah mora biti AGS navedena kot vir.

Vsa nadaljnja pojasnila daje:

Uredništvo
ACTA GEOTECHNICA SLOVENICA
Univerza v Mariboru,
Fakulteta za gradbeništvo
Smetanova ulica 17, 2000 Maribor, Slovenija
E-pošta: ags@uni-mb.si

INSTRUCTIONS FOR AUTHORS**FORMAT OF THE PAPER**

The paper should have the following structure:

- A Title that adequately describes the content of the paper and should not exceed 80 characters;
- An Abstract, which should be viewed as a mini version of the paper and should not exceed 250 words. The Abstract should state the principal objectives and the scope of the investigation and the methodology employed, it should also summarise the results and state the principal conclusions;
- Immediately after the abstract, provide a maximum of 6 keywords
- An Introduction, which should provide a review of recent literature and sufficient background information to allow the results of the paper to be understood and evaluated;
- A Theoretical section;
- An Experimental section, which should provide details of the experimental set-up and the methods used for obtaining the results;
- A Results section, which should clearly and concisely present the data using figures and tables where appropriate;
- A Discussion section, which should describe the relationships shown and the generalisations made possible by the results and discuss the significance of the results, making comparisons with previously published work;

- Conclusions, which should present one or more conclusions that have been drawn from the results and subsequent discussion;
- All references mentioned in the Reference list are cited in the text, and vice versa.

Additional requirements for manuscripts

- Use double line-spacing.
- Insert continuous line numbering.
- The submitted text of Research Papers should cover no more than 18 pages (without Tables, Legends, and References, style: font size 12, double line spacing). The maximum number of illustrations should not exceed 10. Results may be shown in tables or figures but not in both of them.
- Please submit, with the manuscript, the names, addresses and e-mail addresses of 4 potential referees. Note that the editor retains the sole right to decide whether or not the suggested reviewers are used.

UNITS AND ABBREVIATIONS

Only standard SI symbols and abbreviations should be used in the text, tables and figures. Symbols for physical quantities in the text should be written in Italics (e.g. *v*, *T*, etc.). Symbols for units that consist of letters should be in plain text (e.g. Pa, m, etc.). All abbreviations should be spelt out in full on first appearance.

FIGURES

Figures must be cited in consecutive numerical order in the text and referred to in both the text and the caption as Fig. 1, Fig. 2, etc. Figures may be saved in any common format, e.g. BMP, JPG, GIF. However, the use of CDR format (CorelDraw) is recommended for graphs and line drawings, since vector images can be easily reduced or enlarged during final processing of the paper.

When labelling axes, physical quantities (e.g. v , T , etc.) should be used whenever possible. Multi-curve graphs should have individual curves marked with a symbol; the meaning of the symbol should be explained in the figure caption. Good quality black-and-white photographs or scanned images should be supplied for illustrations.

TABLES

Tables must be cited in consecutive numerical order in the text and referred to in both the text and the caption as Table 1, Table 2, etc. The use of names for quantities in tables should be avoided if possible: corresponding symbols are preferred. In addition to the physical quantity, e.g. t (in Italics), units (normal text), should be added on a new line without brackets. Any footnotes should be indicated by the use of the superscript¹.

REFERENCES

citation in text

Please ensure that every reference cited in the text is also present in the reference list (and vice versa). Any references cited in the abstract must be given in full. Unpublished results and personal communications are not recommended in the reference list, but may be mentioned in the text. If these references are included in the reference list they should follow the standard reference style of the journal and should include a substitution of the publication date with either "Unpublished results" or "Personal communication" Citation of a reference as "in press" implies that the item has been accepted for publication.

reference style

Text: All citations in the text should refer to:

- a. *Single author:* the author's name (without initials, unless there is ambiguity) and the year of publication;
- b. *Two authors:* both authors' names and the year of publication;
- c. *Three or more authors:* first author's name followed by "et al." and the year of publication.

Examples:

"as demonstrated (Caquot, 2001a, 2001b, 2003; Caquot and Jones, 1995). Mulilis et al. (2006) have recently shown ..."

List: References should be arranged first alphabetically and then further sorted chronologically if necessary. More than one reference from the same author(s) in the same year must be identified by the letters "a", "b", "c", etc., placed after the year of publication.

Reference to a journal publication:

Tuller, M., Or, D., Dudley, L. M., 1999. Adsorption and capillary condensation in porous media: Liquid retention and interfacial configurations in angular pores. *Water Resources Research* 35, 1949–1964.

Reference to a book:

Mitchell, J.K., Soga, K., 2005. *Fundamentals of Soil Behavior*, third ed. John Wiley and Sons, New York

Reference to a chapter in an edited book:

Mettam, G.R., Adams, L.B., 1999. How to prepare an electronic version of your article, in: Jones, B.S., Smith, R.Z. (Eds.), *Introduction to the Electronic Age*. E-Publishing Inc., New York, pp. 281–304.

Web references:

As a minimum, the full URL should be given and the date when the reference was last accessed. Any further information, if known (DOI, author names, dates, reference to a source publication, etc.), should also be given.

AUTHOR INFORMATION

The following information about the authors should be enclosed with the paper: names, complete postal addresses, telephone and fax numbers and E-mail addresses. Indicate the corresponding person.

ACCEPTANCE OF PAPERS AND COPYRIGHT

The Editorial Committee of the Slovenian Geotechnical Review reserves the right to decide whether a paper is acceptable for publication, to obtain peer reviews for submitted papers, and if necessary, to require changes in the content, length or language.

On publication, copyright for the paper shall pass to the ACTA GEOTECHNICA SLOVENICA. The AGS must be stated as a source in all later publication.

For further information contact:

Editorial Board
 ACTA GEOTECHNICA SLOVENICA
 University of Maribor,
 Faculty of Civil Engineering
 Smetanova ulica 17, 2000 Maribor, Slovenia
 E-mail: ags@uni-mb.si

NAMEN REVIJE

Namen revije ACTA GEOTECHNICA SLOVENICA je objavljane kakovostnih teoretičnih člankov z novih pomembnih področij geomehanike in geotehnike, ki bodo dolgoročno vplivali na temeljne in praktične vidike teh področij.

ACTA GEOTECHNICA SLOVENICA objavlja članke s področij: mehanika zemljin in kamnin, inženirska geologija, okoljska geotehnika, geosintetika, geotehnične konstrukcije, numerične in analitične metode, računalniško modeliranje, optimizacija geotehničnih konstrukcij, terenske in laboratorijske preiskave.

Revija redno izhaja dvakrat letno.

AVTORSKE PRAVICE

Ko uredništvo prejme članek v objavo, prosi avtorja(je), da prenese(jo) avtorske pravice za članek na izdajatelja, da bi zagotovili kar se da obsežno razširjanje informacij. Naša revija in posamezni prispevki so zaščiteni z avtorskimi pravicami izdajatelja in zanje veljajo naslednji pogoji:

fotokopiranje

V skladu z našimi zakoni o zaščiti avtorskih pravic je dovoljeno narediti eno kopijo posameznega članka za osebno uporabo. Za naslednje fotokopije, vključno z večkratnim fotokopiranjem, sistematičnim fotokopiranjem, kopiranjem za reklamne ali predstavitvene namene, nadaljnjo prodajo in vsemi oblikami nedobičkonosne uporabe je treba pridobiti dovoljenje izdajatelja in plačati določen znesek.

Naročniki revije smejo kopirati kazalo z vsebino revije ali pripraviti seznam člankov z izvlečki za rabo v svojih ustanovah.

elektronsko shranjevanje

Za elektronsko shranjevanje vsakršnega gradiva iz revije, vključno z vsemi članki ali deli članka, je potrebno dovoljenje izdajatelja.

ODGOVORNOST

Revija ne prevzame nobene odgovornosti za poškodbe in/ali škodo na osebah in na lastnini na podlagi odgovornosti za izdelke, zaradi malomarnosti ali drugače, ali zaradi uporabe kakršnekoli metode, izdelka, navodil ali zamisli, ki so opisani v njej.

AIMS AND SCOPE

ACTA GEOTECHNICA SLOVENICA aims to play an important role in publishing high-quality, theoretical papers from important and emerging areas that will have a lasting impact on fundamental and practical aspects of geomechanics and geotechnical engineering.

ACTA GEOTECHNICA SLOVENICA publishes papers from the following areas: soil and rock mechanics, engineering geology, environmental geotechnics, geosynthetic, geotechnical structures, numerical and analytical methods, computer modelling, optimization of geotechnical structures, field and laboratory testing.

The journal is published twice a year.

COPYRIGHT

Upon acceptance of an article by the Editorial Board, the author(s) will be asked to transfer copyright for the article to the publisher. This transfer will ensure the widest possible dissemination of information. This review and the individual contributions contained in it are protected by publisher's copyright, and the following terms and conditions apply to their use:

photocopying

Single photocopies of single articles may be made for personal use, as allowed by national copyright laws. Permission of the publisher and payment of a fee are required for all other photocopying, including multiple or systematic copying, copying for advertising or promotional purposes, resale, and all forms of document delivery.

Subscribers may reproduce tables of contents or prepare lists of papers, including abstracts for internal circulation, within their institutions.

electronic storage

Permission of the publisher is required to store electronically any material contained in this review, including any paper or part of the paper.

RESPONSIBILITY

No responsibility is assumed by the publisher for any injury and/or damage to persons or property as a matter of product liability, negligence or otherwise, or from any use or operation of any methods, products, instructions or ideas contained in the material herein.